NONLINEAR DYNAMICS OF MODE COMPETITION IN ANNULAR FLOWS

MARC ÀVILA CAÑELLAS

Dissertation submitted for the Degree of
Doctor of Philosophy

UNIVERSITAT POLITÈCNICA DE CATALUNYA
DEPARTAMENT DE FÍSICA APLICADA

April 2008

NONLINEAR DYNAMICS OF MODE COMPETITION IN ANNULAR FLOWS
Marc Àvila Cañellas, Ph.D.
Universitat Politècnica de Catalunya 2008

The understanding of the transition to chaotic behavior and turbulence in natural flows has been and continues to be a great scientific challenge. Due to the complexity of this general problem, there has been a need to seek more fundamental laboratory flows from which the important physics can be extracted. The swirling flow between two concentric cylinders, known as Taylor–Couette flow, has been used as canonical example for centrifugal instability and transition to turbulence following a progression of flow instabilities.

The aim of the thesis has been to provide a deeper understanding of several experimental observations of spatio-temporally complex flows for which no theoretical picture was available. In order to accomplish this goal, accurate spectral computations of the full Navier–Stokes equations have been combined with equivariant bifurcation and normal form theories. The coupling of these tools not only aids in understanding the nature of the observed flows, but furnishes the setting to compare systems with distinct physical instability mechanisms and geometry.

Different configurations of the classical Taylor–Couette apparatus have been considered in the thesis. First, competition between centrifugal instability and shear due to an additional imposed axial pressure gradient is investigated. This competition results in secondary spiral flows of different angles and propagation speeds that may coexist in space and time. Temporal modulations of axial shear, in this case due to axial sliding of the inner cylinder, lead to a great degree of stabilization of the basic steady flow. However, it is shown here that when transition occurs, the flow becomes highly disordered due to a sequence of symmetry breaking bifurcations which cannot be detected in the laboratory due to experimental uncertainty. Finally, temporal modulations of the inner cylinder rotation are considered and competition between two cellular flows with same spatial symmetries but different spatio-temporal symmetries is investigated. Agreement is achieved with experiments except for the frequency band where these flows coexist. In order to investigate these effects, a radical change in the numerical model is needed. This will be addressed in future work.

ACKNOWLEDGEMENTS

I would like to thank my advisers Francisco Marqués and Álvaro Meseguer for their guidance and help over the past three and a half years. I would also like to thank my adviser Juan Lopez for showing me a broad perspective of fluid dynamics and its applications.

Financial support from the Spanish Ministry of Science and Education, including my stays at Arizona State University, is fully acknowledged.

Finally, I would like to thank my family for their support and understanding. This thesis would not have been possible without the endless encouragement and advice from my mother, Núria Cañellas, and her husband, Josep Piñol.

TABLE OF CONTENTS

CHAPTER 1
INTRODUCTION

The flow of a viscous fluid contained between the gap of two rotating cylinders, known as Taylor–Couette flow, has been a paradigm for the study of the transition from a simple laminar flow to chaotic flow following a progression of instabilities to states with increasing spatial and temporal complexity (Coles, 1965; Fenstermacher, Swinney & Gollub, 1979). Recent developments in dynamical systems theory, computational capabilities and measurement techniques have led to a better understanding of the transition to complex dynamics in fluid flow. Yet it is neither well defined nor understood how a fluid becomes turbulent. In contrast to other flows, the Taylor–Couette system has already proven very useful to elucidating transitions between laminar states, so it is thus well suited to investigate the question of onset of turbulence.

Figure 1.1 shows a schematic of the Taylor–Couette apparatus. The geometry of the system is defined by the radius of the inner and outer cylinders, r_i and r_o respectively, and the length of the cylinders h. The relevant parameters are the aspect ratio $\Gamma = h/d$, where $d = r_o - r_i$ is the gap between cylinders, and radius ratio $\eta = r_i/r_o$. Most of the theoretical and computational work on Taylor–Couette flow assumes that the aspect ratio of the apparatus is infinite, i.e. $\Gamma \to \infty$. This approach has rendered excellent agreement with experiments in long cylinders that have been specifically designed in order to minimize end-wall effects. For low angular speeds of the cylinders, the flow is steady and purely azimuthal. This basic state is known as circular Couette flow (CCF). When the outer cylinder is at rest and the angular velocity Ω_i of the inner cylinder exceeds a critical value $\Omega_{i,c}$, circular Couette flow becomes unstable and axisymmetric meridional cells develop. The cells are separated by radial jets of angular momentum emanating from the cylinders boundary layers. This flow pattern, known as Taylor vortex flow (TVF), is steady and periodic in the axial direction. Each pair of cells (vortices) has a wavelength λ (measured in d space units) which defines the wavenumber $k = 2\pi/\lambda$ of the pattern. Figure 1.2 shows a schematic of TVF.

The symmetries of the Taylor–Couette apparatus and its boundary conditions play a crucial role on the rich nonlinear dynamics that has been observed. The study of bifurcations and symmetric flow patterns has contributed to the development of equivariant bifurcation and normal form theories (Golubitsky, Stewart & Schaeffer, 1988; Chossat & Iooss, 1994; Chossat & Lauterbach, 2000). The Taylor–Couette system is invariant under arbitrary rotations about the cylinders axis and a reflection about the horizontal mid-plane, which together generate an $SO(2) \times Z_2$ symmetry group. In the infinite-

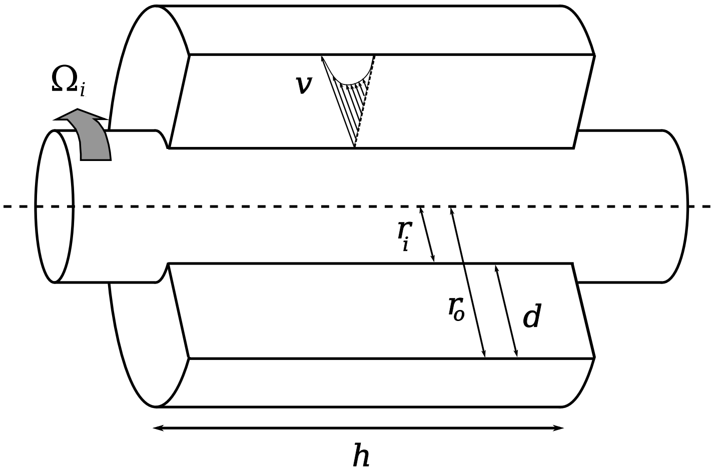

Figure 1.1: Schematic of the Taylor–Couette flow with stationary outer cylinder.

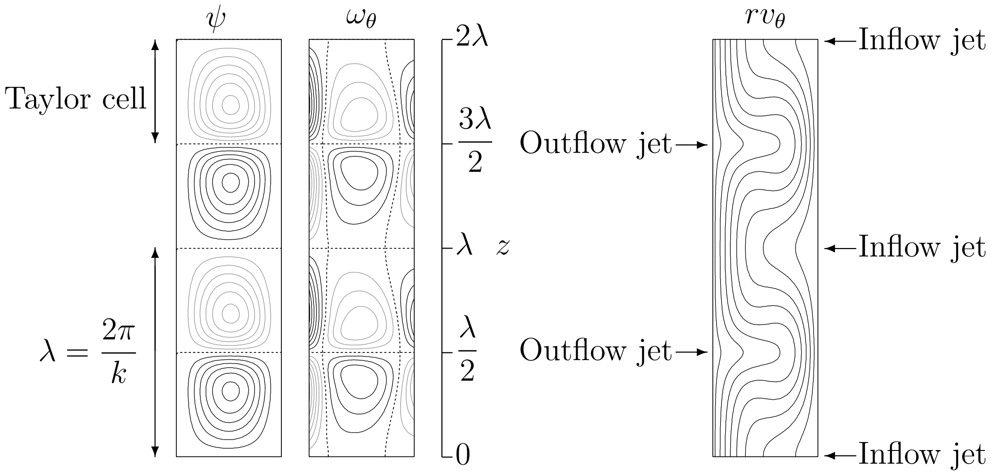

Figure 1.2: Schematic of Taylor vortex flow with axial wavenumber $k = 3.15$. Contours of the stream-function ψ and azimuthal vorticity ω_θ are shown in a meridional cross-section. Vortex lines (rv_θ contours) show the outflow and inflow jets separating the Taylor cells. Black (gray) contours correspond to positive (negative) values, showing $r \in [r_i, r_o]$ and $z \in [0, 2\lambda]$.

cylinder model the system is also invariant under translations along the axis, generating the $SO(2) \times \mathcal{E}(1)$ non-compact group. Non-compact groups, specifically $\mathcal{E}(1)$, are quite difficult to treat mathematically. For example, in the non-compact case, the spectrum contains both a discrete part (eigenvalues) and a continuous part. However, in the case where axial periodicity of the patterns is assumed, the symmetry group of the problem becomes the $\mathcal{G} = SO(2) \times O(2)$ compact group.

Lord Rayleigh (1916) showed that an inviscid rotating flow is stable provided that its angular momentum increases radially outwards

$$\frac{d}{dr}\big(r^2\Omega(r)\big) > 0 \quad \forall\, r. \tag{1.1}$$

In the case of viscous circular Couette flow with rotating inner cylinder and stationary outer cylinder, angular momentum decreases outwards from $r_i^2\Omega_i$ to 0 due to the no-slip boundary conditions. Therefore, according to Rayleigh's invsicid criterion the Couette profile is unstable at infinitesimally small Ω_i. When viscosity is accounted for, a non-dimensional flow Reynolds number associated to the inner cylinder rotation can be defined as $Re_i = dr_i\Omega_i/\nu$, where ν is the kinematic viscosity of the working fluid. In a ground-breaking experimental and theoretical work Taylor (1923) showed that viscosity shifts the onset of secondary flow to finite $Re_{i,c}$, defined as the critical Reynolds number. He performed a linear stability analysis of the Navier–Stokes equations and obtained the critical angular speed of the inner cylinder in remarkable agreement with his own laboratory experiments. He also showed that at the bifurcation point, the emerging pattern consists of a pair of counter-rotating axisymmetric (Taylor) cells which are approximately square, i.e. with critical axial wavenumber $k_c \approx \pi$.

1.1 Wavenumber selection: Eckhaus instability

The transition from a uniform state to a spatially periodic pattern, of wavenumber k_c, is common to many hydrodynamic systems. For $Re_i > Re_{i,c}$, a continuous wave-vector band of solutions bifurcates from the basic state. The width of this band at a particular Re_i is given by the neutral stability curve shown in figure 1.3 (solid line). However, apart from the solution with k_c at $Re_{i,c}$, the other solutions are born unstable and stabilize for higher Re_i upon crossing the so-called Eckhaus curve (dashed line). Therefore, at a given Reynolds number only flow patterns with wavenumber inside the Eckhaus curve are stable and compete. The bifurcation scenario leading to the stabilization of the Eckhaus unstable solutions was elucidated by Tuckerman & Barkley (1990) using a Ginzburg-Landau equation with periodic boundary conditions.

The threshold for Eckhaus instability in Taylor–Couette flow was determined experimentally by Dominguez-Lerma, Cannell & Ahlers (1986), who showed that for $Re_i > Re_{i,c}$ the preferred axial wavenumber deviates from the critical value k_c. However, it is not yet well understood how k is selected on the stable Eckhaus band depending on initial and environmental conditions.

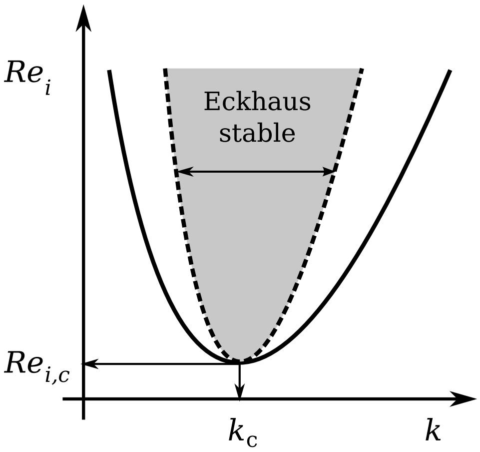

Figure 1.3: Neutral stability curve (solid line) of CCF. The onset of instability is at $Re_{i,c}$ with critical axial wavenumber k_c. TVF with $k \neq k_c$ are unstable at the bifurcation point and restibilize upon crossing the Eckhaus curve (dashed line). Depending on initial and experimental conditions any wavenumber in the shaded region can be selected.

1.2 Flow regimes and transitions

The Eckhaus instability mechanism is not observable in narrow gap ($\eta \to 1$) Taylor–Couette flow due to a secondary Hopf bifurcation which occurs at $Re_{i,w} \gtrsim Re_{i,c}$. The resulting flow, referred to as wavy vortex flow (WVF), is characterized by azimuthal waves that rotate around the cylinder at constant speed. Although WVF is time-periodic, the motion becomes time-independent when observed in a co-rotating frame. Therefore, WVF is a relative equilibrium of the Navier–Stokes equations. King, Li, Lee, Swinney & Marcus (1984) performed laboratory experiments and numerical computations to determine the wavespeed of WVF as a function of the aspect ratio Γ, the Reynolds number Re_i, the axial wavenumber of the underlying Taylor vortices k and the number of azimuthal waves n. They found hat the wavespeed is robust with respect to the geometry and wavenumbers and essentially depends on Re_i. Their experimental results, extrapolated to the $\Gamma \to \infty$ limit, were in excellent agreement with their axially periodic simulations.

If the rotation rate of the inner cylinder is further increased, Fenstermacher *et al.* (1979) showed that WVF undergoes another Hopf bifurcation to modulated wavy vortex flow (MWVF). In MWVF, the motion is quasi-periodic; there are two rotating waves on the Taylor vortices with different frequencies and azimuthal wavenumbers. In a frame co-rotatinng with one of the waves, modulated wavy vortex flow is time-periodic, and thus it is a relative periodic orbit. Upon increasing Re_i the flow gradually loses its

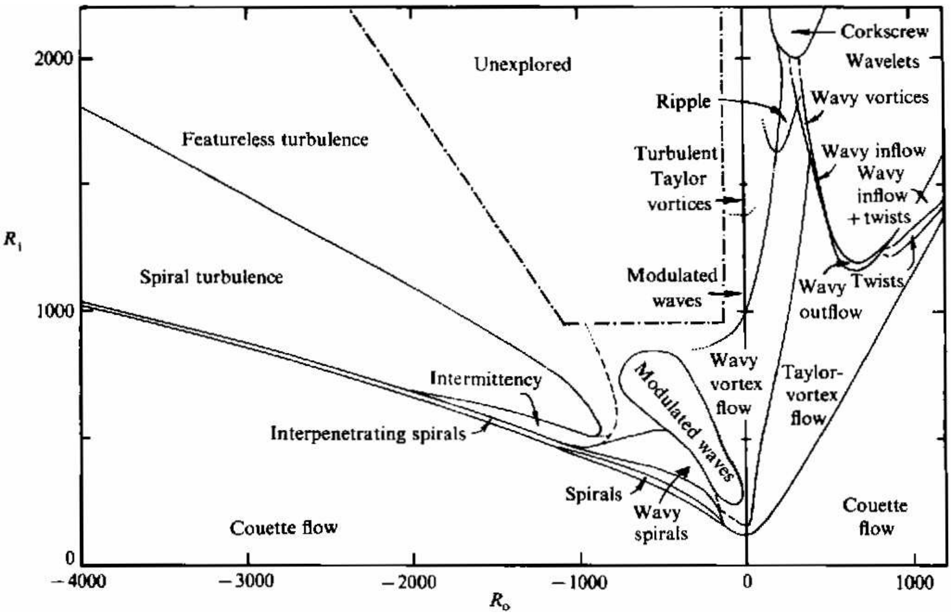

Figure 1.4: Regime diagram of flow between two independently rotating cylinders (Andereck *et al.*, 1986). The rotation speeds of the cylinders are measured by the inner and outer cylinder Reynolds numbers, R_i and R_o, which correspond to Re_i and Re_o in our notation.

azimuthal and axial periodicity and becomes weakly turbulent (Brandstäter & Swinney, 1987).

Andereck, Liu & Swinney (1986) investigated the nonlinear dynamics of Taylor–Couette flow with independently rotating cylinders. They mapped out the two-dimensional parameter space spanned by the inner and outer cylinders Reynolds numbers, Re_i and Re_o, and revealed a large variety of flow regimes. Figure 1.4 shows the regime diagram they obtained by fixing Re_o and slowly increasing Re_i to detect transitions. The flow regimes are distinguished by their spatio-temporal symmetries, frequencies and azimuthal and axial wavenumbers.

When the cylinders rotate in opposite directions, there exists a rotation rate $\mu = Re_o/Re_i$, with $\mu < 0$, such that the primary bifurcation to TVF is replaced by a Hopf bifurcation to non-axisymmetric spiral vortices. This was shown numerically by Krueger, Gross & Di Prima (1966) and experimentally by Snyder (1968), who determined this bicritical μ for several values of the radius ratio. Langford, Tagg, Kostelich, Swinney & Golubitsky (1988) performed a comprehensive linear stability analysis of counter-rotating circular Couette flow for a wide range of μ and η. They showed that for fixed η and decreasing μ the azimuthal wavenumber of the bifurcating spiral vortices increases monotonically in steps of 1. In particular, they computed the bicritical curves $\mu_c(\eta)$ where spiral vortices of different azimuthal wavenumber, n and $n+1$, bifurcate simultaneously. It is worth noting that care must be taken when performing nonlinear computations of spiral vortices with periodic boundary conditions. The secondary spiral vortices generate a weak axial flow which is not physically meaning in the case of an experimental apparatus with end-walls. Edwards, Tagg, Dornblaser & Swinney (1991) imposed a non-periodic pressure term in the Navier–Stokes equations which enforced a zero net axial mass flow and obtained excellent agreeement with their experimental observations.

1.3 Variations of the Taylor–Couette setting

Several variations of the Taylor–Couette problem have focused on the degree of stabilization that can be achieved, i.e. on the degree to which the threshold for the onset of Taylor vortex flow can be shifted to larger angular speeds of the inner cylinder. For example, the superposition of an axial pressure-driven through-flow has been shown to be an efficient mechanism to stabilize the basic flow (Snyder, 1962; Takeuchi & Jankowski, 1981; Meseguer & Marques, 2002). In this case, the basic flow is a combination of circular Couette flow and an axial parabolic profile, termed by Joseph (1976) as spiral Poiseuille flow. For low values of the through-flow the transition is observed to axially propagating Taylor vortices, which are superseded by spiral vortices for higher values of the through-flow (Snyder, 1962; Takeuchi & Jankowski, 1981).

A most interesting feature of this flow was reported by Nagib (1972), who observed secondary flows where two spiral structures coexist simultaneously in space and time in the co-rotating regime. More recently, Lueptow, Docter & Min (1992); Tsameret & Steinberg (1994) have observed several complex flow regimes of Taylor and spiral vortices, including mixed modes, in the case of stationary outer cylinder.

The imposed through-flow generates an axial mass flow which advects perturbations downstream. One must then distinguish between *convective* and *absolute* instabilities (Huerre & Monkewitz, 1990). In the first case, perturbations are amplified while being carried away with the through-flow. The system behaves like a noise amplifier and the bifurcated propagating Taylor vortices feature a time-dependent irregular wavenumber (Babcock, Ahlers & Cannell, 1994). In the absolutely unstable regime perturbations grow until they fill the apparatus, resulting in a well defined spatially periodic flow. Transition thresholds between these regimes have been recently determined numerically and experimentally (Pinter, Lücke & Hoffmann, 2003; Langenberg, Heise, Pfister & Abshagen, 2004).

Axial sliding of the inner cylinder has also been investigated as a stabilization strategy, beginning with the pioneering experimental and analytical work of Ludwieg (1964). However, much less attention has been paid to this problem mainly due to the technical difficulties in its experimental realization. This problem can be formulated either as an open flow system or an enclosed system with end-walls. Ali & Weidman (1993) studied the stability of the latter, and more recently Meseguer & Marques (2000) compared both systems. They focused on the former and showed that stability is enhanced only for slow axial sliding, but that the difference between both systems is small.

Hu & Kelly (1995) considered temporal modulations of both Poiseuille flow and axial sliding in an open Taylor–Couette system and showed that both mechanisms are very efficient in delaying transition. Their theoretical results motivated the experimental work of Weisberg, Kevrekidis & Smits (1997) in order to verify this effect and devise transition control mechanisms based on axial oscillations of the inner cylinder. However, there was only qualitative agreement between experiments and theory due to endwall effects which impose a zero mean axial flow (Marques & Lopez, 1997). Marques & Lopez (1997) noted that for small frequencies and large amplitudes of the oscillations there are some windows of parameter space where the transition is via a Neimark–Sacker bifurcation to non-axisymmetric spiral modes. These windows of parameter space were investigated by Marques & Lopez (2000) using Floquet analysis and Sinha, Kevrekidis & Smits (2006) who experimentally identified regions of quasi-periodic motion and frequency-locking. However, the results they obtained were noisy even very close to the onset of instability.

Donnelly (1964) experimentally investigated time-harmonic modulations of the inner cylinder rotation and observed that modulations delayed the onset of sustained Taylor vortices to higher mean rotation. His findings were contradicted by the theoretical work of Hall (1975) and Floquet analysis of Riley & Laurence (1976), indicating that modulations had a destabilizing effect. The controversy was resolved by Barenghi & Jones (1989), who introduced a low level of noise in nonlinear computations of the Navier–Stokes equations and concluded that the discrepancies regarding stability limits were due to noise-induced difficulties in experimentally determining the onset of instability. More recently, the problem of modulations about a zero-mean has been investigated by Youd, Willis & Barenghi (2003, 2005), who have found a class of Taylor vortex flows whose meridional ciruclation is independent of the direction of rotation of the inner cylinder.

1.4 End-wall effects

Cole (1976) investigated the effect of cylinders length on the Taylor vortex and secondary wavy vortex instabilities. He observed that the critical Reynolds number for TVF is in good agreement with theoretical predictions for infinite cylinders even for aspect ratios as low as $\Gamma = 8$. However, he found that the transition to WVF is very sensitive to aspect ratio. In particular, one needs $\Gamma > 40$ to obtain quantitative agreement with the theory for infinite cylinders $\Gamma \to \infty$.

The presence of end-walls destroys the translation invariance along the cylinders axis. As a consequence, the fluid column admits only an integer number of Taylor cells instead of the continuous axial wavenumber spectrum given by the Eckhaus band of the $\Gamma \to \infty$ limit. Most of the experimental studies of Taylor–Couette flow use either stationary end-walls or end-walls attached to the outer cylinder. In these cases, the discontinuous nature of the boundary conditions, where the inner cylinder meets the end-walls, generates weak vortices for Reynolds numbers well below the critical Reynolds number for $\Gamma \to \infty$, $Re_{i,c}$. As Re_i is increased, the cellular pattern propagates towards the center of the apparatus until it fills the column at about $Re_{i,c}$ (Cole, 1976; Benjamin, 1978). Therefore, the transition to cellular flow is not the result of a bifurcation but of a continuous process.

For end-walls at rest, the end-wall boundary layer flow tends to be radially inward. However, Benjamin (1978); Benjamin & Mullin (1981) found that cellular flows at low aspect ratio could also have an outflow at one or both end-walls boundary layers. These flows, termed as anomalous modes, are disconnected branches of the flow at $Re_i \to 0$ and appear only at higher Re_i. For $\Gamma \sim 1$ competition between the two cell mode and the one cell anomalous mode has been extensively investigated (Benjamin & Mullin, 1981; Cliffe, 1983; Pfister, Schmidt, Cliffe & Mullin, 1988) and the bifurcation scenario has recently been elucidated (Mullin, Toya & Tavener, 2002). Pfister, Buzug & Enge (1992) showed that at higher Re_i bifurcations to non-axisymmetric flows leading to chaotic behavior occur. These are the subject of current numerical investigations to shed light on the transition mechanisms and scenarios (Marques & Lopez, 2006).

1.5 Plan of the thesis

The results presented on this thesis are focused on the understanding of experimental observations in long aspect ratio Taylor–Couette apparatuses. Complex flow transitions, occurring in a variety of situations, are carefully investigated to shed light on the underlying bifurcation scenarios. Accurate spectral computations of the Navier–Stokes equations are systematically combined with equivariant bifurcation and normal form theories to precisely describe the spatio-temporal properties of the flows.

The infinite-cylinder approximation is used in linear stability analyses and axially periodic boundary conditions are considered for nonlinear computations of the Navier–Stokes equations. The approach is validated by the fact that the numerics and experiments, of aspect ratio $\Gamma > 100$ in all cases investigated, have substantial agreement in most observables. In annuli with such large aspect ratios, end effects are secondary to mode competition between flows of different wavenumbers. Moreover, one has finite computational resources and must decide how best to deploy them. Modeling rigid or open end-walls in such long aspect ratio experiments is beyond current computational resources.

The thesis is structured as follows. The governing equations and numerical methods are presented in chapter 2. The numerical scheme is based on a solenoidal Petrov–Galerkin approximation of the Navier–Stokes equations which has been developed from previous spectral schemes recently formulated and extensively tested for cylindrical geometries (Meseguer & Mellibovsky, 2007; Meseguer, Avila, Mellibovsky & Marques, 2007). Convergence tests have been performed and results compared to published papers. In chapter 3, the bifurcation scenario leading to the coexistence of spiral waves experimentally observed by Nagib (1972) in spiral Poiseuille flow is investigated. The material corresponding to this chapter has been published in Avila, Meseguer & Marques (2006). In chapter 4, we consider temporal modulations of axial sliding of the inner cylinder and study the transition to spatio-temporal complexity recently reported by Sinha *et al.* (2006). The results have been disseminated in Avila, Marques, Lopez & Meseguer (2007). Chapter 5 is devoted to the study of mode competition and wavenumber selection that arises when the rotation of the inner cylinder is modulated in time about a zero-mean. The numerical computations of chapter 5 are complemented with experimental results of Mr. Michael Belisle and Prof. William S. Saric at the former Taylor–Couette laboratory of the Department of Mechanical and Aerospace Engeneering, Arizona State University. These joint theoretical and experimental investigations have been published in Avila, Belisle, Lopez, Marques & Saric (2008). The normal form analyses corresponding to the different configurations and bifurcations investigated in the thesis are given in Appendices B, C and D. Finally, a general overview of the main results is given in chapter 6.

CHAPTER 2
GOVERNING EQUATIONS AND NUMERICAL METHODS

We consider an incompressible fluid of kinematic viscosity ν and density ϱ which is contained between two concentric rotating cylinders, whose radius and angular velocities are r_i^*, r_o^* and Ω_i and Ω_o, respectively. The dimensionless parameters governing this problem are the ratio of inner to outer cylinder radius $\eta = r_i^*/r_o^*$, which fixes the geometry of the annulus, and the Couette flow Reynolds numbers $Re_i = dr_i^*\Omega_i/\nu$ and $Re_o = dr_o^*\Omega_o/\nu$, where $d = r_o^* - r_i^*$ is the gap between cylinders. In the linear stability analysis the cylinders are assumed to be infinite, whereas the nonlinear computations are performed in a periodic annulus with axial wavelength Λd.

Henceforth, all variables will be rendered dimensionless using d, d^2/ν, and ν^2/d^2 as units for space, time and the reduced pressure ($p = p^*/\varrho$), respectively. The Navier–Stokes equation and the incompressibility condition for this scaling become

$$\partial_t \mathbf{v} + (\mathbf{v}\cdot\nabla)\mathbf{v} = -\nabla p + \Delta\mathbf{v}, \quad \nabla\cdot\mathbf{v} = 0\ . \tag{2.1}$$

Let $\mathbf{v} = (v_r, v_\theta, v_z)$ be the physical components of the velocity field in cylindrical coordinates (r, θ, z). In the infinite-cylinder idealization, the boundary conditions read

$$\mathbf{v}(r_i, \theta, z, t) = (0, Re_i, 0), \quad \mathbf{v}(r_o, \theta, z, t) = (0, Re_o, 0). \tag{2.2}$$

where $r_i = r_i^*/d = \eta/(1-\eta)$, $r_o = r_o^*/d = 1/(1-\eta)$ are the non-dimensional radii of the cylinders. The purely rotary flow

$$\mathbf{v}_b(r) = \Big(0, Ar + \frac{B}{r}, 0\Big) \tag{2.3}$$

where

$$A = \frac{Re_o - \eta Re_i}{1+\eta}, \quad B = \eta\frac{Re_i - \eta Re_o}{(1-\eta)(1-\eta^2)}\ , \tag{2.4}$$

is an exact solution to the Navier–Stokes equations (2.1) satisfying the no-slip boundary conditions (2.2). This steady flow is known as circular Couette flow (CCF).

The governing equations and boundary conditions are invariant to the K_z reflection $z \longrightarrow -z$ and to translations T_a along the z-axis, which generate the Euclidean group of symmetries $\mathcal{E}(1)$. However, in the nonlinear computations axial periodicity is imposed and the symmetry group in the axial direction becomes $O(2)$. Note that as K_z and T_a do not commute (in fact $K_z T_a = T_{-a} K_z$), they together generate an $O(2)$ symmetry group which is not the direct product of $SO(2)$ and Z_2, but the *semi-direct* product $O(2) = SO(2) \rtimes Z_2$. The elements of Z_2 are the identity and K_z. In the azimuthal direction the governing equations are invariant to arbitrary rotations R_α which generate another $SO(2)$ symmetry group. Since both T_a and K_z commute with R_α, these operations generate the group $\mathcal{G} = SO(2) \times O(2)$ of the spatial symmetries of the system. The actions of these symmetries on the velocity field are:

$$T_a\mathbf{v}(r,\theta,z,t) = \mathbf{v}(r,\theta,z+a,t), \tag{2.5}$$

$$K_z\mathbf{v}(r,\theta,z,t) = (v_r, v_\theta, -v_z)(r,\theta,-z,t), \tag{2.6}$$

$$R_\alpha\mathbf{v}(r,\theta,z,t) = \mathbf{v}(r,\theta+\alpha,z,t). \tag{2.7}$$

The basic state (2.3) is invariant under $\mathcal{G}$.

The numerical method used for the results presented in this thesis is based on a Petrov–Galerkin formulation (a comprehensive analysis of this type of formulation can be found in Moser, Moin & Leonard, 1983). The linear stability results have been obtained with a new implementation of the method used by Meseguer & Marques (2000) to determine the stability of spiral Couette flow. Their numerical scheme has been used as a starting point to develop the full three-dimensional unsteady Navier–Stokes solver. Overall, the novel solenoidal scheme used for the nonlinear computations is mainly based on previous spectral schemes recently formulated and extensively tested for cylindrical geometries (Meseguer & Mellibovsky, 2007).

2.1 Linear stability analysis

We investigate the stability of CCF (2.3) to infinitesimal disturbances which are assumed to be periodic in the azimuthal and axial directions:

$$\begin{aligned} \mathbf{v}(r,\theta,z,t) &= \mathbf{v}_b(r) + \mathrm{e}^{\mathrm{i}(kz+n\theta)+\sigma t}\,\mathbf{u}_{kn}(r), \\ p(r,\theta,z,t) &= p_b(z) + \mathrm{e}^{\mathrm{i}(kz+n\theta)+\sigma t}\,q_{kn}(r). \end{aligned} \tag{2.8}$$

On introducing this decomposition in the Navier–Stokes equations (2.1) and neglecting the nonlinear term on the perturbation $\mathbf{u}_{kn}$, we obtain the eigenvalue problem

$$\sigma\mathbf{u}_{kn} + (\mathbf{v}_b\cdot\nabla)\mathbf{u}_{kn} + (\mathbf{u}_{kn}\cdot\nabla)\mathbf{v}_b = -\nabla p_b + \Delta\mathbf{u}_{kn}. \tag{2.9}$$

The boundary conditions (2.2) and solenoidal condition in (2.1) are used to define the space of vector fields of the problem

$$V = \{\mathbf{u}_{kn} \in (\mathcal{L}_2(r_i,r_o))^3 \,|\, \nabla\cdot[\mathrm{e}^{\mathrm{i}(kz+n\theta)}\mathbf{u}_{kn}(r)] = 0,\ \mathbf{u}_{kn}(r_i) = \mathbf{u}_{kn}(r_o) = 0\}, \tag{2.10}$$

where $(\mathcal{L}_2(r_i, r_o))^3$ is the Hilbert space of square-integrable vectorial-functions defined in the interval (r_i, r_o), with the inner product

$$\langle \mathbf{u}, \mathbf{v} \rangle = \int_{r_o}^{r_i} \mathbf{u}^* \cdot \mathbf{v} \, r dr. \tag{2.11}$$

The spatial discretization to solve (2.9) numerically, is accomplished by projecting (2.9) onto a suitable basis. Here * denotes the complex conjugate. Note that for any $u \in V$ and any scalar function p, we have $\langle \mathbf{u}, \nabla p \rangle = 0$. Hence, when discretizing the problem by expanding $\mathbf{u}$ in a suitable basis of V

$$\mathbf{u}_{kn} = \sum_m a_{knm} \, \mathbf{u}_{knm} \qquad \mathbf{u}_{knm} \in V, \tag{2.12}$$

and projecting the linearized equations (2.9) onto V the pressure term disappears, and we get a linear system for the coefficients a_{knm}:

$$\sigma \sum_m \langle \tilde{\mathbf{u}}_{kn\beta}, \mathbf{u}_{knm} \rangle a_{knm} = \sum_m \langle \tilde{\mathbf{u}}_{kn\beta}, \Delta \mathbf{u}_{knm} - \mathbf{v}_b \cdot \nabla \mathbf{u}_{knm} - \mathbf{u}_{knm} \cdot \nabla \mathbf{v}_b \rangle a_{knm}. \tag{2.13}$$

A Petrov–Galerkin scheme is implemented, where the physical basis used to expand the unknown velocity, $\mathbf{u}_{knm}$, differs from the projection basis, $\tilde{\mathbf{u}}_{knm}$. Both sets of bases are given in Appendix §A. Here it suffices to say that the bases $\mathbf{u}_{knm}$ are chosen such that $\mathbf{u}_{knm} \in V$ and the radial direction is discretized using Chebyshev polynomials. Therefore, all the inner products in (2.13) involve polynomials and can be computed exactly using the Chebyshev Gauss–Lobatto quadrature (Canuto, Hussaini, Quarteroni & Zang, 2006). The projection yields the generalized eigenvalue problem

$$\sigma \mathbb{A}^{kn} x = \mathbb{B}^{kn} x \tag{2.14}$$

where the vector x contains the real and imaginary parts of the coefficients a_{knm} in (2.13), and $\mathbb{A}^{kn}$, $\mathbb{B}^{kn}$ are constant matrices, with $\mathbb{A}^{kn}$ positive definite.

The stability of CCF is determined by the sign of the eigenvalue σ_* of (2.14) with $\sigma_* = \max_\sigma \Re(\sigma)$. For negative values of σ_*, CCF is stable under infinitesimal perturbations. When σ_* is positive, it becomes unstable and bifurcated secondary flows appear. Note that $\sigma_*(n, k, \eta, Re_i, Re_o)$ is a function of the physical parameters of the system. For fixed η, Re_o, and given n, k, the inner Reynolds number Re_i such that

$$\sigma_*(n, k, \eta, Re_i, Re_o) = 0 \tag{2.15}$$

is computed to obtain the neutral stability curve. The critical inner Reynolds number is defined as

$$Re_{i,c} = \min_{n,k} \{ Re_i(n, k) \mid \sigma_*(Re_i) = 0 \} \tag{2.16}$$

and the corresponding values of n, k are the critical azimuthal and axial wavenumbers n_c, k_c, which will dictate the geometrical shape of the critical eigenfunction.

2.2 Nonlinear computations

In order to investigate the dynamics of the bifurcated flows beyond onset, nonlinear computations of the Navier–Stokes equations are required. In this case, the perturbation $\mathbf{u}$ is discretized as

$$\mathbf{u}(r,\theta,z,t) = \sum_{l=-L}^{L}\sum_{n=-N}^{N}\sum_{m=0}^{M} a_{lnm}(t)\mathrm{e}^{\mathrm{i}(lk_0 z+n\theta)}\mathbf{u}_{lnm}(r), \tag{2.17}$$

which is Λ-periodic, with $\Lambda = 2\pi/k_0$, in the axial direction. The discrete set of axial wavenumbers is of the form $k = lk_0$ for $l = [-L, L]$, i.e. they are all harmonics of the fundamental axial wavenumber k_0. Note that the expressions for $\mathbf{u}_{lnm}$ are the same as in the linear stability analysis and the convention $\mathbf{u}_{lnm} = \mathbf{u}_{knm}$, with $k = l\,k_0$, has been used.

The basic flow (2.3) can be used to simplify the numerical scheme by decomposing the velocity field and pressure as

$$\begin{aligned} \mathbf{v}(r,\theta,z,t) &= \mathbf{v}_b(r) + \mathbf{u}(r,\theta,z,t), \\ p(r,\theta,z,t) &= p_b(z) + q(r,\theta,z,t). \end{aligned} \tag{2.18}$$

On introducing the perturbed fields in the Navier-Stokes equations, we obtain a nonlinear initial-boundary problem for the perturbations $\mathbf{u}$ and q:

$$\partial_t\mathbf{u} = -\nabla q + \Delta\mathbf{u} - (\mathbf{v}_b\cdot\nabla)\mathbf{u} - (\mathbf{u}\cdot\nabla)\mathbf{v}_b - (\mathbf{u}\cdot\nabla)\mathbf{u}, \qquad \nabla\cdot\mathbf{u} = 0, \tag{2.19}$$

for $(r,\theta,z) \in \mathfrak{D} = [r_i, r_o]\times[0,2\pi]\times[0,\Lambda]$ and $t > 0$. The boundary conditions are homogeneous for the radial coordinate and periodic for the azimuthal and axial coordinates

$$\begin{aligned} &\mathbf{u}(r_i,\theta,z,t) = 0, && \mathbf{u}(r_o,\theta,z,t) = 0, \\ &\mathbf{u}(r,\theta+2\pi,z,t) = \mathbf{u}(r,\theta,z,t), && \mathbf{u}(r,\theta,z+\Lambda,t) = \mathbf{u}(r,\theta,z,t). \end{aligned} \tag{2.20}$$

Finally, the initial condition at $t = 0$ is

$$\mathbf{u}(r,\theta,z,0) = \mathbf{u}_0, \qquad \nabla\cdot\mathbf{u}_0 = 0 \quad \text{in } \mathfrak{D}. \tag{2.21}$$

The spectral scheme is obtained when introducing expansion (2.17) in (2.19) and projecting over a suitable set of *test* solenoidal fields

$$\mathbf{\Psi}_{lnm} = \mathrm{e}^{\mathrm{i}(lk_0 z+n\theta)}\tilde{\mathbf{u}}_{lnm}, \tag{2.22}$$

where $\tilde{\mathbf{u}}_{lnm}$ are defined in (A.5) and (A.6). The projection is carried out via the standard volume integral over the domain $\mathfrak{D}$,

$$\big(\mathbf{\Psi}_{lnm}, \partial_t\mathbf{u}_\mathrm{S}\big)_\mathfrak{D} = \big(\mathbf{\Psi}_{lnm}, \Delta\mathbf{u}_\mathrm{S} - (\mathbf{v}_b\cdot\nabla)\mathbf{u}_\mathrm{S} - (\mathbf{u}_\mathrm{S}\cdot\nabla)\mathbf{v}_b - (\mathbf{u}_\mathrm{S}\cdot\nabla)\mathbf{u}_\mathrm{S}\big)_\mathfrak{D}, \tag{2.23}$$

for $(l, n, m) \in [-L, L] \times [-N, N] \times [0, M]$, where

$$(\mathbf{a}, \mathbf{b})_{\mathfrak{D}} = \int_{\mathfrak{D}} \mathbf{a}^* \cdot \mathbf{b} \, \mathrm{d}\mathfrak{D}. \tag{2.24}$$

The pressure term is canceled in the projection, i.e., $(\boldsymbol{\Psi}_{lnm}\ ,\ \nabla q)_{\mathfrak{D}} = 0$, leading to a dynamical system only involving the amplitudes $a_{lmn}(t)$ of the velocity approximation (2.17), i.e,

$$\mathbb{A}^{lnm}_{pqr} \frac{da_{pqr}}{dt} = \mathbb{B}^{lnm}_{pqr} a_{pqr} - \mathbb{N}_{lnm}(a, a), \tag{2.25}$$

where we have used the convention of summation with respect to repeated subscripts. In (2.25), the matrices $\mathbb{A}$ and $\mathbb{B}$ stand for the projection of the time differentiation and linear Laplacian-advection operators, whereas $\mathbb{N}$ is the projected nonlinear advective term.

The system of ODE's (2.25) is integrated in time by means of a linearly implicit method, where backwards differences are used for the linear part and polynomial extrapolation is used for the nonlinear one.

2.2.1 Modal kinetic energy of the solutions

It is convenient to consider the kinetic energy of the perturbation field $\mathbf{u}$, $E(\mathbf{u}, t)$. Since the basic flow has $\mathbf{u} = 0$, a non-zero value of $E(\mathbf{u}, t)$ indicates that the basic state has become unstable and a new state has bifurcated. However, the kinetic energy of the perturbation field alone does not provide information on the dominant axial and azimuthal wavenumbers of the bifurcated solutions. In order to characterize the spatial complexity of these flows, we consider the kinetic energy associated with each Fourier mode in the spectral approximation (2.17)

$$\mathrm{E}_{ln}(t) = \frac{1}{2V} \int_0^{\Lambda} \mathrm{d}z \int_0^{2\pi} \mathrm{d}\theta \int_{r_i}^{r_o} \mathbf{u}^*_{ln} \cdot \mathbf{u}_{ln} \, r \, \mathrm{d}r, \tag{2.26}$$

where $\mathbf{u}_{ln}$ is the (l, n) component of the perturbation field $\mathbf{u}$

$$\mathbf{u}_{ln} = \mathrm{e}^{\mathrm{i}(lk_0 z + n\theta)} \sum_{m=0}^{M} a_{lnm}(t) \mathbf{v}_{lnm}(r). \tag{2.27}$$

L	M	u_r	
		Re_i =72.4569	106.066
4	8	4.23316438	17.832956
	12	4.23319133	17.832834
	16	4.23319131	17.8328605
6	8	4.23360501	17.9595509
	12	4.23363199	17.9594085
	16	4.23363197	17.959437
8	8	4.23360889	17.9697507
	12	4.23363587	17.9696144
	16	4.23363586	17.9696437

Table 2.1: Radial velocity u_r at $(r, \theta, z) = ((r_i + r_o)/2, 0, 0)$, corresponding to the outflow jet, for Taylor vortex flow at different Re_i. The values reported by Jones (1985) are 4.23363 and 17.9705.

Sometimes it is more useful to consider the energy associated to each azimuthal or axial mode

$$\mathrm{E}_l(t) = \sum_{n=-N}^{N} \mathrm{E}_{ln}(t), \tag{2.28}$$

$$\mathrm{E}_n(t) = \sum_{l=-L}^{L} \mathrm{E}_{ln}(t). \tag{2.29}$$

Note that due to the mutual orthogonality of the Fourier modes, this decomposition yields

$$E(\mathbf{u}, t) = \sum_{l=-L}^{L} \sum_{n=-N}^{N} \mathrm{E}_{ln}(t). \tag{2.30}$$

The changes in the distribution of modal energies of the solutions as the Reynolds number is increased aids in identifying subsequent bifurcations and in elucidating the increased complexity of the resulting flow patterns.

2.2.2 Validation of the scheme

Numerical computations have been performed in the axisymmetric steady Taylor vortex flow regime for $\eta = 0.5$ and Reynolds numbers $Re_i = 72.4546$ and $Re_i = 106.066$ as in Jones (1985). Table 2.1 shows the values of the radial velocity u_r for different truncations of the spectral approximation (2.17) at $(r, \theta, z) = ((r_i + r_o)/2, 0, 0)$, which corresponds to the outflow jet separating the Taylor cells.

$Re_i/Re_{i,c}$	$\lambda = 2\pi/k$	Computed	King *et al.*
3.98	2.40	0.3343±0.0005	0.3343±0.0001
3.98	3.00	0.3340±0.0005	0.3340±0.0001

Table 2.2: Wavespeeds of the $n = 6$ wavy vortex flow for $\eta = 0.868$ and different axial periodicities of the pattern. Onset of Taylor vortex flow is at $Re_{i,c} = 115.1$.

The accuracy of the time-stepping scheme has been tested in the non-axisymmetric unsteady wavy vortex flow regime. Wavespeeds have been computed and compared to the experimental and numerical values obtained by King *et al.* (1984), who showed that wavespeeds are very sensitive to numerical discretization and accuracy of the time-stepping scheme. Table 2.2 shows their and our numerical results (within 0.1% of their values).

2.3 Mode competition in axially periodic flows

In a linear stability analysis, the axial wavenumber of the perturbation $\mathbf{u}$ varies continuously. However, in the nonlinear computations the axial direction is treated as being periodic and a suitable fundamental axial wavenumber k_0 in (2.17) has to be selected such that the discretization resolves those axial modes responsible for the instability. In order to illustrate how to choose k_0, let us consider the infinite-cylinder case with the inner cylinder rotating at a constant angular speed, Re_i, and the outer cylinder stationary. For $\eta = 0.5$, circular Couette flow becomes linearly unstable via a pitchfork-of-revolution bifurcation to axisymmetric Taylor vortex flow (TVF) at $Re_{i,c} = 68.19$, with critical axial wavenumber $k_c = 3.162$. For $Re_i > Re_{i,c}$ a continuous wave-vector band of TVF solutions bifurcates from circular Couette flow. The width of this band at a particular Re_i is given by the neutral stability curve of figure 2.1(a) (solid line). However, apart from the solution with k_c, the other solutions are born unstable and stabilize for higher Re_i upon crossing the Eckhaus curve. Figure 2.1(a) shows the Eckhaus curve as obtained by Riecke & Paap (1986) assuming continuous axial wavenumber k (dashed curve), and its classic Ginzburg-Landau estimate (dotted curve).

In the nonlinear computations the spectrum of axial wavenumbers is discrete due to the imposed periodic boundary conditions (2.20). Consider a small fundamental axial wavenumber $k_0 = 0.15$ which corresponds to a periodic annular domain of axial wavelength $\Lambda = 2\pi/k_0 = 41.89$. With this choice, the most unstable Fourier mode in the spectral expansion (2.17) is $l = 21$, with an axial wavenumber $k = l\,k_0 = 3.15$

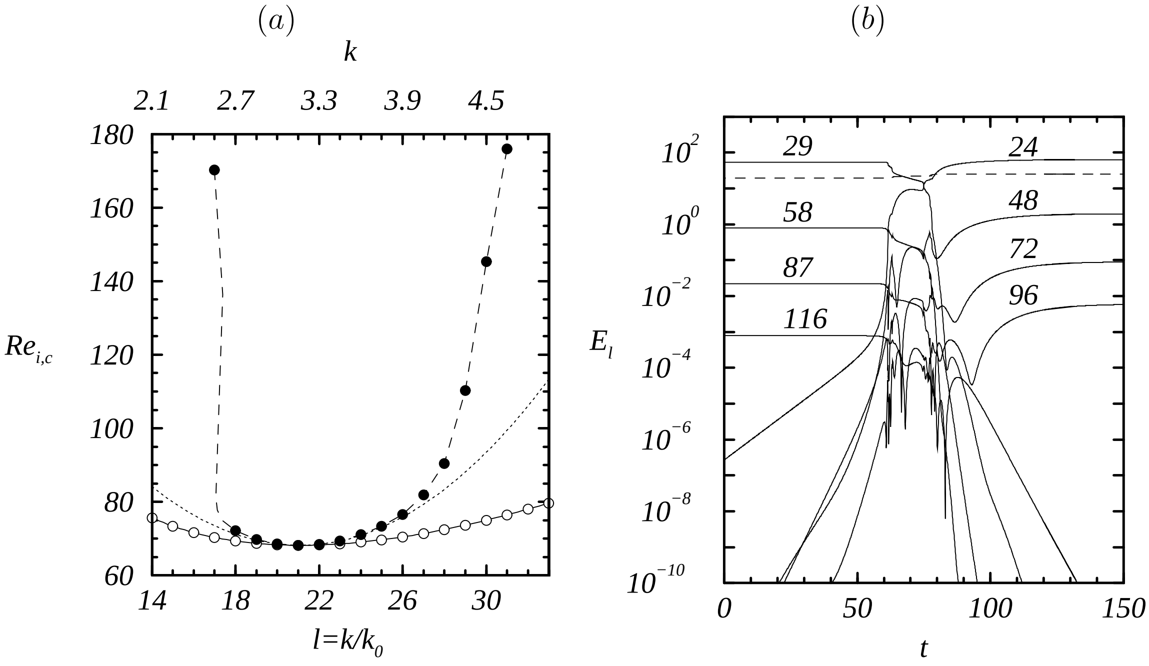

Figure 2.1: (a) Neutral (solid line) and Eckhaus (dashed line) stability curves for circular Couette flow with $\eta = 0.5$ and stationary outer cylinder (computations by Riecke & Paap, 1986). The open and filled circles correspond to the points in these curves with axial wavenumbers $k = l\,k_0$ with $k_0 = 0.15$. The dotted line corresponds to the third-order Ginzburg-Landau approximation of the Eckhaus curve. (b) Solid lines show the kinetic energy time series of the $l = 24, 29$ axial Fourier modes, and their three first harmonics, in the transition from the Eckhaus unstable TVF$_{58}$ to TVF$_{48}$ at $Re_i = 100$. The dashed line corresponds to the $l = 0$ mode.

very close to the critical value k_c. The wavelength of the resulting periodic pattern is $\lambda = 2\pi/k = 1.995$, which correponds to approximately square counter-rotating Taylor cells (see figure 1.2). When considering the full axial domain, $z \in [0, \Lambda]$, the flow spans $\Lambda/(\lambda/2) = 2l = 42$ cells, henceforth TVF$_{42}$.

For $Re_i > Re_{i,c}$ a discrete family of Taylor vortex flows with different l bifurcate supercritically from circular Couette flow at the open circles in figure 2.1(a). These TVF are unstable at onset as circular Couette flow is already unstable to TVF$_{42}$, and they become stable at secondary bifurcations (Tuckerman & Barkley, 1990). These secondary bifurcations are indicated by the filled circles in figure 2.1(a) and coincide very well with the Eckhaus curves computed by Riecke & Paap (1986) and the large aspect ratio experiments of Dominguez-Lerma *et al.* (1986). Here, the Eckhaus instability curve has been determined using nonlinear computations. For example, starting at $Re_i = 100$ with a random perturbation in the Fourier subspace spanned by mode $l = 29$, with corresponding $k = 4.35$, the perturbation is evolved in time, resulting in steady TVF$_{58}$.

Then, a small perturbation to the modes $l = 21, \ldots, 28$ is introduced and their kinetic energy (2.29) is monitored in time. In this case, TVF_{58} is Eckhaus unstable and evolves to TVF_{48}, i.e. with $l = 24$ and $k = 3.6$. This transition is illustrated in figure 2.1(*b*), showing the kinetic energy of the axial Fourier modes $l = 24, 29$ and their first three harmonics. The process is repeated with increasing Re_i in order to detect the point of bifurcation. The use of a small fundamental axial wavenumber k_0 is essential for capturing the nonlinear competition between modes as the Eckhaus curve is crossed.

CHAPTER 3

DOUBLE HOPF BIFURCATION IN SPIRAL POISEUILLE FLOW

The spiral Poiseuille problem deals with the behavior of an incompressible viscous fluid confined between two coaxial cylinders independently rotating around their common axis. In addition, the fluid is enforced to flow downstream by an imposed pressure gradient in the axial direction. The resulting steady spiral flow is a combination of a rotation due to the circular Couette flow and an axial parabolic profile, due to the pressure gradient, also termed spiral Poiseuille flow by Joseph (1976). The spiral Poiseuille flow (SPF) is subject to shear and centrifugal instability mechanisms, which can destabilize the flow for sufficiently high values of the axial pressure gradient and angular speeds of the cylinders.

The stability of SPF was studied experimentally by Snyder (1962) for narrow gap geometry and fixed outer cylinder, showing that the primary transition leads to axially propagating structures. For low values of the through-flow the transition is observed to propagating Taylor vortices. For higher values of the through-flow the primary bifurcation is to spiral vortices of increasing azimuthal and axial wavenumbers (Snyder, 1962; Takeuchi & Jankowski, 1981). The systematic exploration of secondary flows for this problem has also been studied more recently by Lueptow *et al.* (1992) and Tsameret & Steinberg (1994), who have observed several flow regimes of toroidal and spiral vortices. Wereley & Lueptow (1999) have experimentally characterized the velocity fields of some of these regimes and compared them to the Taylor–Couette case. Their results have been numerically reproduced by Hwang & Yang (2005).

Pinter *et al.* (2003) have performed a saddle-point analysis of counter-rotating SPF and have provided the boundaries between convective and absolute instabilities for low through-flow. Their results have been confirmed experimentally (Langenberg *et al.*, 2004). The nonlinear dynamics of SPF for moderate axial flow and counter-rotating cylinders have been studied by Hoffmann, Lücke & Pinter (2004). They have used a hybrid finite-difference-Galerkin method to investigate competition between spirals vortices of opposite helical orientation and propagating Taylor vortices.

Former numerical linear stability analyses of the SPF were carried out in the axisymmetric case (Chung & Astill, 1977; Hasoon & Martin, 1977) or for specific angular rotation speed ratio values of the cylinders (Takeuchi & Jankowski, 1981; Cotrell & Pearlstein, 2004). Meseguer & Marques (2002, 2005*b*) provided a first comprehensive linear stability analysis for medium gap geometry which covered a wide range of independent co-rotating angular speeds of the cylinders as well as axial flow velocities. They found a bicritical curve of coexistence of spiral waves of opposite helical orientation. Over that curve, two, or even three, independent modes bifurcate simultaneously.

Experimental explorations of the co-rotating SPF carried out by Nagib (1972) for small gap revealed the presence of secondary stable regimes consisting of a superposition of traveling spiral waves of opposite helical orientation. The linear stability analysis by Meseguer & Marques (2005*b*) suggested that these originate from the codimension two bifurcation curve where both spiral waves bifurcate simultaneously. However, a nonlinear analysis is required in order to determine the bifurcation scenario leading to the complex flows observed by Nagib (1972). As noted by Joseph (1976), these flows are characterized by very high axial and azimuthal wavenumbers, thus being unfeasible to reproduce them numerically, due to the current computational limitations.

The results presented in this chapter provide numerical evidence of the existence of these secondary regimes for much lower angular and stream-wise speeds of the flow, where the spatial resolution required is less demanding. We combine equivariant bifurcation and normal form theories with numerical computations to elucidate the scenario leading to the coexistence of spiral waves.

3.1 Basic flow and symmetries

We consider the Taylor–Couette system with co-rotating cylinders. In addition, the fluid is driven by an imposed axial pressure gradient which generates a mean axial flow. The non-dimensional dynamical parameters of the system are the inner and outer cylinders Reynolds numbers, Re_i and Re_o, and the *Poiseuille* number $P = \partial p_b / \partial z$ which measures the applied pressure gradient. Figure 3.1 shows the geometry and parameters of the spiral Poiseuille problem.

The steady velocity field satisfying the Navier–Stokes equations (2.1) with boundary conditions (2.20) and imposed axial pressure gradient P is a superposition of circular Couette flow and a logarithmic-parabolic profile in the axial direction

$$\mathbf{v}_b = (u_b, v_b, w_b) = \Big(0, Ar + \frac{B}{r}, C\ln(r/r_o) + \frac{P}{4}(r^2 - r_o^2)\Big), \tag{3.1}$$

where

$$C = \frac{P}{4\ln\eta}\frac{1+\eta}{1-\eta}, \tag{3.2}$$

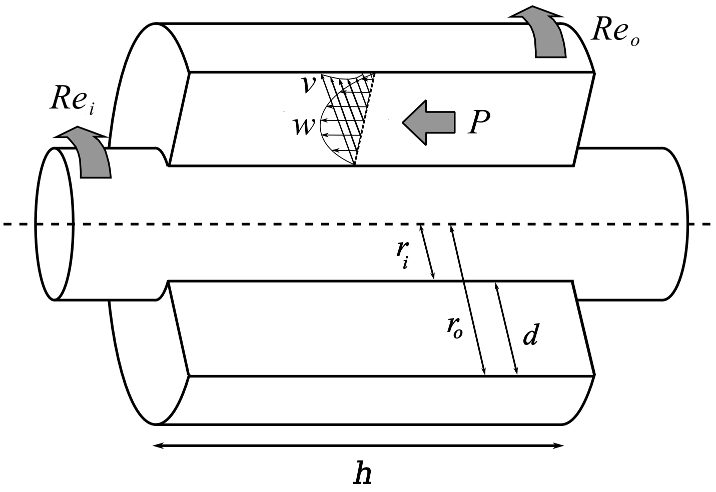

Figure 3.1: Schematic of the spiral Poiseuille flow with co-rotating cylinders.

and A and B as given in (2.4). The mean axial flow generated by the pressure gradient P can be used to define an axial Reynolds number

$$Re_{ax} = \frac{2}{r_i^2 - r_o^2} \int_{r_i}^{r_o} w_b r \, dr = \frac{\eta^2 - (1+\eta^2)\ln\eta - 1}{8(1-\eta^2)\ln\eta} P. \tag{3.3}$$

The governing equations are invariant to rotations R_α about the cylinder axis and to axial translations T_a:

$$R_\alpha(\mathbf{v})(r,\theta,z) = \mathbf{v}(r,\theta+\alpha,z), \tag{3.4}$$

$$T_a(\mathbf{v})(r,\theta,z) = \mathbf{v}(r,\theta,z+a). \tag{3.5}$$

Rotations generate the symmetry group $SO(2)$, and due to the imposed axial periodicity, axial translations generate another $SO(2)$ symmetry group. As rotations and translations commute, the complete symmetry group of the problem is $\mathcal{G} = SO(2) \times SO(2)$. The steady basic flow (3.1) is invariant to $\mathcal{G}$. Note that the imposed axial pressure breaks the Z_2 reflectional symmetry of classical Taylor–Couette flow.

3.2 Bifurcation scenario

Meseguer & Marques (2002, 2005*b*) have recently provided a linear stability analysis of the steady SPF for $\eta = 0.5$ covering a wide range of independent angular speeds of the cylinders and through-flow velocities. They have showed that in the co-rotating

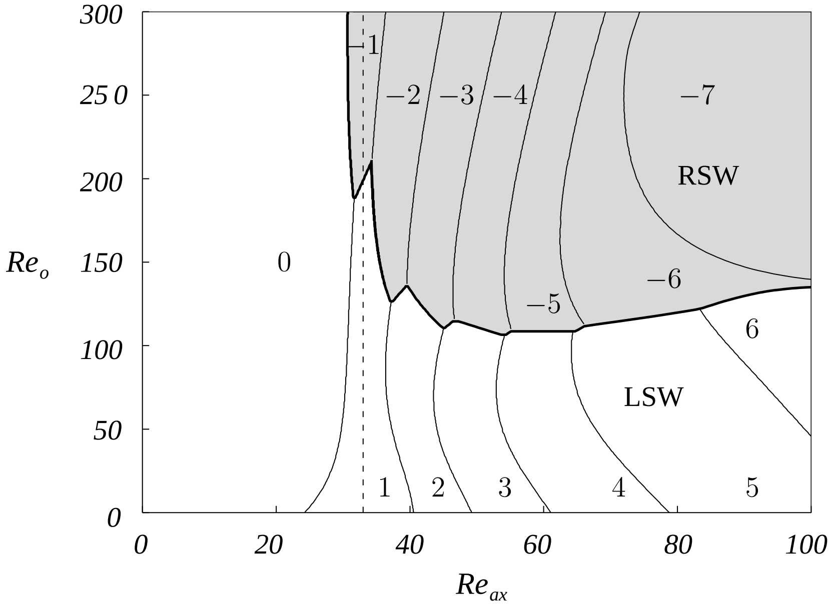

Figure 3.2: Projection of the critical surface $Re_i^c(Re_{ax}, Re_o)$ on the (Re_{ax}, Re_o)-plane (Meseguer & Marques, 2005*b*). Boundary curves separate regions where modes of different azimuthal wavenumber n (included in the plot) bifurcate at lowest Re_i. The bold line represents the bicritical boundary crossed by dashed line at $Re_{ax} = 33$.

regime the interaction between shear and centrifugal instabilities leads to mode competition. In particular, they found a bicritical Hopf curve where spiral waves of opposite axial propagation compete. Figure 3.2 shows a projection of the critical surface $Re_i = Re_i^c(Re_{ax}, Re_o)$ as computed by Meseguer & Marques (2005*b*), where the double Hopf curve (bold line) is shown. In the white region below the bicritical curve, Left-handed spiral waves (LSW) which propagate downstream, i.e in the direction of the imposed through flow, are dominant. In contrast, upstream propagating Right-handed spiral waves (RSW) are dominant in the gray region. LSW are characterized by positive azimuthal wavenumbers $n > 0$, depicted in the figure, whereas RSW are characterized by negative azimuthal wavenumbers.

In this chapter we present a study of the nonlinear dynamics arising in the neighborhood of a double Hopf point of the bicritical curve. For computational reasons, $Re_{ax} = 33$ (dashed line in figure 3.2) has been chosen to perform a comprehensive bifurcation analysis, since the bifurcated spirals feature the lowest non-zero azimuthal wavenumbers $n = \pm 1$. Figure 3.3(a) shows the neutral stability curves $(k, Re_{i,c})$ provided by linear stability analysis of SPF at $Re_{ax} = 33$ and $Re_o = 200.48$. The curves associated with the azimuthal modes $n_1 = -1$ and $n_2 = 1$ attain a common minimum Reynolds number $Re_i = 413.02$ at $k_{c,1} = 3.343$ and $k_{c,2} = 4.56$, respectively. This corresponds to the

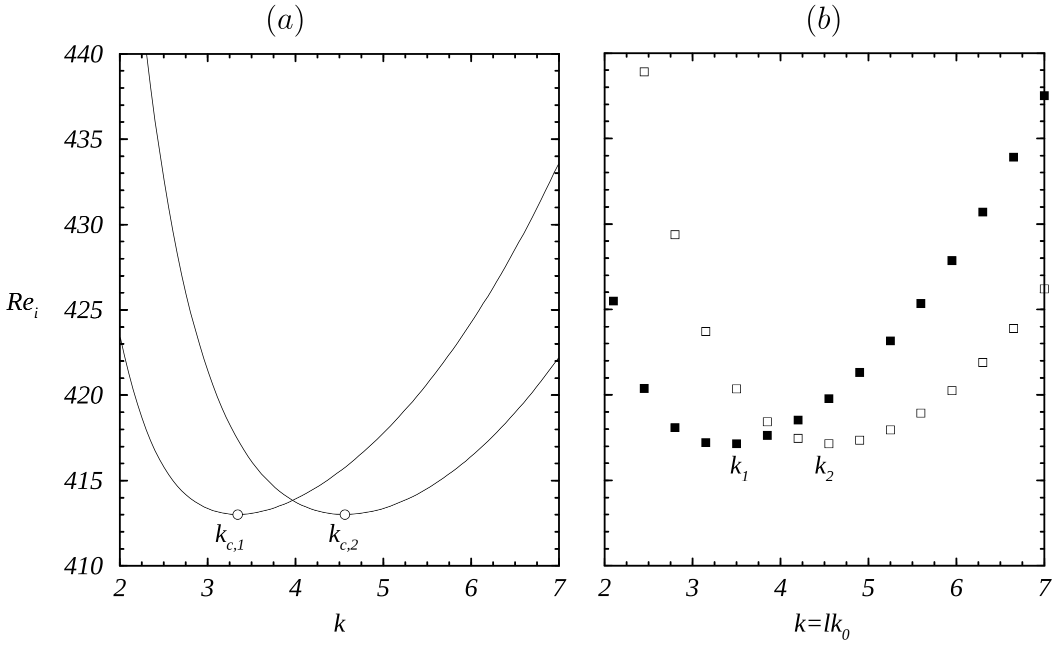

Figure 3.3: (a) Neutral stability curves of $n = \pm 1$ azimuthal modes at the bicritical point $(Re_{ax}, Re_o) = (33, 200.48)$ for k varying continuously. The white circles are located at the minima $k_{c,1}$ and $k_{c,2}$ of $n_1 = -1$ and $n_2 = 1$, respectively. (b) Same as (a) but for the discretization $k = lk_0$ with $k_0 = 0.35$ and $l \in [-66, 66]$. In this case the bicritical point is $(Re_{ax}, Re_o) = (33, 202.6)$.

double Hopf point

$$(Re_{ax}, Re_o, Re_i)^{\mathrm{dH}}_{\infty} = (33, 200.48, 413.02), \tag{3.6}$$

where ∞ sub-index refers to critical values computed assuming a continuous range of axial wave numbers k. When considering nonlinear computations, the spectrum of axial wave numbers becomes discrete (see §2.3), and it has to be fixed so that those modes responsible for the instability, as well as their harmonics, are resolved. At this point, a fundamental axial wavenumber k_0 in (2.17) has to be fixed so that the discretization covers the unstable dynamics.

In this chapter we use a spectral resolution consisting of $(L, M, N) = (66, 24, 8)$ modes along with $k_0 = 0.35$, leading to a periodic annulus of wavelength $\Lambda \sim 18$. The value of k_0 has been suitably chosen in order to capture the two values $k_{c,1} = 3.343$ and $k_{c,2} = 4.56$. This is accomplished by the axial discretization used, where the Fourier modes $(l_1, n_1) = (10, -1)$ and $(l_2, n_2) = (13, 1)$, rendering $k_1 = 10k_0 = 3.5$ and $k_2 = 13k_0 = 4.55$, consistently reproduce the nearby critical values of the continuum case. In addition, up to four harmonics of the two previous modes are also included in the dynamical system of amplitudes. Nevertheless, the resulting equispaced set of discretized axial wave numbers

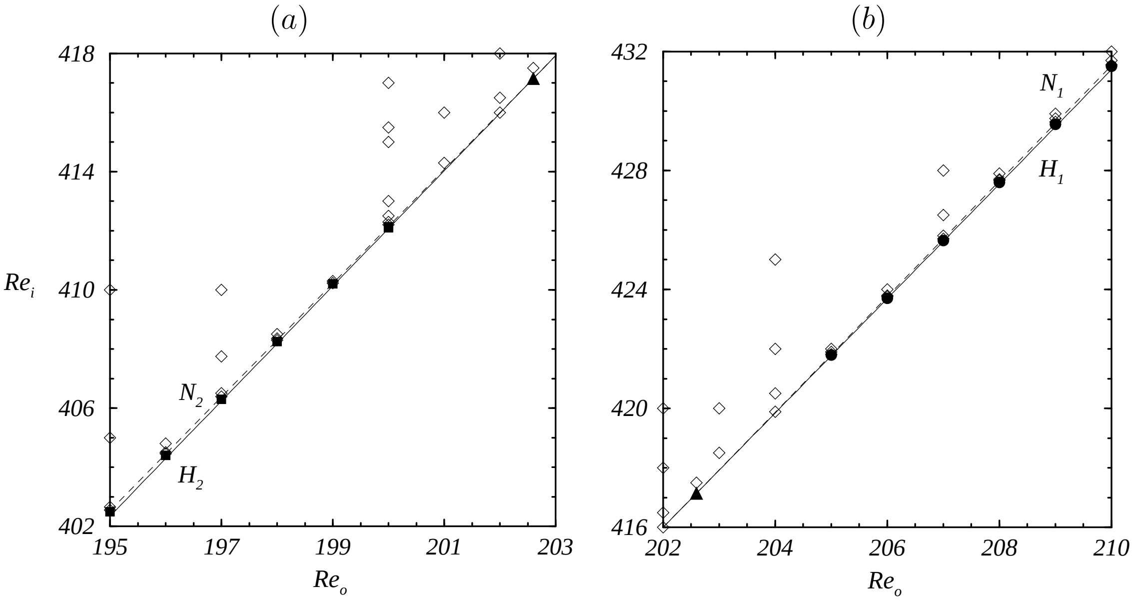

Figure 3.4: Loci of solutions type in (Re_o, Re_i)-space. Filled squares and circles are LSW and RSW, respectively, and diamonds are IPS. Solid (dashed) lines correspond to the Hopf (Neimark–Sacker) bifurcation curves. The double Hopf point (3.7) is indicated with a filled triangle.

lk_0 leads to minor discrepancies when trying to reproduce the instability mechanisms. This is mainly due to the fact that the critical Reynolds number Re_o at which these modes bifurcate simultaneously is slightly different from the ideal value $Re_o = 200.48$. This small discrepancy can be spotted from figure 3.3(b), where the neutral stability points $(lk_0, Ri_c)_{n=\pm1}$ attain a common critical value $Re_{i,c} = 417.15$ for $Re_o = 202.6$. As a result, the coordinates of the double Hopf bifurcation point based on our discretization are

$$(Re_{ax}, Re_o, Re_i)^{\mathrm{dH}} = (33, 202.6, 417.15). \tag{3.7}$$

Overall, the critical values of the spectral approximation differ nearly by 1% from the values obtained by linear stability computations using a continuous range of k.

Figure 3.4 shows the regime diagram of the competition between $n_1 = -1$ RSW and $n_2 = 1$ LSW in the neighborhood of the double Hopf point (3.7). The bifurcation curves in figure 3.4 are very close together. For clarity, these have been represented in figure 3.5 in (Re_o, ϵ)-space, where $\epsilon = Re_i - H_2(Re_o)$ and H_2 corresponds to the linear stability curve of the $n_2 = 1$ spiral mode. For Re_i and Re_o in region 1 the basic state SPF is the only flow that exists. Crossing the Hopf bifurcation curve H_1 into region 2, SPF become unstable and RSW emerge. Upon crossing into region 3, RSW become unstable via a Neimark–Sacker bifurcation N_1 to a regime of interpenetrating spirals

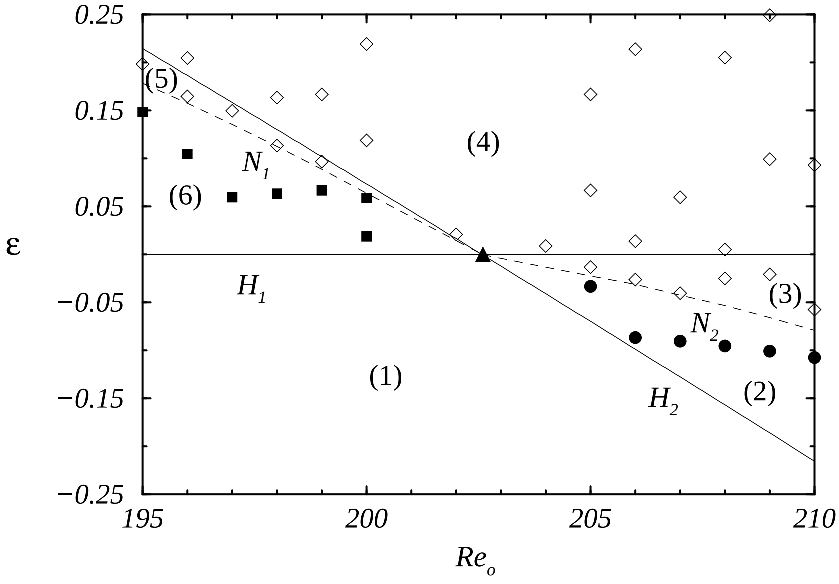

Figure 3.5: Loci of solutions type in (Re_o, ϵ)-space ($\epsilon = Re_i - H_2$). Filled squares and circles are LSW and RSW, respectively, and diamonds are IPS. Solid (dashed) lines correspond to the Hopf (Neimark–Sacker) bifurcation curves. The double Hopf point (3.7) is indicated with a filled triangle. Bracketed numbers correspond to regions in parameter space with qualitatively different dynamics. A schematic of their phase portraits are shown in figure 3.6.

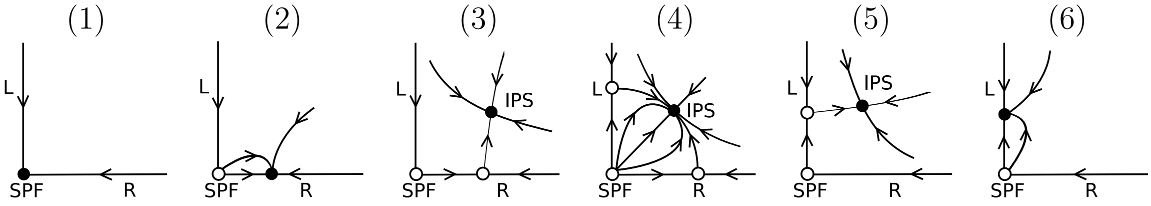

Figure 3.6: Generic phase portraits corresponding to the six different regions of the regime diagram in figures 3.4 and 3.5. Solid (open) circles are stable (unstable) states. See Appendix B for details.

(IPS). These consist of the superposition of RSW and LSW. The latter bifurcate at H_2 but are unstable in region 4. The situation is analogous when starting from region 1 and crossing H_2, N_2 and H_1 to reach region 4. The detailed analysis of this bifurcation is presented in Appendix B in terms of equivariant normal form theory. Figure 3.6 shows a schematic of the phase portraits in the six regions of parameter space indicating the stability of the flows, summarizing the results in the Appendix. The Hopf bifurcation curves H_1 and H_2 have been obtained with linear stability analysis of SPF for the discrete axial wavenumbers $k = lk_0$ in the nonlinear computations. Their intersection renders the double Hopf point (3.7). The Neimark-Sacker bifurcation curves N_1 and N_2

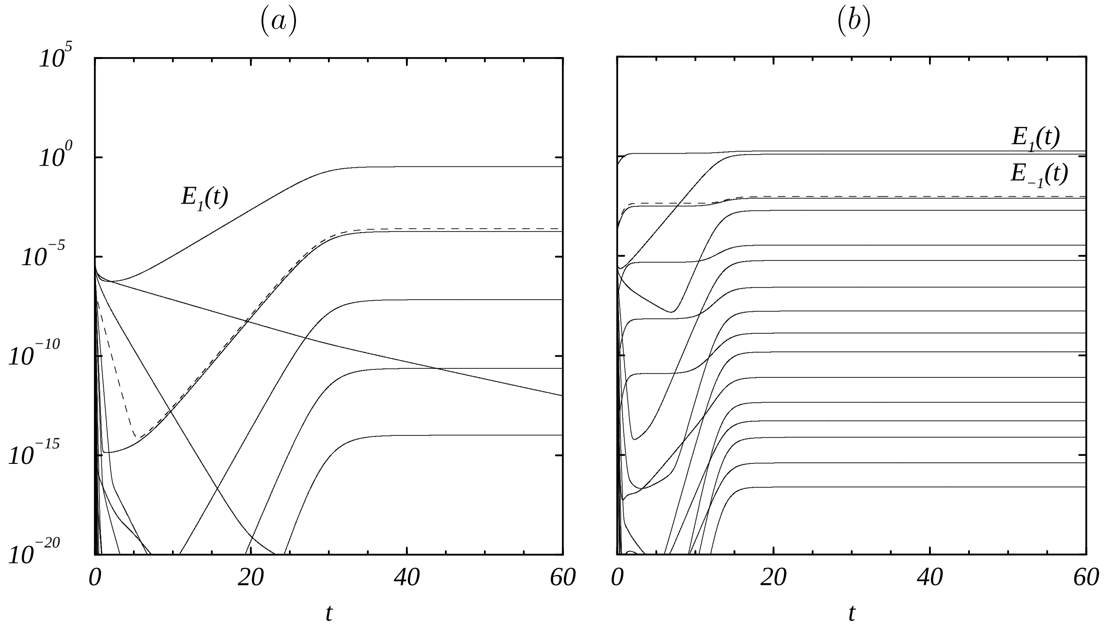

Figure 3.7: (a) Time evolution of the energy of the azimuthal Fourier modes, measured according to (2.28), during transition from SPF to LSW at $(Re_o, Re_i) = (190, 392.85)$. The solid upper line corresponds to the $n = 1$ mode generating the LSW, whereas the stagnated curves below $\mathrm{E}_n(t)$ correspond to harmonics of the leading unstable mode. (b) Same as (a) during transition from LSW to IPS at $(Re_o, Re_i) = (190, 393.5)$.

in figures 3.4 and 3.5 have been computed by time evolution, using the 3D Navier-Stokes solver. The stability of any solution is monitored in time through the measurement of the kinetic energy density associated with each azimuthal Fourier mode $\mathrm{E}_n(t)$ as defined in (2.28). Figure 3.7(a) shows an energy-time plot of the transition from SPF to LSW when crossing H_2 from below. In order to detect the Neimark-Sacker boundary N_2, the LSW were continued by subsequently increasing Re_i until they eventually became unstable, as shown in its energy-time evolution, see figure 3.7(b). In this case, the instability leads to quasi-periodic IPS. As shown in figure 3.4, the regions where LSW or RSW are stable are very narrow, whereas the IPS are stable in a much wider region of parameter space. Note that region 6, where LSW are stable, is slightly wider than region 2 where RSW are stable (figure 3.5). In addition, all the bifurcations observed were found to be supercritical.

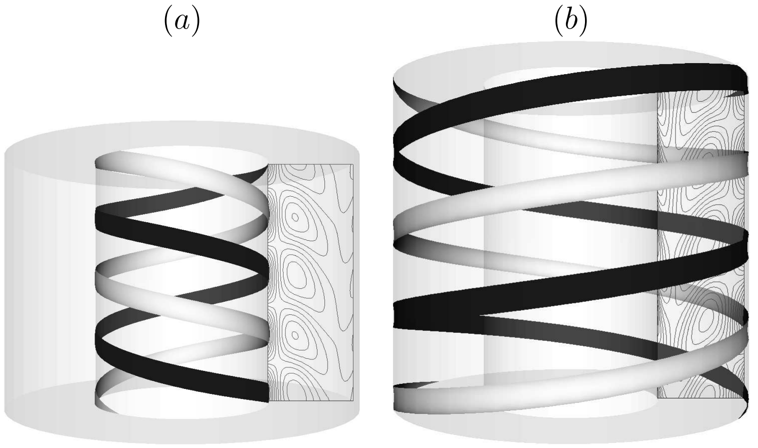

Figure 3.8: Isosurfaces of the azimuthal vorticity of the perturbation over two axial wavelengths of the patterns: (*a*) LSW at $(Re_o, Re_i) = (190, 392.8)$, $\omega_\theta = \pm 23$. (*b*) RSW at $(Re_o, Re_i) = (210, 431.5)$, $\omega_\theta = \pm 9.5$.

3.3 Characterization of the bifurcated flows

3.3.1 Left and Right spiral waves

The spiral patterns arising from Hopf bifurcations H_1 (RSW) and H_2 (LSW) break the rotational and translational symmetries of the problem. However, these solutions are time-periodic and, essentially, one-dimensional, since their dependence on t, z and θ occurs through the *phase variable* (Hoffmann *et al.*, 2004)

$$\phi = \omega t + l k_0 z + n\theta, \tag{3.8}$$

Therefore, these patterns rotate with angular speed $w_p = -\omega/n$ and propagate axially with phase speed $c = -\omega/(lk_0)$, so that the symmetries have become spatio-temporal, see Appendix B equations (B.28)–(B.29). These solutions retain a purely spatial symmetry, a combination of an axial translation T_a and a rotation R_α such that

$$l k_0 z + n\theta = 0, \tag{3.9}$$

corresponding to helical motion. Therefore the symmetry $H_\alpha = R_\alpha T_{-n\alpha/(lk_0)}$ generates a subgroup $SO(2)_H$ of $\mathcal{G}$, see Appendix B for details. These spiral patterns are simultaneously rotating and traveling waves, resembling a barber pole, and for this reason we use the term *spiral waves* for them. The geometrical shape of these solutions can be seen in figure 3.8, showing isosurfaces of azimuthal vorticity. Each spiral wave is composed of two spiral vortices with opposite vorticity (light and dark in the figure), within an axial wavelength.

LSW	Re_o	Re_i	ω_p	c/Re_{ax}
	195	402.5	397.7	2.65
	196	404.4	398.9	2.66
	197	406.3	400.0	2.66
	198	408.25	401.2	2.67
	199	410.2	402.4	2.68
	200	412.1	403.5	2.69

RSW	Re_o	Re_i	ω_p	c/Re_{ax}
	205	421.8	27.53	-0.24
	206	423.7	28.24	-0.24
	207	425.65	28.99	-0.25
	208	427.6	29.72	-0.26
	209	429.55	30.45	-0.26
	210	431.5	31.19	-0.27

Table 3.1: Angular and axial speeds of LSW and RSW measured at points located within the boundaries H_2-N_2 and H_1-N_1 of figure 3.4. The axial speed c of the patterns has been normalized with respect to the axial Reynolds number Re_{ax}.

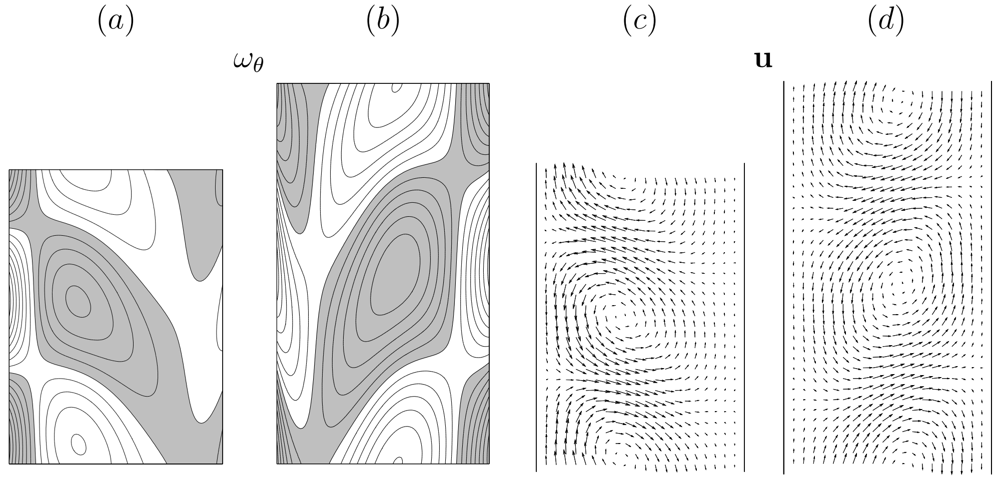

Figure 3.9: (a) and (b) show contours of azimuthal vorticity of the perturbation ω_θ evaluated over a θ-constant cross section for $(r, z) \in [r_i, r_o] \times [0, h_{L,R}]$ for LSW at $(Re_o, Re_i) = (190, 392.85)$ and RSW at $(Re_o, Re_i) = (210, 431.5)$, respectively. (c) and (d) correspond to perturbation vector field components (u_r, u_z). For clarity, the original aspect ratio has been preserved in the plots.

Within the explored regions between H_1-N_1 and H_2-N_2, the RSW and LSW are found to co-rotate with the cylinders, precessing with angular speeds of order $\omega_p^L \sim 400$ and $\omega_p^R \sim 30$, respectively. However, the LSW pattern exhibits a downstream phase speed c faster than the basic state axial mean velocity (measured by Re_{ax}), whereas the RSW slowly propagate upstream. It is shown in the Appendix that opposite axial propagation is a sufficient condition to inhibit resonances, thus the case of study is non-resonant. Accurate angular and axial speeds of these described patterns within their domains of stability are reported in Table 3.1. The LSW have an axial wavelength of $h_L = 1.38$ and are mainly concentrated on the inner cylinder wall, where strong azimuthal vorticity spots are generated, as shown in figure 3.9(a). On the other hand, the RSW have an axial

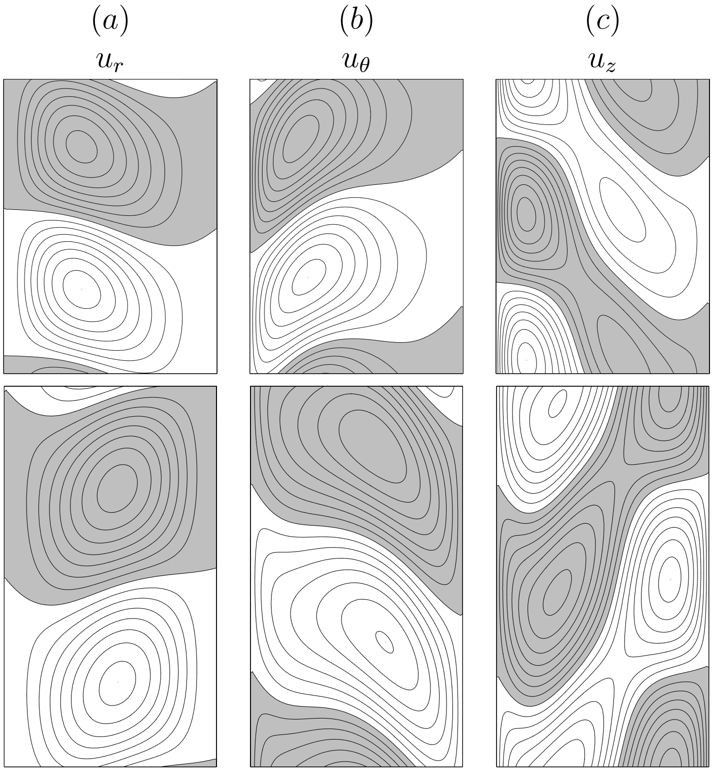

Figure 3.10: Contours of the perturbation field $\mathbf{u}$ evaluated over a θ-constant cross section for $(r, z) \in [r_i, r_o] \times [0, h_{L,R}]$. Top, LSW at $(Re_o, Re_i) = (190, 392.85)$ and bottom, RSW at $(Re_o, Re_i) = (210, 431.5)$. From left to right: (a) u_r, (b) u_θ and (c) u_z components. Gray and white regions stand for negative and positive or zero values, respectively.

wavelength of $h_R = 1.8$ but are mainly concentrated on the outer cylinder wall, where similar azimuthal vorticity spots are produced, as shown in figure 3.9(b). However, for the LSW the azimuthal vorticity is confined within a region close to the inner cylinder, whereas the RSW feature high values of the azimuthal vorticity along all the radial domain. Figures 3.9(c) and (d) show their perturbation velocity field $\mathbf{u}$ on a θ-constant cross section. The center of the vortices is slightly displaced towards the inner (outer) cylinder for the LSW (RSW). Figure 3.10 shows contours of the components of the perturbation velocity $\mathbf{u}$ for both solutions. Their maxima and minima are also located near the inner (LSW) or outer (RSW) cylinders, as happens with the azimuthal vorticity.

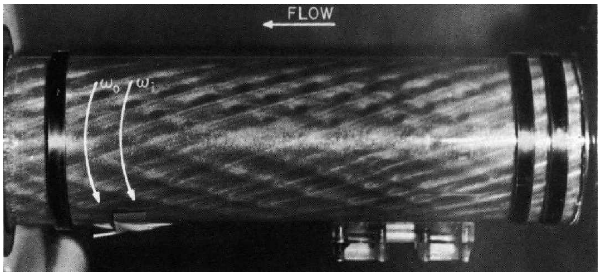

Figure 3.11: DSSF experimental flow found by Nagib (1972) for $Re_{ax} = 120$, $Re_o = 898$, $Re_i = 835$, and for small gap geometry with $\eta = 0.77$.

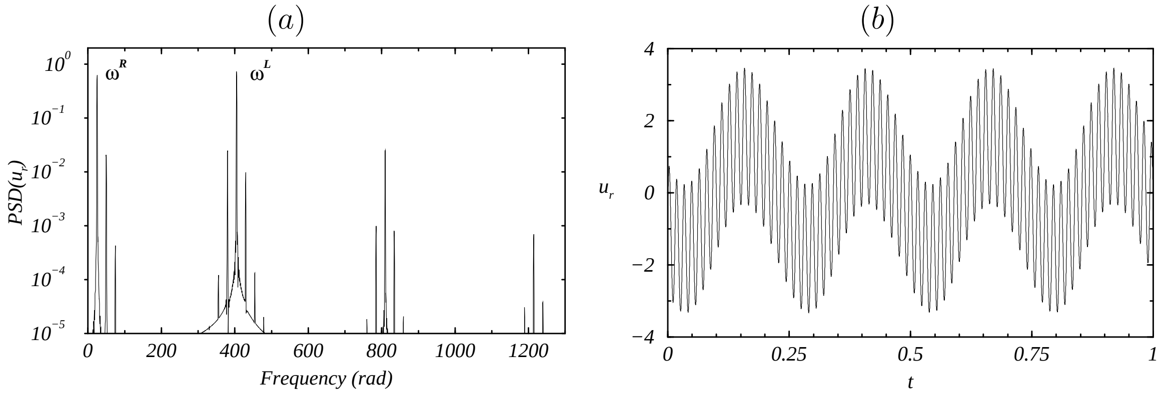

Figure 3.12: (a) Power spectral density of the IPS solution at $(Re_o, Re_i) = (201, 414.3)$. The two independent frequencies are very close to the frequencies of the unstable RSW ($\omega^R = 24.82$) and LSW ($\omega^L = -404.6$) solutions, respectively. (b) Time series of u_r for the IPS solution in (a).

3.3.2 Interpenetrating spirals

The interpenetrating spirals (IPS) consist of quasi-periodic regimes exhibiting the main features of the two limit cycles corresponding to LSW and RSW. Similar interpenetrating spirals regimes were found experimentally in the past by Nagib (1972), who termed them as *Double Spiral Secondary Flows* (DSSF). The experiments were carried out at higher Reynolds numbers Re_{ax}, Re_o, Re_i than our computations, and with a smaller gap $\eta = 0.77$. Figure 3.11 shows a photograph of the aforementioned DSSF found by Nagib (1972). Recent linear stability results Meseguer & Marques (2005a) suggest that these solutions come from a similar instability mechanism, although much higher azimuthal modes (typically within the range $13 \leq |n| \leq 15$) are responsible for the transition, rendering nonlinear computations unaffordable. The dependence of the IPS on t, z and

IPS	Ro	Ri	ω_p^L	c^L/Re	ω_p^R	c^R/Re
	195	402.65	397.7	2.65	20.42	-0.18
	198	408.5	401.2	2.67	22.62	-0.20
	201	414.3	404.6	2.69	24.82	-0.21
	204	422	408.7	2.72	28.27	-0.24
	207	426.5	411.9	2.74	29.53	-0.26
	210	432	415.3	2.77	31.73	-0.27

Table 3.2: Angular and axial speeds of the IPS measured at some points located over N_1 and N_2 curves of figure 3.4.

θ happens through the two independent phase variables

$$\phi^L = \omega^L t + k^L z + \theta, \tag{3.10}$$

$$\phi^R = \omega^R t + k^R z - \theta, \tag{3.11}$$

corresponding to the unstable LSW and RSW. This fact, predicted in Appendix B using normal form theory, is confirmed by the good agreement between the frequencies observed in the IPS regime and the eigenfunctions of the linear stability problem that generate LSW and RSW (disagreement below a 0.5%). The power spectral density of the IPS is plotted in figure 3.12(a), where the associated LSW and RSW frequencies and their harmonics are clearly observed. The two frequencies differ in more than one order of magnitude, being ω^R about 16 times larger than ω^L. They can be clearly observed in the time series of the radial velocity at a convenient point, shown in figure 3.12(b). The IPS regime can be interpreted as a superposition of two waves, with phases ϕ^L and ϕ^R, corresponding to LSW and RSW respectively, but precessing with different angular speeds while propagating downstream and upstream respectively. Angular and axial speeds of both waves are also provided in Table 3.2. Figure 3.13 shows isosurfaces of the azimuthal vorticity and helicity of the perturbation velocity field $\mathbf{u}$, illustrating that the waves associated with the LSW and RSW are clustered on the inner and outer cylinder, respectively. In order to illustrate the opposite axial propagation of the LSW and RSW components of the interpenetrating spirals IPS, several snapshots of the azimuthal vorticity at different times are shown in Fig. 3.14, where the two periods $T^L = 2\pi/\omega^L \simeq 0.016$ and $T^R = 2\pi/\omega^R \simeq 0.25$ have been considered. In the first row, covering one T^L period, we observe the downstream propagation associated with the LSW, clearly concentrated on the inner cylinder. In the second row, covering one T^R period, the upstream propagation associated with the RSW is observed on the outer cylinder (note that downstream propagation corresponds to motion on the positive axial direction in the plots). The interaction of the two spiral waves, RSW and LSW,

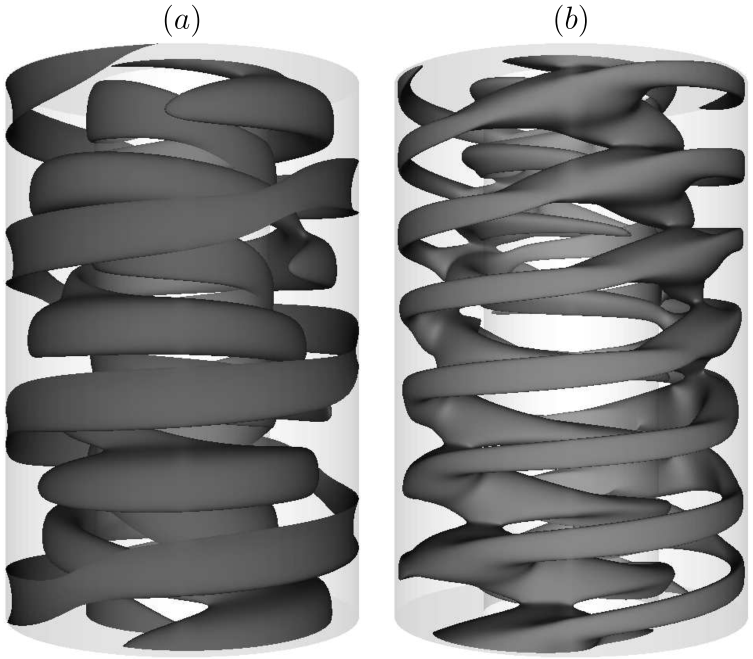

Figure 3.13: Isosurfaces of the IPS solution at $(Re_o, Re_i) = (201, 414.3)$, $z \in [0, \Lambda/3]$. (a) Azimuthal vorticity of the perturbation at level $\omega_\theta = -10$. (b) Helicity of the perturbation $H = \mathbf{u} \cdot (\nabla \times \mathbf{u})$ at level $H = 0.2$.

with different periods and axial wavelengths, makes it difficult to analyze the resultant pattern, except where one of the spiral waves is clearly dominant, i.e., close to the inner or the outer cylinder. The interpenetrating spirals IPS are quasi-periodic both in space and time. Quasi-periodicity in time is clearly manifested in figure 3.12(b). Figure 3.15 shows the vector field $\mathbf{u}$ and contours of its components on a θ-constant section for the IPS regime. The radial-azimuthal velocity field clearly shows a non uniform cell-height throughout the cross section, as a result of the incommensurate wavelengths of the RSW and LSW spiral waves. The superposition of the two coexisting solutions is better seen in the azimuthal velocity contours (third column of figure 3.15), where a Λ-shape is identified close to the mean radius. The axial wavelengths corresponding to the LSW (RSW) can still be identified close to the inner (outer) cylinder in the contours for u_r (compare with figure 3.10).

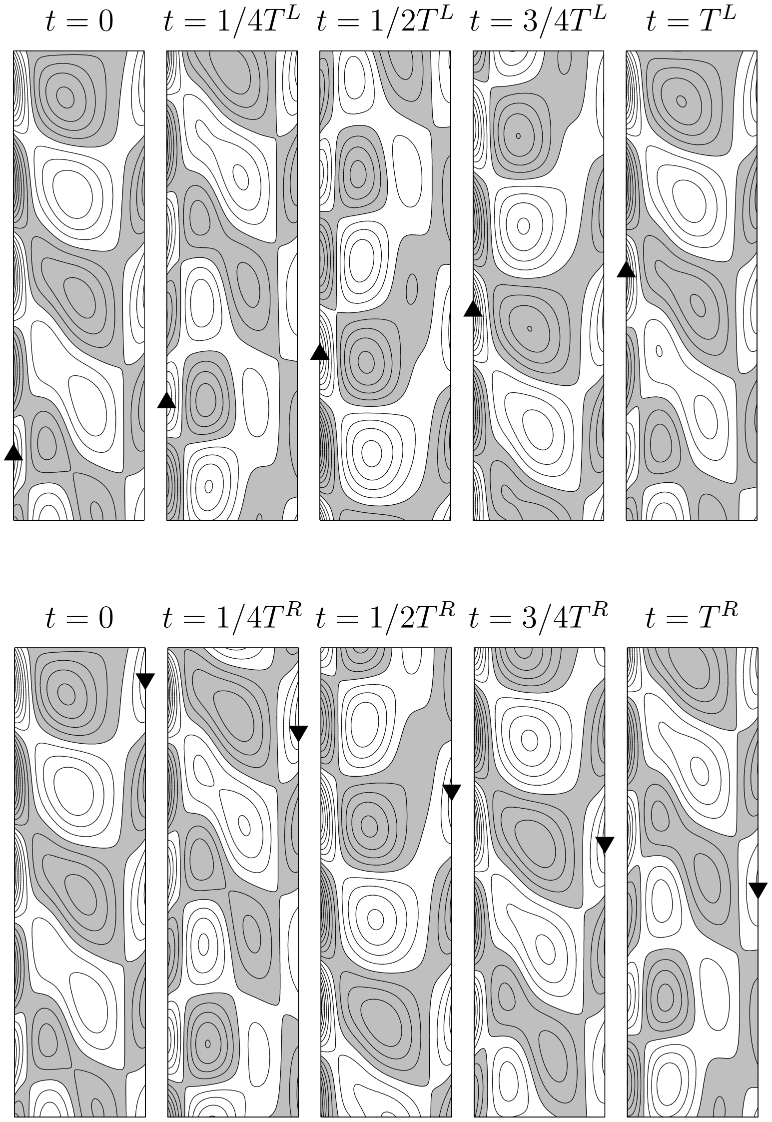

Figure 3.14: Contours of the azimuthal vorticity of the perturbation, ω_θ, for the IPS at $(Re_o, Re_i) = (201, 414.3)$ evaluated over a θ-constant cross section for $(r, z) \in [r_i, r_o] \times [0, 2h_R]$. The first (second) row illustrates the upward (downward) propagation associated to the LSW (RSW), indicated with ▲ (▼).

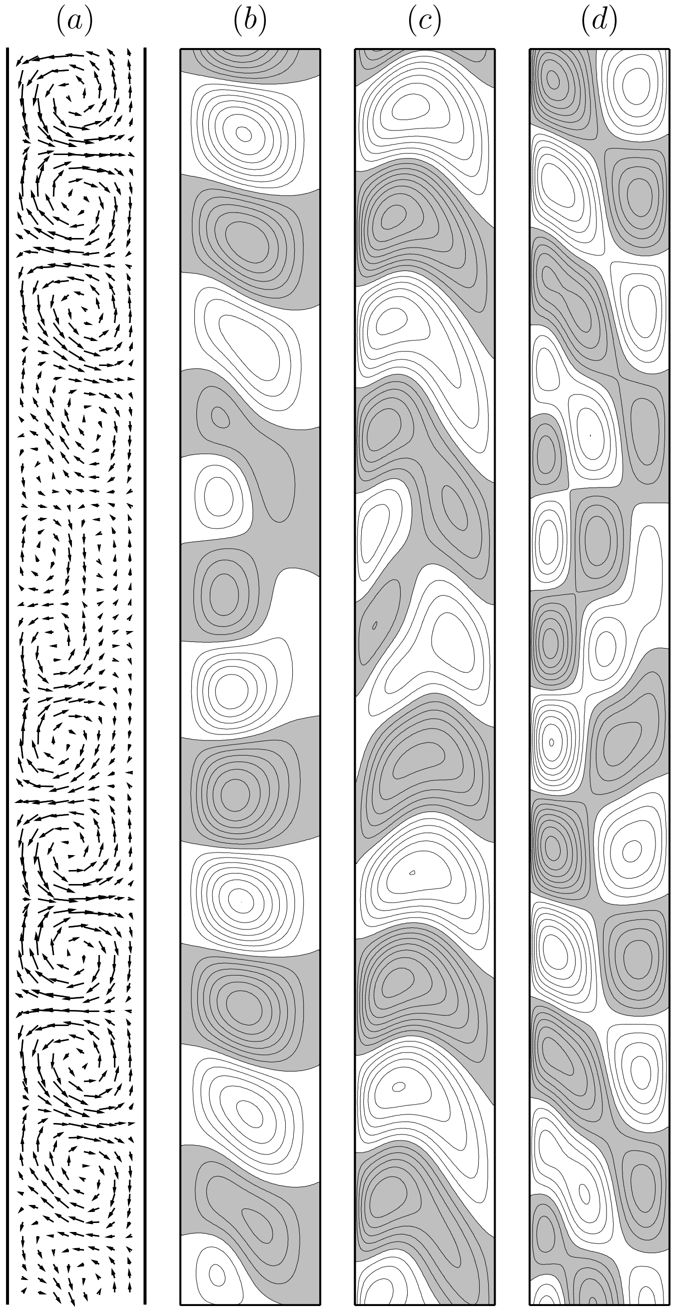

Figure 3.15: Perturbation vector field **u** corresponding to the IPS solution at $(Re_o, Re_i) = (201, 414.3)$ evaluated on a θ-constant cross section for $(r, z) \in [r_i, r_o] \times [0, \Lambda/2]$. (*a*) Vector field (u_r, u_z), (*b*) contours of u_r, (*c*) contours of u_θ, (*d*) contours of u_z.

3.4 Conclusions

Nonlinear dynamics of the co-rotating spiral Poiseuille flow have been investigated. The explorations have been focused on a neighborhood of a double Hopf point where low azimuthal modes compete. Numerical simulations confirm that spiral waves of opposite wave number $n = \pm 1$ and a mixed mode of interpenetrating spirals are born at the double Hopf bifurcation. All these flows break both $SO(2)$ symmetries, though in the case of the spiral waves, the symmetries become spatio-temporal. The numerical exploration for different inner/outer cylinder velocities has been combined with Normal form analysis with the symmetry group $\mathcal{G} = SO(2) \times SO(2)$, allowing the identification of the bifurcation scenario corresponding to this problem. This analysis, presented in Appendix B, shows that the symmetry group $\mathcal{G}$ does not alter the generic normal form but imposes a stronger constraint for resonance, rendering the present case of study non-resonant.

The dominant flow is the quasi-periodic state IPS, which is stable in a wide region of parameter space, confining the periodic spiral waves to very narrow parameter regions. LSW and RSW can be viewed as rotating and traveling waves which precess with independent angular speeds, co-rotating with the cylinders, but exhibit opposite stream-wise phase propagation. The stability region for the downstream traveling LSW is slightly wider than the upstream RSW, as observed in the counter-rotating case by Hoffmann *et al.* (2004). The stable IPS can be regarded as the superposition of both pure mode solutions. The features of the LSW and RSW regimes can be observed close to the inner and outer cylinder respectively, where one or the other are dominant. The spatio-temporal properties of the computed solutions are in very good agreement with bifurcation theory predictions provided.

The coexistence of spiral patterns of opposite helical orientation and stream-wise propagation had been formerly observed experimentally in this problem for much higher angular speeds of the cylinders and also for narrow gap geometries, where the dominant azimuthal modes at transition are one order of magnitude larger than in the present study, thus being extremely expensive a well-resolved computation with current computational capabilities.

Above the studied range of inner and outer angular speeds, additional bifurcations take place, and the dynamics may exhibit more complex mode interactions. These issues will be addressed in future works.

CHAPTER 4

AXIALLY OSCILLATING TAYLOR–COUETTE FLOWS

Hu & Kelly (1995) first considered temporal modulations of both Poiseuille flow and axial sliding in the open Taylor–Couette system. They performed a Floquet analysis of the resulting periodic basic states and showed that both mechanisms are more efficient in delaying transition than the corresponding steady flows. Their results motivated the experimental work of Weisberg, Kevrekidis & Smits (1997), who investigated axial oscillations of the inner cylinder to verify the theoretical predictions of Hu & Kelly (1995). However, the agreement between the experiments and the numerical Floquet analysis was only qualitative. Marques & Lopez (1997) showed that the discrepancy was due to the presence of endwalls in the experimental apparatus in contrast to the open flow system considered by Hu & Kelly (1995), where mass is conserved only after a forcing period. Following Edwards *et al.* (1991), the Floquet analysis by Marques & Lopez (1997) accounted for the leading order effects of the presence of endwalls by imposing a zero axial mass flow, and despite the fact that their model retained the idealization of infinitely long cylinders, the agreement with the experiments was excellent.

Although the transition when the inner cylinder is forced to oscillate harmonically in the axial direction is generally via a synchronous bifurcation to axisymmetric cells, Marques & Lopez (1997) noted that for small frequencies and large amplitudes of the axial oscillations there are some windows of parameter space where the transition is via a Neimark–Sacker bifurcation (a Hopf bifurcation from a periodic orbit) to non-axisymmetric spiral flow. In this case, the time periodic basic state bifurcates to a quasi-periodic torus featuring the forcing frequency, ω_f, and the frequency of the spiral mode, ω_s. These windows of parameter space were investigated by Marques & Lopez (2000) using Floquet analysis to identify the presence of several strong resonances, i.e. $\omega_s/\omega_f = p/q$ with $q \leq 4$. That linear analysis motivated the recent experiments by Sinha *et al.* (2006) who investigated the associated nonlinear dynamics and identified regions of quasi-periodic motion and frequency-locking, as well as observing the torus to break up for higher post-critical values of the Reynolds number. However, the results they obtained were noisy even for Reynolds numbers very close to critical. The signals they analyzed contained additional frequencies which were not a linear combination of ω_f and ω_s, and were attributed to background noise.

In order to shed light on the transition to complex behavior in periodically forced systems and clarify the results of Sinha *et al.* (2006), we have numerically solved the unsteady Navier–Stokes equations. We have found that subsequent bifurcations occurring

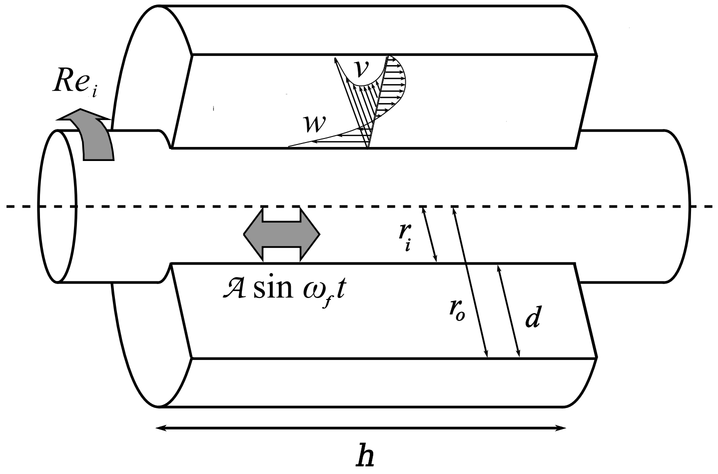

Figure 4.1: Schematic of Taylor–Couette flow with axial oscillations of the inner cylinder.

very close to onset of the first instability of the basic state, which are not detectable in the experiments due to the precision that can be achieved, destroy the torus and introduce additional independent frequencies into the solutions. Moreover, our theoretical analysis, presented in Appendix C, shows that due to the symmetries of the system under consideration, frequency-locking is not possible until the bifurcating flow has broken the translational and rotational symmetries. As this happens by the introduction of new independent frequencies, any observed frequency-locking must be only partial and therefore does not involve periodic flow.

4.1 Numerical methods and symmetries

We consider the Taylor–Couette system with rotating inner cylinder and stationary outer cylinder. In addition, the inner cylinder executes harmonic oscillations in the axial direction. The dimensionless dynamical parameters governing this system are the inner cylinder Reynolds number Re_i and the amplitude and frequency of the oscillations, $\mathcal{A}$ and ω_f, respectively.

Figure 4.1 shows a schematic of the flow. The experimental apparatus of Sinha *et al.* (2006) had a radius ratio of $\eta = 0.905$, and we have used the same value in our computations. Moreover, in the experiment the amplitude and frequency of the axial motion were mechanically coupled such that $\omega_f = \mathcal{A}/9.525$; we have used this relationship in our computations presented here.

The boundary conditions of the axially oscillating Taylor–Couette system in cylindrical coordinates read

$$\mathbf{v}(r_i,\theta,z,t) = (0, Re_i, \mathcal{A}\sin\omega_f t) \quad \mathbf{v}(r_o,\theta,z,t) = \mathbf{0}. \tag{4.1}$$

In the experiments of Sinha *et al.* (2006), the aspect ratio of the annulus is very large, $h/d = 152$. We assume periodicity in the axial direction and account for the leading order effects of the presence of endwalls by imposing a zero net axial mass flow at every instant in time (*enclosed flow* condition),

$$\dot{m}(\mathbf{v}) = \rho\int_S \mathbf{v}\cdot\mathbf{n}\,dS = \rho\int_{r_i}^{r_o}\int_0^{2\pi} w\,r\,d\theta\,dr = 0, \tag{4.2}$$

where S is any constant z-section. This is accomplisehd by imposing an axial pressure gradient which includes a linear term on z, i.e. $p = p_0 z + p_1(r,\theta,z,t)$.

4.1.1 Basic flow

We look for a basic flow independent of the axial and azimuthal directions, $\mathbf{v}_b(r,t) = (0, v_b, w_b)$. In this case, the Navier–Stokes equations (2.1) reduce to

$$\partial_t v_b = \big(\partial_{rr} + \frac{1}{r}\partial_r - \frac{1}{r^2}\big)v_b \tag{4.3}$$

$$\partial_t w_b = \big(\partial_{rr} + \frac{1}{r}\partial_r\big)w_b - p_0 \tag{4.4}$$

with boundary conditions (4.1) and w satisfying the enclosed flow condition (4.2). The resulting basic flow is $T_f = 2\pi/\omega_f$ periodic and consists of the superposition of circular Couette flow and an axial annular Stokes flow,

$$\mathbf{v}_b = \Big(0, \frac{\eta Re_i}{1-\eta^2}\Big(\frac{r_o}{r} - \frac{r}{r_o}\Big), \mathcal{A}\,\Im\big(f(r)\,\mathrm{e}^{\mathrm{i}\omega_f t}\big)\Big). \tag{4.5}$$

Here $f(r)$ is the solution of a second order ODE satisfying the boundary conditions of the problem and the enclosed flow condition,

$$\mathrm{i}\,\omega_f f = f'' + \frac{1}{r}f' - p_0, \tag{4.6}$$

$$f(r_i) = 1, \quad f(r_o) = 0, \tag{4.7}$$

$$\int_{r_i}^{r_o} f(r)\,dr = 0. \tag{4.8}$$

An explicit solution involving modified Bessel functions is given in Marques & Lopez (1997), along with asymptotic expansions and other properties of f, but it is more convenient to numerically compute f by solving (4.6)–(4.8) with efficient spectral methods.

We have used collocation at Gauss-Lobatto points as in the nonlinear Petrov–Galerkin scheme of chapter 2. Equation (4.6)–(4.8) are solved by writing $f = g + \mathrm{i}\, h$ and discretising the resulting equations for g and h in the Gauss–Lobatto points r_j

$$(D^2_{ij} + \frac{1}{r_j} D_{ij}) g_j + \omega_f h_j - \Re(p_0) = 0, \tag{4.9}$$

$$(D^2_{ij} + \frac{1}{r_j} D_{ij}) h_j - \omega_f g_j - \Im(p_0) = 0, \tag{4.10}$$

$$\sum_j w_j\, g_j = 0, \quad \sum_j w_j\, h_j = 0, \tag{4.11}$$

where D_{ij} and D^2_{ij} are the associated Chebyshev differentiation matrices of first and second order, and w_j are the Clenshaw–Curtis quadrature weights (Trefethen, 2000).

4.1.2 Zero mass flow perturbations

In order to perform nonlinear computations using the Petrov–Galerkin scheme, one has to enforce the zero net axial mass flow not only on the basic flow $\mathbf{v}_b$, but also on the perturbation $\mathbf{u}$, so that the full velocity field $\mathbf{v} = \mathbf{v}_b + \mathbf{u}$ satisfies the enclosed flow condition (4.2). Let us recall the form of the spectral approximation for the perturbation $\mathbf{u}$

$$\mathbf{u}(r, \theta, z, t) = \sum_{l=-L}^{L} \sum_{n=-N}^{N} \sum_{m=0}^{M} a_{lnm}(t) \mathrm{e}^{\mathrm{i}(lk_0 z + n\theta)} \mathbf{u}_{lnm}(r). \tag{4.12}$$

Since $\int_0^{2\pi} \mathrm{e}^{in\theta} d\theta = 0$, the modes with $n \neq 0$ do not contribute to (4.2). Moreover, as the net axial mass flow must be independent of the section S, the modes with $l \neq 0$ do not contribute to (4.2). This may be rewritten as

$$\dot{m}(\mathbf{u}) = 2\pi\rho \sum_{m=0}^{M} a^{(2)}_{00m}(t) \int_{r_i}^{r_o} h_m(r)\, r\, dr = 0. \tag{4.13}$$

In order to enforce equation (4.13) we use the technique in the previous section and introduce a time dependent constant axial pressure gradient $p_0'(t)$ in the Navier–Stokes equations for the perturbation (2.19)

$$\partial_t \mathbf{u} = -\nabla q + \Delta \mathbf{u} - (\mathbf{v}_B \cdot \nabla)\mathbf{u} - (\mathbf{u} \cdot \nabla)\mathbf{v}_B - (\mathbf{u} \cdot \nabla)\mathbf{u} - p_0'(t)\, \mathbf{e}_z. \tag{4.14}$$

After introducing the physical basis in (4.14) and projecting over the test basis, the pressure term $p_0'(t)\mathbf{e}_z$ only appers in the equation for the $(l, n) = (0, 0)$ compoment of

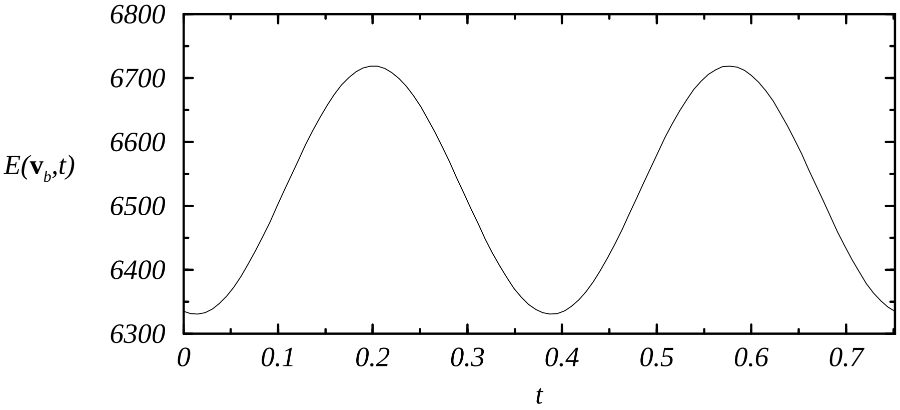

Figure 4.2: Kinetic energy time series of basic flow (4.5) over a forcing period. The parameter values are $Re_i = 200$, $\mathcal{A} = 79.6$.

the physical basis. Therefore the dynamical system involving the amplitudes (2.25) is modified only in the equation for a_{00m},

$$\mathbb{A}_{00r}^{00m}\frac{da_{00r}}{dt} = \mathbb{B}_{00r}^{00m}a_{00r} - \mathbb{N}_{00m}(a,a) - p_0'(t). \tag{4.15}$$

Equation (4.13) is discretized using the Clenshaw–Curtis quadrature and added to system (4.15). Together they are solved for $p_0'(t)$ and a_{00m} at each time step.

4.1.3 Symmetries and axial periodicity

The governing equations and boundary conditions are invariant under rotations R_α about and translations T_a along the common axis of the cylinders. Rotations generate the symmetry group $SO(2)$, and due to the imposed axial periodicity, axial translations generate another $SO(2)$ symmetry group. As both actions commute, the group of spatial symmetries of the system is $\mathcal{G}_0 = SO(2) \times SO(2)$. There is an additional spatio-temporal symmetry S, which consists of a time translation of half a period, $\phi^{T/2}$, followed by a reflection about a plane orthogonal to the cylinder axis K_z (acting as $z \to -z$). The actions of these on the velocity are:

$$R_\alpha(\mathbf{v})(r,\theta,z) = \mathbf{v}(r,\theta+\alpha,z), \tag{4.16}$$

$$T_a(\mathbf{v})(r,\theta,z) = \mathbf{v}(r,\theta,z+a), \tag{4.17}$$

$$K_z(\mathbf{v})(r,\theta,z) = (v_r, v_\theta, -v_z)(r,\theta,-z), \tag{4.18}$$

$$\phi^{T/2}(\mathbf{v})(r,\theta,z,t) = \mathbf{v}(r,\theta,z,t+T/2). \tag{4.19}$$

$S = K_z \circ \phi^{T/2}$ commutes with rotations but not with translations: $ST_a = T_{-a}S$. If S were purely spatial, i.e. the reflection K_z, then S and T_a would generate the orthogonal group,

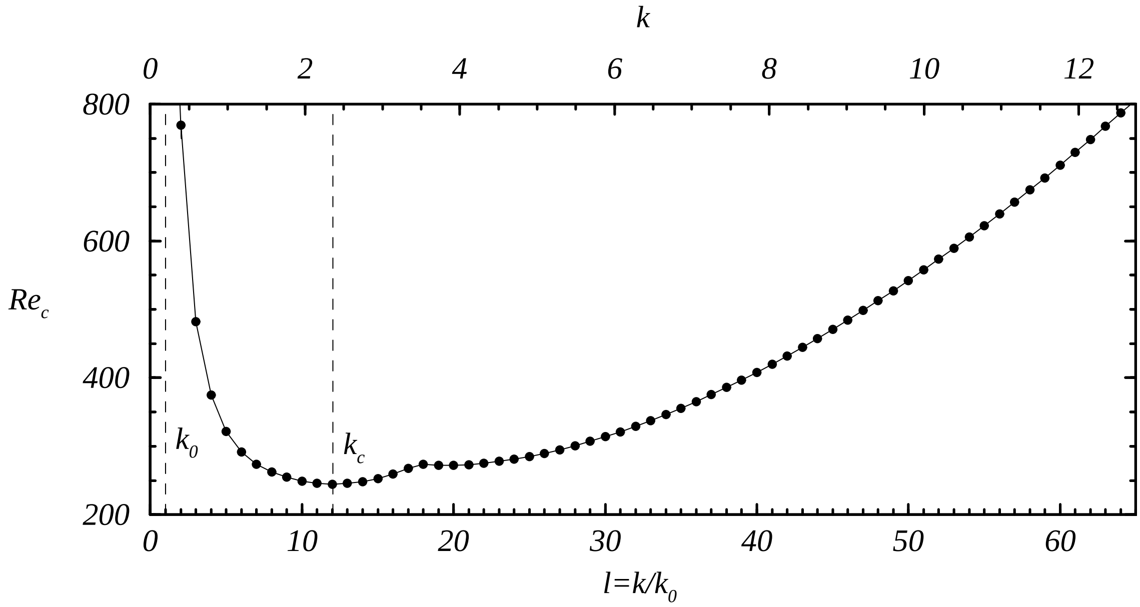

Figure 4.3: Neutral stability curve of the azimuthal modes $n = \pm 1$ for $\mathcal{A} = 79.25$ as computed with Floquet analysis. The circles are the discrete set of axial wavenumbers corresponding to the Fourier modes used in the nonlinear computations (4.12). The first Fourier mode $(l, n) = (1, 1)$, with smallest axial wavenumber $k = k_0 = 0.196$, is not shown as the corresponding $Re_{i,c} = 16\,256$ is off the scale of the plot. The most unstable mode is $(l, n) = (12, 1)$, with axial wavenumber $k = 12k_0 = 2.35$, which is very close to the critical axial wavenumber of the infinite case $k_c = 2.36$.

$O(2) = SO(2) \rtimes Z_2$ (semidirect product), where the elements of Z_2 would be K_z and the identity. As S is a space-time symmetry, S and T_a generate a space-time symmetry group isomorphic to $O(2)$, $O(2)^{ST} = SO(2) \rtimes Z_2$, where now the elements of Z_2 are S and the identity. The complete symmetry group of the problem is $\mathcal{G} = SO(2) \times O(2)^{ST}$. The basic flow (4.5) is invariant under $\mathcal{G}$. Figure 4.2 shows a kinetic energy time series of the basic flow over a forcing period T_f. Due to the spatio-temporal symmetry S, the time series is $T_f/2$ periodic, the two peaks corresponding to the forcing at maximum amplitude and opposite axial directions of the motion of the inner cylinder.

It is important to note that in many studies of flows in long cylinders, a spatial periodicity of wavelength $\lambda_c = 2\pi/k_c$ in the axial direction is assumed (where k_c is the critical axial wavenumber obtained from linear stability analysis). This assumption, which corresponds to fixing $k_0 = k_c$ in (4.12), renders the $l = 1$ axial mode as the only one unstable in the parameter regime of study and results in the computations being unable to investigate the competition between different spatial modes (except in the exceptional cases that their wavelengths are in simple rational ratios). If this imposed axial periodicity is destroyed in subsequent bifurcations due to mode competition, as is the case in the present problem, a larger axial periodicity $\Lambda = 2\pi/k_0$, with $k_c < k_0$ must be considered instead. Here, we have used a fundamental axial wavenumber of $k_0 = 0.196$, leading to periodic cylinders of wavelength $\Lambda \sim 32$. This value of k_0 has been chosen in order to capture the dynamics arising in the neighborhood of the resonant point $\mathcal{A} = 79.25$, $Re_{i,c} = 244.74$ (identified in the Floquet analysis). In particular, the $(l, n) = (12, \pm 1)$ Fourier modes in the expansion (2.17) have an axial wavenumber of $k = 12k_0 = 2.35$, which is very close to the critical axial wavenumber of the infinite case $k_c = 2.36$. Overall, with a spectral resolution consisting of $(L, M, N) = (65, 16, 20)$ modes our discretizaion includes up to four harmonics of the most dangerous modes ($l = 11, 12, 13$). Figure 4.3 shows the neutral stability curve of the azimuthal modes $n = \pm 1$ for $\mathcal{A} = 79.25$, found using Floquet analysis. The discrete axial wavenumbers considered in the nonlinear computations are shown as filled symbols on the curve. The discretization of the problem is still periodic, so the wavenumber ratio between different competing modes is rational, but our discretization allows for rational ratios with large denominators. The interaction of these modes is practically indistinguishable from truly quasi-periodic solutions.

4.2 Transition to complex spatio-temporal dynamics

The experiments of Weisberg *et al.* (1997) and the Floquet analysis of Marques & Lopez (1997) showed that the stability of Couette flow can be greatly enhanced by harmonic axial motion of the inner cylinder. Although this forcing stabilizes both axisymmetric and non-axisymmetric modes, there are windows in parameter space where the onset of instability is to spiral modes via a Neimark–Sacker bifurcation (a Hopf bifurcation from a periodic orbit). Marques & Lopez (2000) showed that in these windows strong resonances between the Neimark–Sacker frequency ω_s and the forcing frequency ω_f occur, motivating the recent experiments by Sinha *et al.* (2006) who studied the complex nonlinear dynamics subsequent to the Neimark–Sacker bifurcation. Nevertheless, their results contained additional frequencies which could not be identified and were attributed to background noise.

We show that these additional frequencies are due to subsequent bifurcations taking place very close to the first onset of instability. The increments in Re_i at which these additional bifurcations occur are so small (about 0.4%) that they cannot be detected with the precision that could be achieved in the experiments (the experimental uncertainty in Re_i was about 3%). A consequence of this rapid succession of bifurcations following

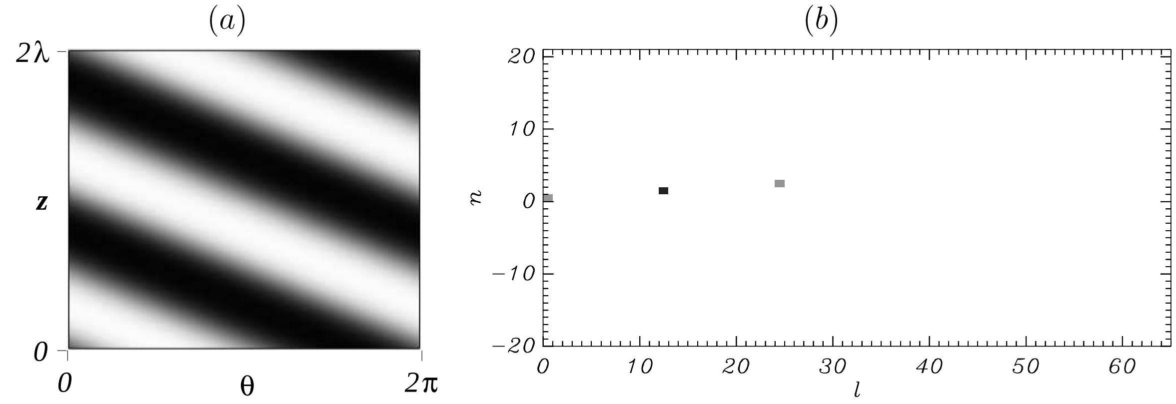

Figure 4.4: (*a*) Planar (θ, z) rendering of a gray-scale snapshot of the azimuthal vorticity of the perturbation $\mathbf{u}$ at the outer cylinder $r = r_o$, where black (white) corresponds to positive (negative) values. In (*b*) a snapshot of the kinetic energies of the Fourier modes $\mathrm{E}_{ln}(t)$ is shown in a logarithmic gray-scale map, where black corresponds to the energy of the leading mode and white to a level seven orders of magnitude lower. The flow is M1 at $\mathcal{A} = 79.6$ and $Re_i = 246.32$.

the loss of stability of the temporally forced Couette flow is that the resulting state has much greater spatio-temporal complexity than the unforced state at the same Re_i (which is the wavy vortex flow). Therefore, there is a trade-off between the enhanced stability and the spatio-temporal complexity of the flows once instability has arisen. For the axial forcing amplitudes considered in the experiments and here ($\mathcal{A} \sim 80$), the critical Reynolds number $Re_{i,c}$ for instability of Couette flow is about 80% higher than in the unforced case. Nevertheless, for the axially forced case the flow begins to lose regularity in axial and azimuthal wavenumber for $Re_{i,c}$ about 2% above criticality due to the sequence of bifurcations.

4.2.1 Onset of instability

The spiral modes predicted by the Floquet analysis of Marques & Lopez (2000), from now on are referred to as Mode 1 (M1), bifurcate supercritically from the oscillating basic state (4.5) in a Neimark–Sacker bifurcation. They are characterized by their axial and azimuthal wavenumbers (k, n) which define a constant spiral angle $\beta = \tan^{-1}(-n/k)$. In particular, the full nonlinear solution is of the form $\mathbf{f}(r, t, \omega_s t + kz + n\theta)$; $\mathbf{f}$ is T_f-periodic in the second argument and 2π-periodic in the third argument. Figure 4.4(*a*) shows a gray-scale snapshot of the azimuthal vorticity at the outer cylinder, in a (θ, z) planar rendering of the cylinder surface for M1 at $\mathcal{A} = 79.6$ and $Re_i = 246.32$. Note that

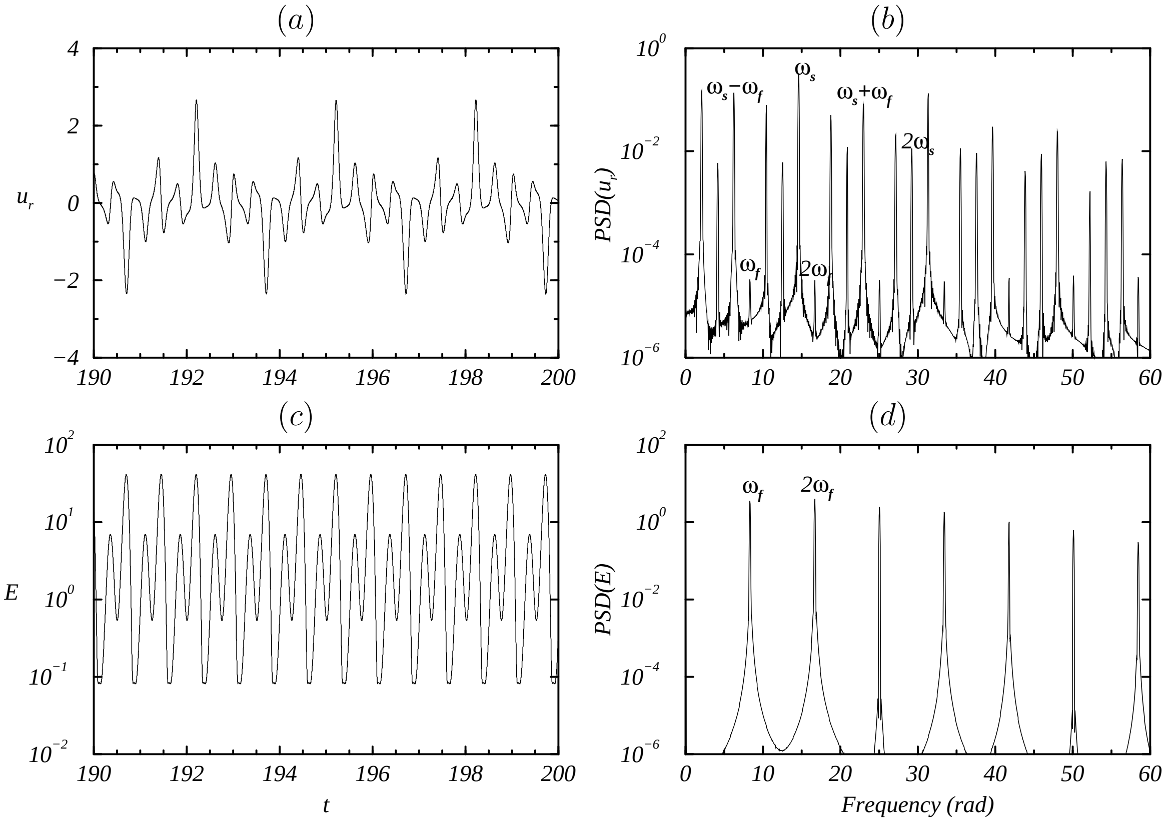

Figure 4.5: Time series of the radial velocity u_r at $(r, \theta, z) = ((r_i + r_o)/2, 0, 0)$ and the kinetic energy $E(\mathbf{u}, t)$, together with the corresponding power spectra, for the spiral waves (M1) shown in figure 4.4.

the azimuthal vorticity is constant over straight lines of angle β. Figure 4.4(*b*) shows a gray-scale snapshot of the kinetic energy of the Fourier modes $\mathrm{E}_{ln}(t)$. The leading mode is $(l, n) = (12, 1)$, i.e. with axial wavenumber $k = 12k_0 = 2.35$, which renders a spiral angle of $\beta \sim -23°$.

The translational and rotational symmetries of the basic flow are broken, but M1 retains a helical symmetry $H_\alpha = R_\alpha T_{-n\alpha/k}$, which consists of an arbitrary rotation R_α composed with an axial translation $T_{-n\alpha/k}$, leaving the phase $kz + n\theta$ invariant; the bifurcated solution is a spiral wave that is modulated by the harmonic forcing. However, due to the helical symmetry, strobing the solution at the forcing frequency renders the second argument in $\mathbf{f}$ constant and the strobed spiral pattern then precesses in the azimuthal direction with precession frequency $-\omega_s/n$. This azimuthal rotation can also be interpreted as an axial translation (barber-pole effect), with axial velocity $-\omega_s/k$. Therefore, M1 is a *relative periodic orbit*, in exactly the same way as rotating and traveling waves are *relative equilibria* (Rand, 1982; Wulff, Lamb & Melbourne, 2001).

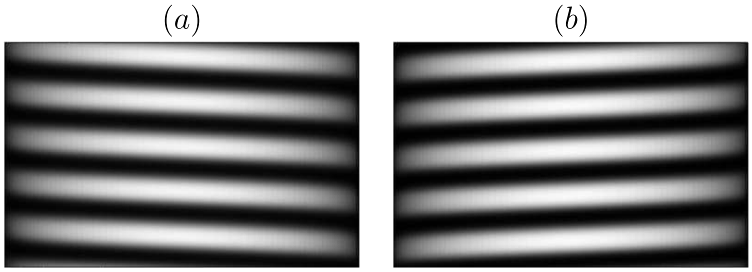

Figure 4.6: Perspective view (parallel projection of the cylinder). The gray-scale snapshot shows the intensity of azimuthal vorticity of the perturbation $\mathbf{u}$ at $r = r_o$. The flows are: (*a*) a left-handed upward propagating M1 and (*b*) a right-handed downward propagating M1, both at $\mathcal{A} = 79.6$ and $Re_i = 246.32$.

For the M1 case shown in figure 4.4, its radial velocity time series at the point $(r, \theta, z) = ((r_i + r_o)/2, 0, 0)$ along with the time series of its kinetic energy and the corresponding power spectra are shown in figure 4.5. The velocity time series and corresponding spectra indicate that M1 is quasi-periodic. However, as M1 is a relative periodic orbit, its kinetic energy has the form $g(r, t, \omega_s t + kz + n\theta)$ and is not modified by the presence of the spiral frequency ω_s. Integrating g over the whole domain, the $\omega_s t$ term is just a phase shift of the third argument; integrating over a complete period, the shift does not modify the result and the dependence on $\omega_s t$ disappears, leaving only the T_f-periodic time dependence of the second argument (the periodic forcing), as shown in figures 4.5(*c*) and (*d*).

The Neimark–Sacker bifurcation also breaks the spatio-temporal symmetry S, resulting in two different M1, corresponding to left-handed ($n = 1$) and right-handed ($n = -1$) spirals related by the action of S. As in chapter 3, the right-handed spirals propagate in the negative axial direction whereas the left-handed spirals propagate in the positive axial direction. Figure 4.6 shows a gray-scale snapshot of the azimuthal vorticity at the outer cylinder (as would be seen by an observer situated opposite the apparatus; note that due to the parallel projection used in this rendering, distances are not preserved and the angle of the spirals appears distorted towards the sides of the image) of (*a*) left-handed and (*b*) right-handed M1 at $\mathcal{A} = 79.6$ and $Re_i = 246.32$ (onset of instability is at $Re_{i,c} = 245.42$). Since the imposed periodic Stokes flow reverses its direction after half a forcing period, these solutions spend half the time traveling with and the other half traveling against the imposed flow. This behavior is manifested in the kinetic energy time series of figure 4.5(*c*), which shows two peaks of different intensity at t and $t + T_f/2$ corresponding to propagation with (higher peak) and against (lower peak) the imposed Stokes flow, indicating that the S symmetry is broken by the bifur-

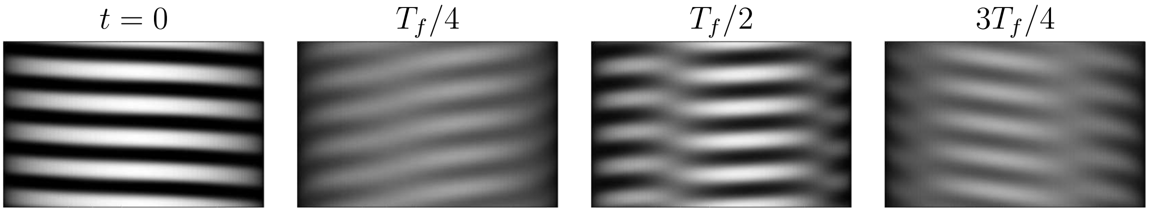

Figure 4.7: Snapshots of a perspective view (parallel projection of the cylinder). The gray-scale map shows the intensity of azimuthal vorticity of the perturbation $\mathbf{u}$ at $r = r_o$, where black (white) corresponds to positive (negative) values. The flow corresponds to M2 at $\mathcal{A} = 79.6$ and $Re_i = 247$ at 4 phases over one forcing period.

cation to M1. Note that for the S-symmetric basic flow the two peaks are identical (see figure 4.2). Therefore, the symmetry group of M1 is purely spatial, and its elements are the aforementioned helical motions H_α, generating a group isomorphic to $SO(2)$.

4.2.2 Secondary bifurcations

The M1 spiral waves that bifurcate from the basic flow are only stable in a very small region of parameter space, becoming unstable to a wavy spiral mode, M2. In particular, this secondary bifurcation occurs precisely at $\epsilon = (Re_i - Re_{i,c})/Re_{i,c} = 0.0039$ which is an order of magnitude smaller than the experimental uncertainty in Re_i. Therefore, the M1 spiral waves born at onset are not observable in the experiments of Sinha *et al.* (2006). The M2 state is characterized by the axial and azimuthal wavenumbers (k, n) of the underlying spiral wave (M1), and the wavy azimuthal wavenumber n_w, which is typically $3 \leq |n_w| \leq 5$ depending on the parameter values and the initial conditions. In contrast to the constant spiral angle β characteristic of M1, the M2 wavy spirals have a time-dependent inclination, as illustrated in the flow snapshots in figure 4.7.

The bifurcation leading to M2 is not synchronous with the imposed Stokes flow, so that the wavy spirals have a new independent frequency ω_w which corresponds to a secondary Hopf bifurcation from the quasi-periodic M1 to the three-torus state M2. Nevertheless, as the spiral wave M1 is a relative periodic orbit with symmetry group $SO(2)$, the bifurcation to M2 is effectively a Neimark-Sacker bifurcation with $SO(2)$ symmetry (Wulff *et al.*, 2001). The breaking of this symmetry results in a wavy flow with a discrete helical symmetry, as evident in figure 4.8(a). Instead of the straight lines of M1 in figure 4.4(a), the lines are modulated by the wavy azimuthal wave number $n_w = 5$. This can also be seen in the kinetic energies of the Fourier modes shown in the

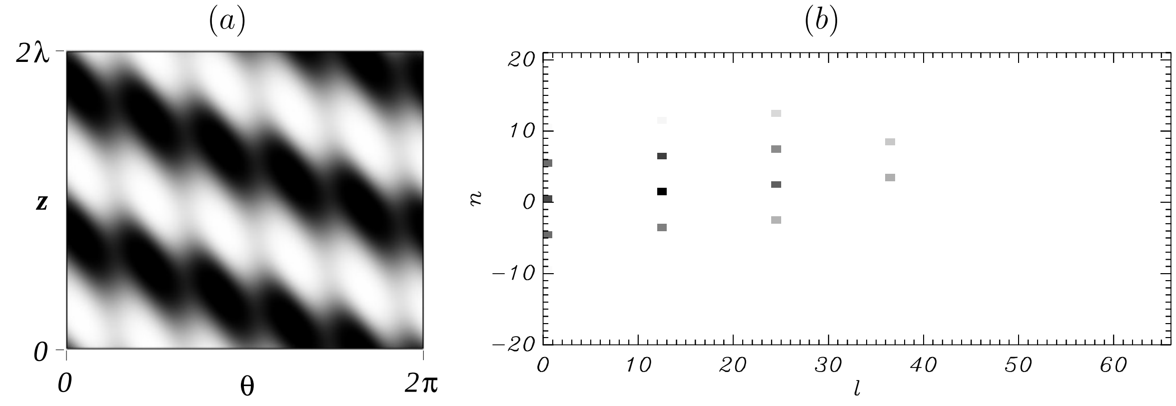

Figure 4.8: As figure 4.4 for M2 at $\mathcal{A} = 79.6$ and $Re_i = 247$.

gray-scale snapshot in figure 4.8(b). M2 features an axial wavenumber of $k = 12k_0 = 2.35$ and an azimuthal wavenumber of $n = \pm 1$. Moreover, an additional mode $(0, n_w) = (0, 5)$ appears, along with all the linear combinations between (k, n) and $(0, n_w)$. Therefore, the (θ, z)-dependence of M2 is of the form $\mathbf{f}(r, t, \omega_s t + kz + n\theta, \omega_w t + n_w\theta)$, where ω_w is the precession frequency associated to the wavy motion along the spiral pattern. The symmetry group of M2 is the discrete subgroup of $SO(2)$ generated by the helical symmetry $H_{\lambda/n_w} = R_{2\pi/n_w} T_{\lambda/n_w}$ and their integer multiples, leaving both phases in $\mathbf{f}$ invariant; $\lambda = 2\pi/k$ is the axial wavelength of the spiral pattern. Due to the periodicity of the boundary conditions, this group is isomorphic to $\mathbb{Z}_{ln_w}$.

Figure 4.9 shows the time series of the radial velocity and kinetic energy, as well as the corresponding power spectra, of M2 at the same parameter values as in figures 4.7 and 4.8. In contrast to M1 in figure 4.9, an additional high frequency modulation ω_w is evident in the radial velocity. Since ω_w is only associated with the precession speed of the wavy mode, it is not present in the kinetic energy time series, which has the form $g(r, t, \omega_s t + kz + n\theta, \omega_w t + n_w\theta)$. The base state has two periodic directions θ and z, and the two Hopf bifurcations correspond to time dependent shifts in these directions. Integrating with respect to θ and z, the two frequencies ω_s and ω_w disappear, and the kinetic energy is simply T_f-periodic. In fact, in an appropriate rotating and axially translating reference frame, M2 is purely periodic and synchronous with the forcing. Although in the laboratory M2 has three independent frequencies and therefore lives on a three-torus, the two frequencies ω_s and ω_w are of a kinematic nature, so that the M2 wavy spirals are also relative periodic orbits.

M2 becomes unstable at a third bifurcation at $\epsilon = (Re_i - Re_{i,c})/Re_{i,c} = 0.011$, evolving to a secondary wavy spiral state, termed M3. The visual differences between

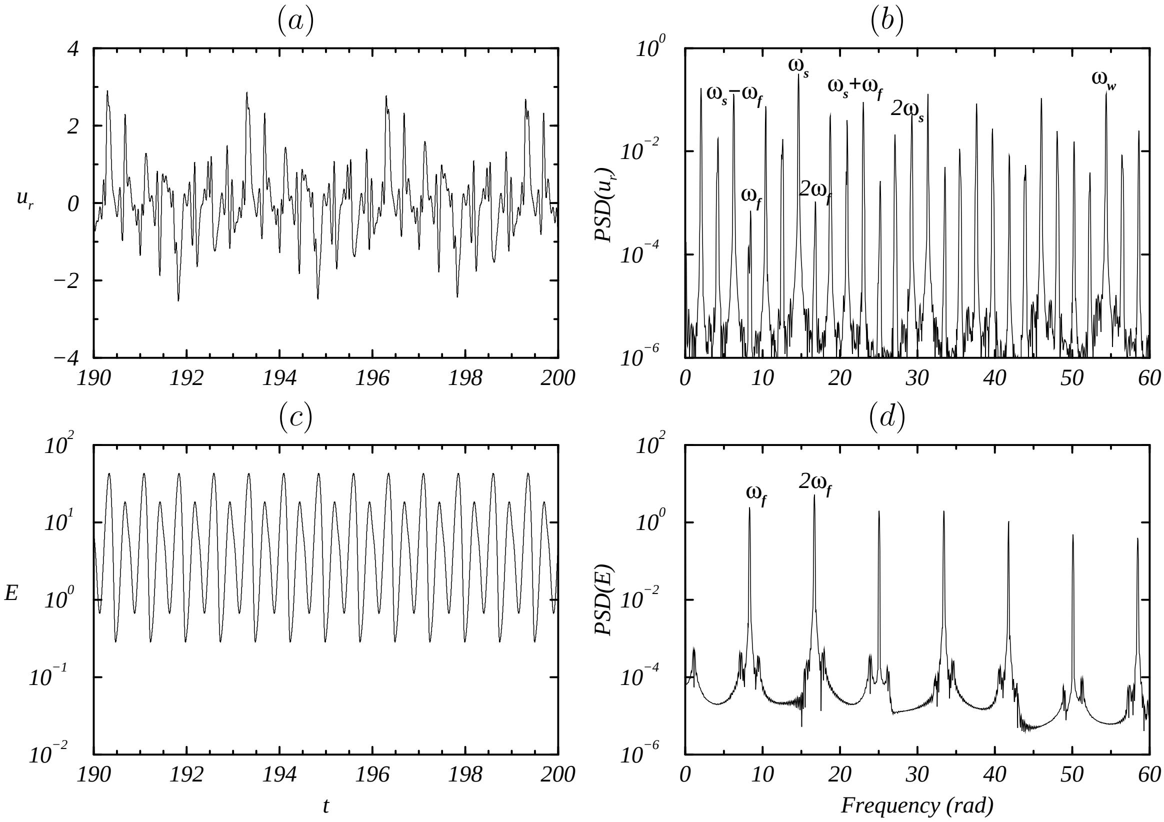

Figure 4.9: Time series of the radial velocity u_r at $(r, \theta, z) = ((r_i + r_o)/2, 0, 0)$, and the kinetic energy E, together with the corresponding power spectra, for the M2 wavy spirals shown in figures 4.7 and 4.8.

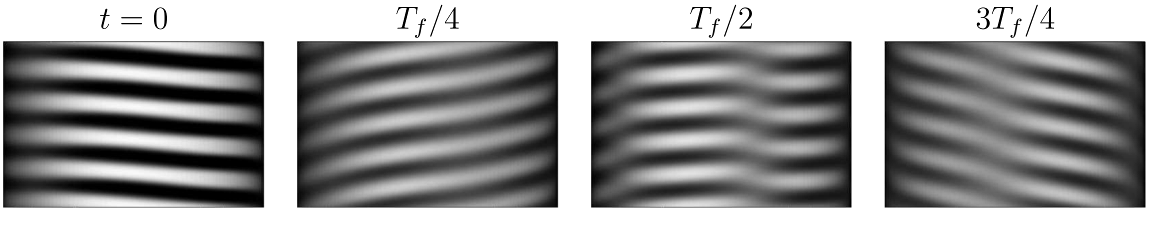

Figure 4.10: As figure 4.7. The flow corresponds to M3 at $\mathcal{A} = 79.6$ and $Re_i = 249$.

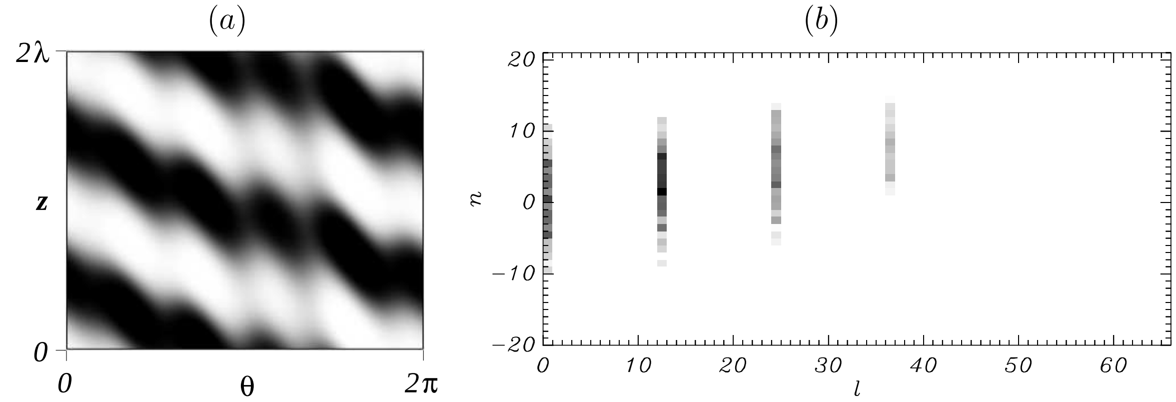

Figure 4.11: As figure 4.4 for M3 at $\mathcal{A} = 79.6$ and $Re_i = 249$.

the wavy spirals M2 before and M3 after this bifurcation are difficult to discern in the laboratory frame (snapshots of M3 are shown in figure 4.10, and should be compared with the corresponding snapshots of M2 in figure 4.7. However, the (θ, z)-planar rendering of the cylinder surface in figure 4.11(a) reveals that the azimuthal periodicity of M2 has been lost, and M3 has defects in the azimuthal wavenumber. In particular, the kinetic energy of the Fourier modes shown in the gray-scale map of figure 4.11(b) elucidates that the spectrum in azimuthal wavenumbers is now full due to competition between different wavy modes. Therefore, the helical motion (H_{λ/n_w} generating $\mathbb{Z}_{ln_w}$) is no longer a symmetry of the pattern. Nevertheless, M3 still preserves the axial periodicity given by the axial wavenumber $k = 12k_0 = 2.35$, so that the subgroup of $\mathbb{Z}_{ln_w}$ generated by T_λ remains. This symmetry group contains only axial translations of a multiple of the axial wavelength of the pattern and it is isomorphic to $\mathbb{Z}_l$.

The time series and corresponding power spectra of the radial velocity and kinetic energy just beyond this third bifurcation at $\mathcal{A} = 79.6$ and $Re_i = 248.5$ are shown in figure 4.12. The characteristics of the radial velocity are very similar to those before the bifurcation (compare with figure 4.9), although the irregularities in azimuthal wavenumber result in a higher degree of irregularity in the signal. Moreover, the kinetic energy is no longer T_f-periodic. It is now quasi-periodic, modulated by the spiral frequency ω_s.

A very small further increase in Re_i results in the loss of the axial periodicity present in M3 (i.e. the remaining translational symmetry $\mathbb{Z}_l$ is broken). As a result of competition between different axial modes, a non-constant axial wavelength is evident in figure 4.13(a), showing a gray-scale snapshot of the azimuthal vorticity at the outer cylinder in a (z, θ) planar rendering of the cylinder surface over the whole axial domain. At this bifurcation, the defective wavy spiral states, termed M4, emerge. These

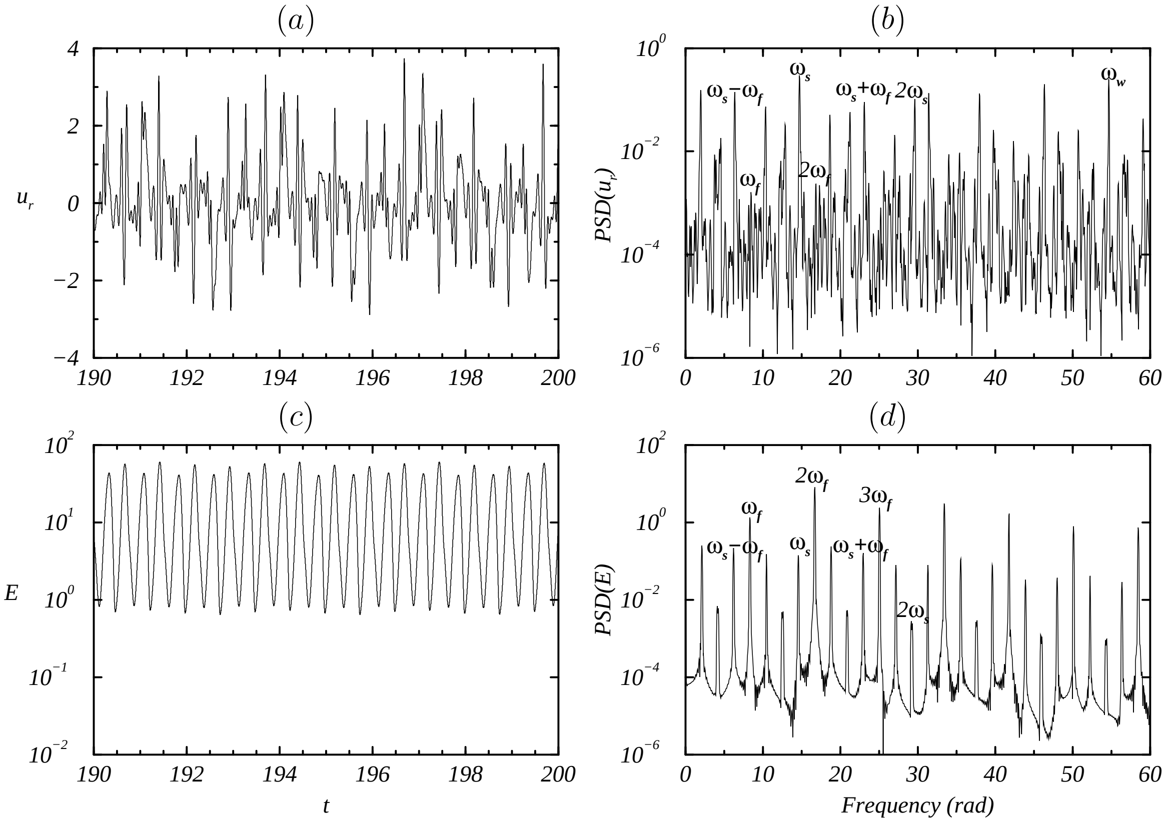

Figure 4.12: Time series of the radial velocity u_r at $(r, \theta, z) = ((r_i + r_o)/2, 0, 0)$, and the kinetic energy E, together with the corresponding power spectra, for M3 at $\mathcal{A} = 79.6$ and $Re_i = 248.5$.

are characterized by a broadband in k. Figure 4.13(b) shows a snapshot of the kinetic energy of the Fourier modes for M4. The spectrum is full in both axial and azimuthal wavenumbers, illustrating the spatial complexity of this non-symmetric flow. The increased temporal complexity of M4 is clear in the radial velocity and kinetic energy time series and corresponding power spectra shown in figure 4.14. The defects in the axial and azimuthal wavenumbers lead to broadbands in both the spatial and temporal spectra.

We note that in order to detect this bifurcation, occurring only 1.8% above the first onset of instability, spectral computations considering a small fundamental axial wavenumber k_0, as in the present work, are required. To the authors knowledge, this is the first time that such an approach is used in the Taylor–Couette problem. In previous works, the fundamental axial wavenumber was set to $k_0 = k_c$, so that defects in the axial wavenumber were not observable due to the imposed periodicity. The flow snapshots of figure 4.15 have been computed at $\mathcal{A} = 79$ and $Re_i = 250$, the same point in parameter

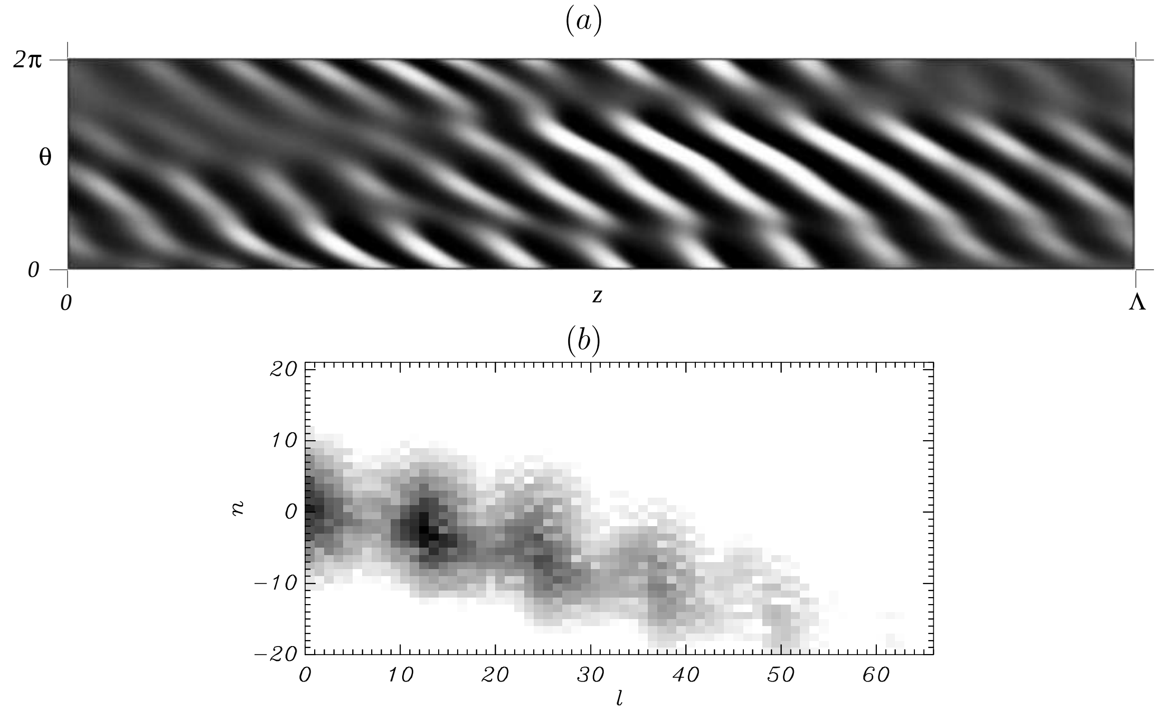

Figure 4.13: (a) Planar (z, θ) rendering of a gray-scale map of the azimuthal vorticity of the perturbation $\mathbf{u}$ at the outer cylinder $r = r_o$. The flow is M4 at $\mathcal{A} = 79$ and $Re_i = 250$. In (b) the kinetic energy of the Fourier modes of this state is shown in a logarithmic gray-scale map.

space as in figure 8 of Sinha *et al.* (2006). Although these parameter values correspond to the lowest post-critical value of their published data, Re_i is already 2.4% above the first onset of instability. As the bifurcation from M3 to the non-symmetric M4 occurs before (1.8% above $Re_{i,c}$), we can conclude that M4 corresponds to the wavy spiral states that are observed in the experiments just following onset. As noted in Sinha *et al.* (2006), the pattern loses spatial regularity very fast, becoming chaotic for higher Re_i. At this point, the spectral resolution demanded by these states renders our computations impractical, and so we do not pursue them further.

Figure 4.16 is a schematic of the various solutions obtained, and the bifurcations between them. The starting point is the base state, which is invariant under the full symmetry group of the problem, $\mathcal{G} = SO(2) \times O(2)^{ST}$, leaving the governing equations invariant. Below each stable solution found is the symmetry subgroup leaving the solution invariant, its generators, and the temporal character of the corresponding kinetic energy. The arrows correspond to the different bifurcations we have found in the present study, and each arrow is labeled with the type of bifurcation involved. This sequence of symmetry-breaking bifurcations occurs over about a 2% variation in Re_i (between

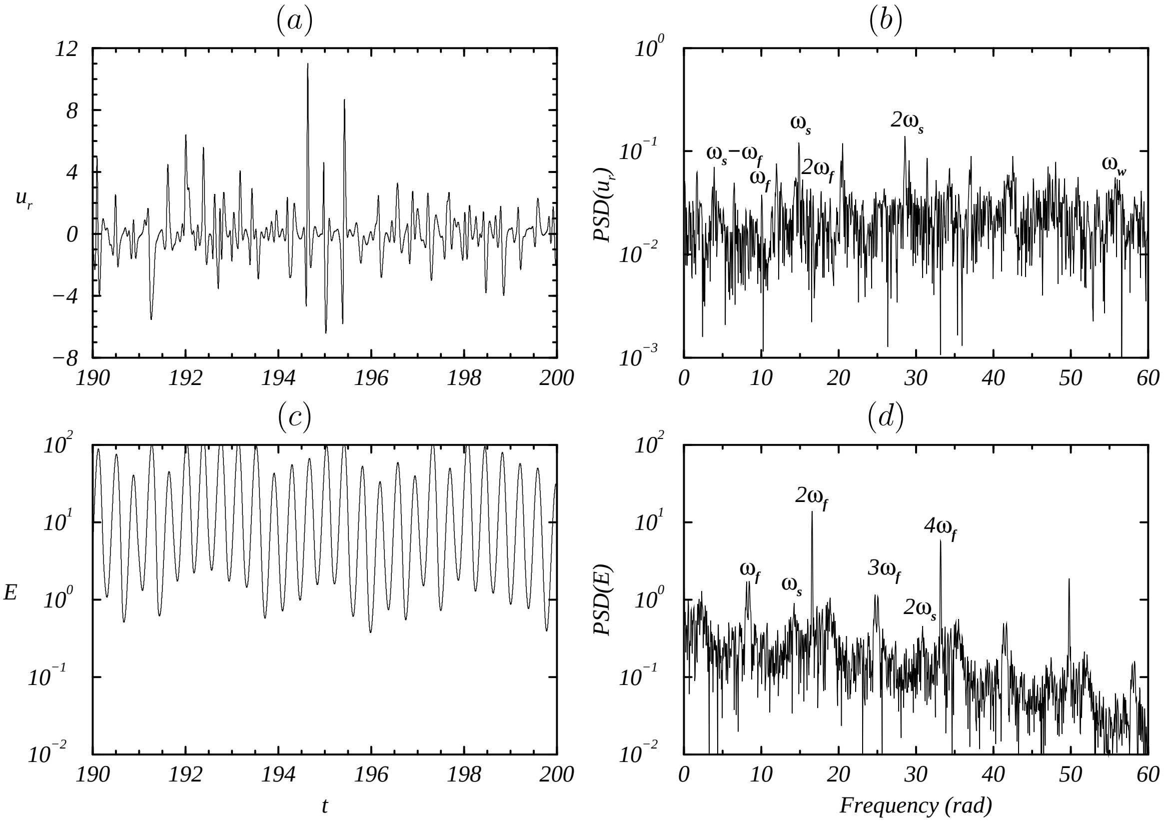

Figure 4.14: Time series of the radial velocity u_r at $(r, \theta, z) = ((r_i + r_o)/2, 0, 0)$, and the kinetic energy E, together with the corresponding power spectra, for M4 in figure 4.13.

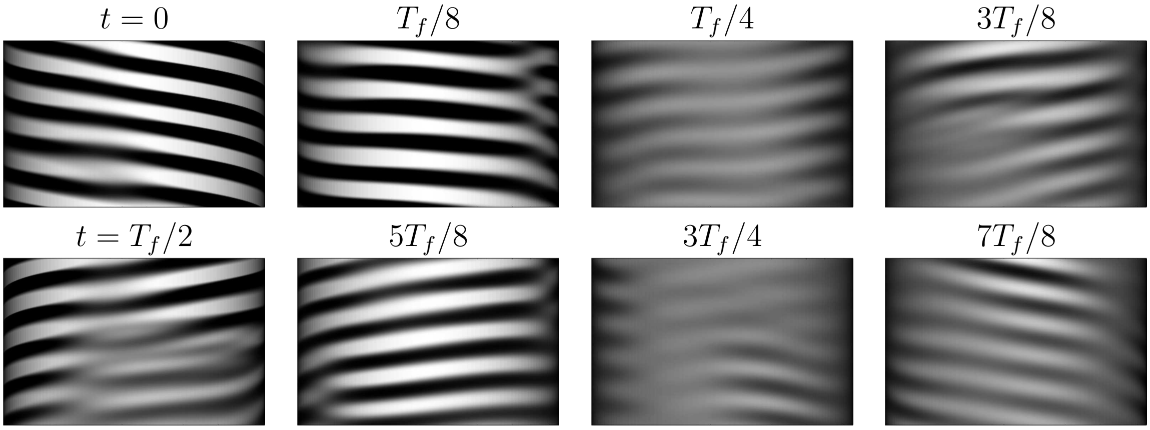

Figure 4.15: Same as figure 4.7. The flow corresponds to M4 at $\mathcal{A} = 79$ and $Re_i = 250$ shown at 8 phases over one forcing period.

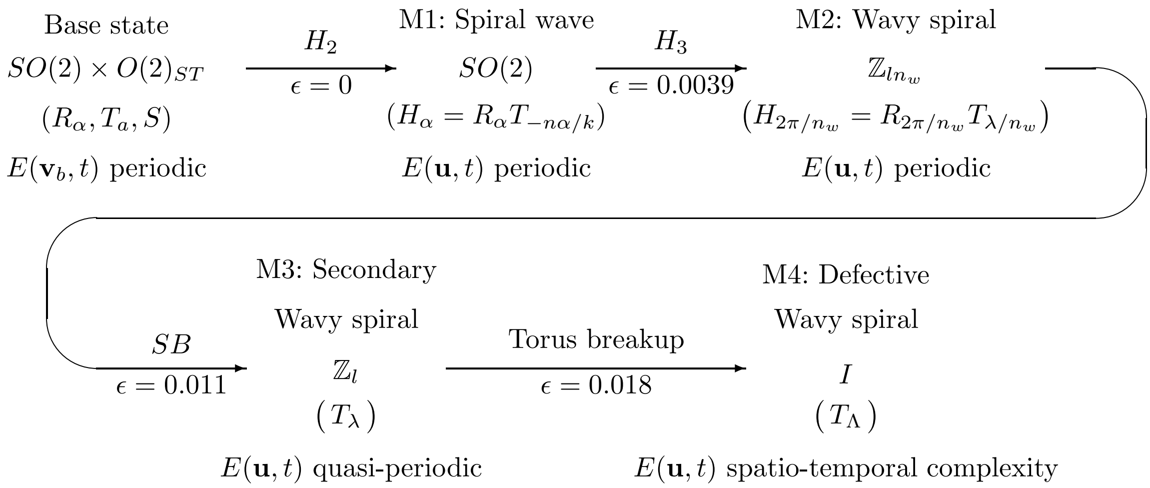

Figure 4.16: Diagram showing the successive bifurcations from the base state to M4 defective wavy spirals. For each solution the symmetry group, its generators and the form of $E(t)$ is indicated. H_n is a Hopf bifurcation to an n-dimensional torus (a relative periodic orbit), and SB is a symmetry breaking bifurcation of a three torus; the $\epsilon = (Re_i - Re_{i,c})/Re_{i,c}$ at which each of these bifurcations take place are also indicated ($Re_{i,c} = 245.42$).

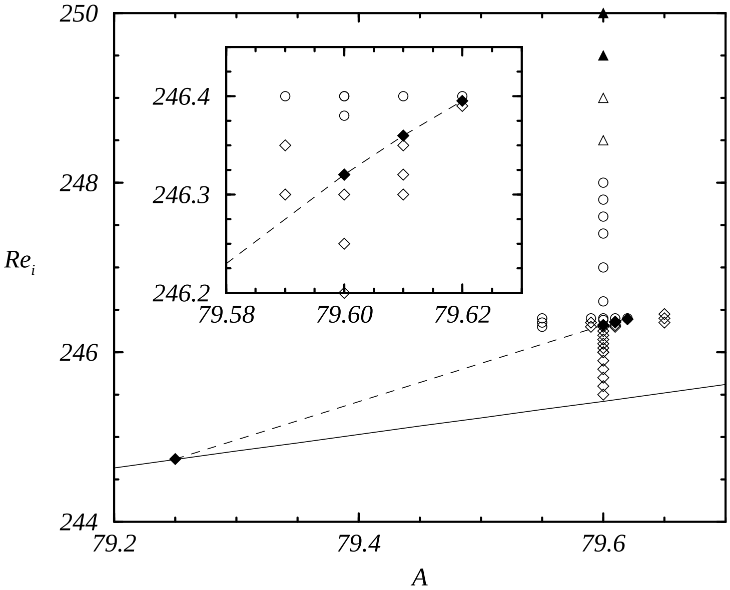

Figure 4.17: Loci of computed solutions for $\eta = 0.905$ and $\omega_f = \mathcal{A}/9.525$, as in Sinha *et al.* (2006). Above the solid line $Re_i = Re_{i,c}(\mathcal{A})$ the basic flow is unstable and evolves to a M1 spiral wave (◇) and to M2 wavy spirals (○) and M3 secondary wavy spirals (△) for higher values of Re_i. The ▲ indicate M4 defective wavy spirals. The dashed line is the resonance 7/4 curve originating at $\mathcal{A}/9.525 = 79.25$, $Re_i = 244.74$, and ◆ are M1 on the resonance line.

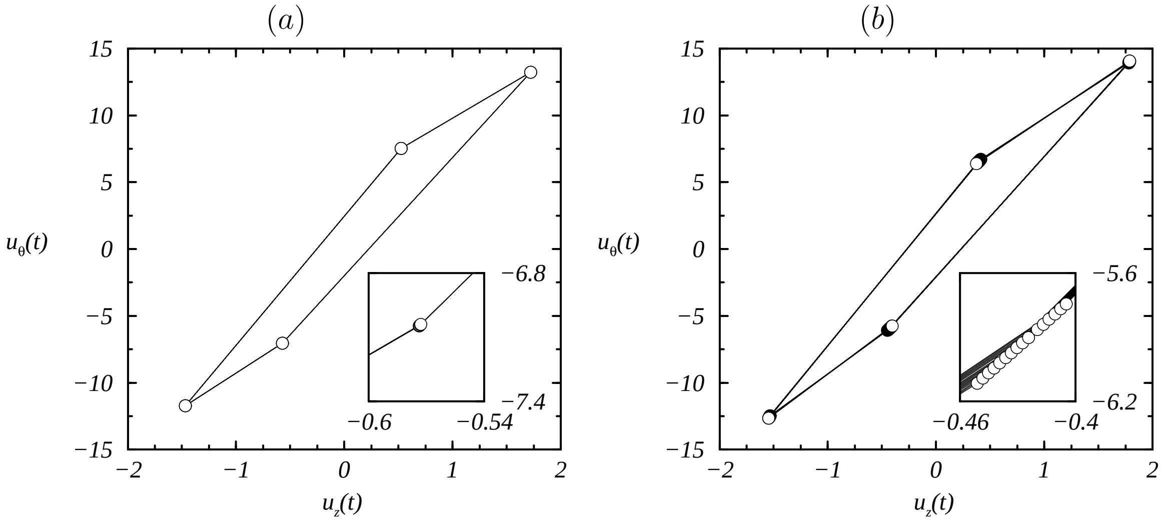

Figure 4.18: Poincaré maps for two M1 solutions, computed with the axial and azimuthal components of the perturbation at $(r, \theta, z) = ((r_i + r_o)/2, 0, 0)$ over several forcing cycles. In (a) the solution is very close to the 7/4 resonance at $\mathcal{A} = 79.6$ and $Re_i = 246.32$, whereas in (b) at $\mathcal{A} = 79.6$ and $Re_i = 246.35$, the flow is quasi-periodic, as is indicated by the slight shifts in subsequent iterates of the map in the close-up (both close-ups are at the same scale).

about $Re_i = 245$ and 250), which is about 2/3 of the experimental uncertainty in Re_i. Figure 4.17 shows the loci of computed solutions, where the subsequent bifurcations from the basic flow leading to the defective wavy spirals observed in the experiments are detailed in the parameter space.

4.3 Periodic flow and partial frequency-locking

In the previous section we described the transition scenario that leads from the simple time-periodic oscillating flow to complex dynamics following several symmetry-breaking bifurcations. When the oscillating basic flow (a periodic orbit) is destabilized via a Neimark–Sacker bifurcation, the flow becomes quasi-periodic, except for the cases where the bifurcating spiral frequency ω_s is resonant with the forcing frequency ω_f, i.e. the rotation number is rational $\omega_s/\omega_f \in \mathbb{Q}$, and then the flow remains periodic. In generic systems, nonlinear behavior in the neighborhood of such resonances typically manifests frequency-locking, i.e. there are regions of parameter space where the solution trajectory corresponds to a closed orbit on a 2-torus. These regions of frequency-locking typically are shaped like a horn whose tip is a cusp point on the bifurcation curve at which the rotation number is rational (Arnold *et al.*, 1999). However, the normal form analysis presented in Appendix C shows that due to the symmetries of the problem, the dynamics of the bifurcated M1 spiral waves are the same regardless of whether ω_s/ω_f is rational or irrational. There is no distinction between strong resonances, weak resonances ($\omega_s/\omega_f = \ell/m$, with $m > 4$), or no resonances ($\omega_s/\omega_f \notin \mathbb{Q}$). Therefore, the resonance horns collapse to one-dimensional resonance curves. This is a consequence of the rotational and translational symmetries of the system. Moreover, we show in §C.4 of Appendix C that due to the helical symmetry of M1, frequency-locking is also absent following the secondary bifurcation to M2.

In order to detect resonances, we strobe the phase trajectory once every forcing period to produce accurate global Poincaré maps. If the points in the map lie in a set of q clusters then the flow is periodic, whereas a densely filled orbit indicates that the flow is quasi-periodic. Figure 4.18(a) shows the Poincaré map for a M1 spiral wave at $\mathcal{A} = 79.6$ and $Re_i = 246.32$ using the phase trajectory given by the axial and azimuthal components of the perturbation $(u_z(t), u_\theta(t))$ recorded at $(r, \theta, z) = ((r_i + r_o)/2, 0, 0)$. Four clusters can be clearly observed. Since $\omega_f = 79.6/9.525 = 8.357$ and the computed value of the spiral frequency at criticality is $\omega_s = 14.61$, then the spiral wave is very close to the $\omega_s/\omega_f = 7/4$ resonance. The presence of a high peak at $\omega = 14.62$ in the power spectra of figure 4.5(b) together with the 4 distinct clusters of iterations in the Poincaré map (the close-up of one cluster shows that the iterates are slightly displaced) confirms this hypothesis. When Re_i is slightly increased by 0.03 to 246.35, the Poincaré map shown in figure 4.18(b) is very similar, with the small shifts in the iterates of the 4 clusters more pronounced. We have varied Re_i in very small increments about this region of parameter space and found no evidence of frequency-locking, in agreement with the equivariant theory in Appendix C. The flow is quasi-periodic and very close to the 7/4 resonance curve (the dashed line in figure 4.17).

In the previous section it was shown that due to uncertainty in the experiments (about 3% in Re_i), the states observed in the experiments are in the regime where the flow has no symmetries left. For these M4 states, there is no symmetry restriction on the development of resonance horns, but now the frequency-locking within these horns must be partial, i.e. only between two of the multiple frequencies that such a complex flow possesses. Figure 4.19 shows the Poincaré map for secondary wavy spirals M3 at $\mathcal{A} = 79.6$ and $Re_i = 248.5$ computed from both the azimuthal and axial components of the perturbation and the kinetic energy time series. Due to the multiple independent frequencies that this flow possesses (ω_f, ω_s, ω_w), and the irregularities due to defects in azimuthal wavenumber, there is no identifiable structure in the Poincaré map produced using the velocity. However, the Poincaré map based on the kinetic energy indicates

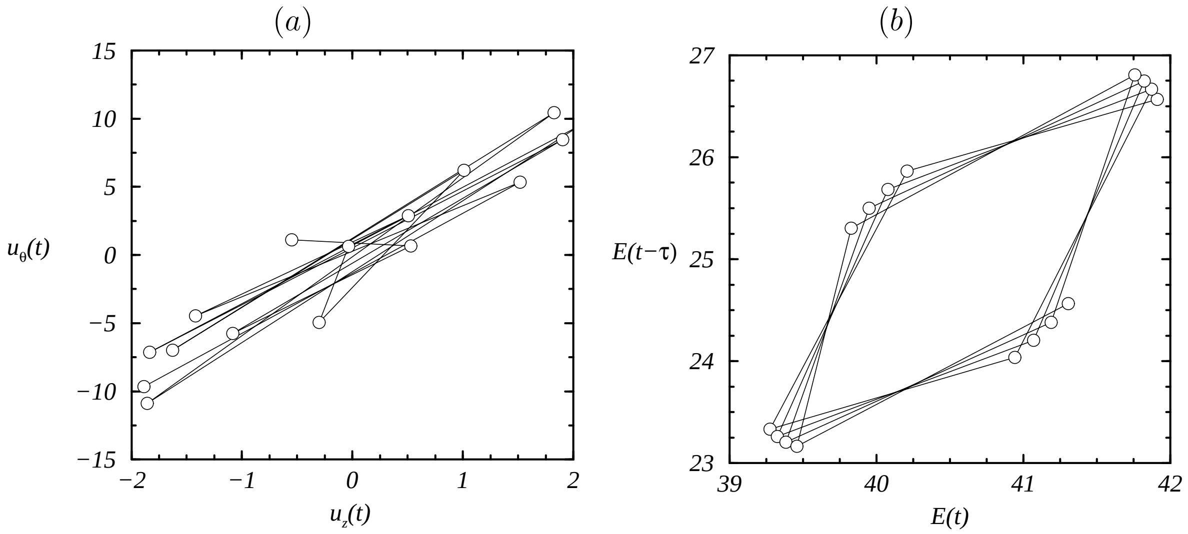

Figure 4.19: Poincaré maps for a secondary wavy spiral M3 at $\mathcal{A} = 79.6$ and $Re_i = 248.5$ over several forcing cycles. In (*a*) the axial and azimuthal components of the perturbation at $(r, \theta, z) = ((r_i + r_o)/2, 0, 0)$ are used for the phase trajectory, whereas in (*b*) the kinetic energy of the perturbation $E(t)$ and the delayed signal $E(t - \tau)$. The time delay is $\tau = 0.452$.

that the solution is close to the 7/4 partial-locking horn. In this case, the kinetic energy acts as a natural filter for some of the frequencies in the flow, in particular those due to the kinematic frequencies associated with the rotation and axial translation of the spiral pattern. In fact, figure 4.19(*b*) is similar to the frequency-locking plots reported in the experiments of Sinha *et al.* (2006). This sheds some light on the apparent discrepancy between the frequency-locking observations reported in these experiments and our theoretical analysis which shows that the symmetries of the basic flow and M1 inhibit frequency-locking. The sequence of symmetry-breaking bifurcations over a very small range in Re_i removes this restriction and the partial locking is then observable in our nonlinear computations as it is in the experiments.

4.4 Discussion and Conclusions

Nonlinear dynamics of an axially forced Taylor–Couette system has been investigated numerically by solving the unsteady three-dimensional Navier–Stokes equations. In earlier studies, it was shown experimentally (Weisberg *et al.*, 1997) and numerically with Floquet analysis of the basic flow (Marques & Lopez, 1997) that a high degree of stabilization could be achieved for low frequencies and large amplitudes of the forcing. More recently, the nonlinear dynamics beyond onset of instability was experimentally investigated (Sinha *et al.*, 2006), focusing on regions of parameter space where transition is to a spiral mode following a Neimark–Sacker bifurcation.

Our nonlinear numerical explorations have been focused on the same parameter regime as in the experiments by Sinha *et al.* (2006). The flows they observed appeared to contain a high degree of noise, i.e. the signals contained a number of frequencies that could not be identified. Here, using precise spectral computations, we have shown that this apparent noise is due to a sequence of symmetry-breaking bifurcations occurring very close to the primary onset of instability introducing additional independent frequencies. For Re_i only 0.39% above critical, a secondary bifurcation renders the spiral mode into a wavy spiral mode and introduces a third independent frequency. For slightly higher Re_i, the wavy spirals develop defects in the azimuthal and axial wavenumbers, resulting in spatial and temporal broadband spectra; this is commonly referred to as the onset of soft turbulence. Overall, for Re just 2% above the instability threshold for the basic state, the flow is spatio-temporally very complex. The fine discretization in wavenumber used in the nonlinear computations, combined with careful consideration of the symmetries of the bifurcated flows, is essential to understand the sequence of symmetry-breaking bifurcations that leads from a simple symmetric flow to a very complex pattern.

The experiments reported bands of frequency-locking between the frequency of the forcing and the spiral frequency stemming from the Neimark–Sacker bifurcation. Our theoretical work in Appendix C shows that frequency-locking leading to periodic flow is not possible in the system under consideration. The rotational and translational $SO(2)$ symmetries of the oscillating basic flow annihilate the resonant terms in the normal form of the Neimark–Sacker bifurcation, rendering the dynamics independent of the ratio between frequencies and preventing the formation of resonance horns. However, once the continuous $SO(2)$ symmetries are broken, frequency-locking is permitted. Since there are more than two independent frequencies in this parameter regime, a one-parameter variation will generically only detect regions of partial frequency-locking between two of the frequencies. This partial frequency-locking is very likely the phenomena observed in the experiments, since in the regimes where locking was detected the flow is extremely complex featuring various frequencies and defects in the axial and azimuthal periodicity. Moreover, these additional frequencies account for the noisy Poincaré maps which were used experimentally to identify the regions of locking. This highlights the care that needs to be taken in distinguishing between extraneous noise and the effects of deterministic bifurcations in accounting for spatio-temporal complex dynamics.

CHAPTER 5
MODULATED TAYLOR–COUETTE FLOWS

Time-harmonic modulations of the inner cylinder rotation in Taylor–Couette flows have been and continue to be of much interest. The original motivation for studying the effects of modulations was the experimentally observed threshold shift to higher mean rotation for the onset of sustained Taylor vortices (Donnelly, 1964). Hall (1975), neglecting curvature effects by taking the small gap limit $\eta = r_i/r_o \to 1$, performed a perturbation analysis for small modulation amplitudes and frequencies, showing that in this limit the modulations slightly destabilize the basic state. His results were confirmed by the Floquet analysis (also in the narrow gap limit) of Riley & Laurence (1976), contradicting the experimental results of Donnelly (1964). In an attempt to shed light on the nature of this discrepancy, Carmi & Tustaniwskyj (1981) extended the Floquet analysis to finite values of the radius ratio, i.e. including curvature effects. However, their results showed a much larger degree of destabilization than the previous theoretical and computational studies of Hall (1975) and Riley & Laurence (1976), contradicting all of the previous experimental and theoretical work on the problem.

Barenghi & Jones (1989) performed nonlinear computations of the Navier–Stokes equations for finite gap and confirmed the results of Hall (1975) and Riley & Laurence (1976). They noted that the computations of Carmi & Tustaniwskyj (1981) were performed with too large a time-step, so that in the low-frequency limit they were unable to properly reproduce the exponential growth and decay of the perturbations during a modulation period. Following Hall (1983), who showed that in the low-frequency limit the most relevant perturbations are not periodic solutions of the equations of motion, Barenghi & Jones (1989) introduced a low level of noise in their computations and obtained qualitative agreement with Ahlers' experimental results which were published as an appendix to Barenghi & Jones (1989). They concluded that the discrepancies regarding stability limits were due to noise-induced difficulties in experimentally determining the onset of instability.

The Floquet analysis in the narrow gap limit of Riley & Laurence (1976) showed that for zero-mean modulations of the inner cylinder, two different time-periodic Taylor vortex flows compete. For low frequencies the flow is characterized by a reversal of the sign of the radial and axial velocities every half-period, whereas for higher frequencies the radial and axial velocities pulse twice during a cycle without changing sign. Nevertheless, none of the subsequent Floquet analyses for finite values of the radius ratio (Carmi & Tustaniwskyj, 1981; Barenghi & Jones, 1989) detected competition between the two different modes. This was attributed to a failure of the narrow gap limit in the modulated Taylor–Couette system (Carmi & Tustaniwskyj, 1981). More recently, Youd, Willis & Barenghi (2003) performed nonlinear computations for a medium gap ($\eta = 0.75$) and confirmed the existence of these modes, terming them reversing and non-reversing Taylor vortex flow, respectively. Consequently, it was not clear whether the linear stability results of Riley & Laurence (1976) extended to the case of finite radius ratio η or if one or both modes were due to nonlinear growth of finite-amplitude perturbations.

We have performed a Floquet analysis of the basic state and found that both reversing and non-reversing flows are due to linear instabilities of the basic state, confirming the results of Riley & Laurence (1976). In fact, the instabilities are pitchfork-of-revolution bifurcations in which the axial translation invariance is broken. For non-reversing flow this is the only symmetry which is broken, whereas the pitchfork-of-revolution bifurcation leading to reversing flow also breaks the half-period-flip spatio-temporal symmetry under which the basic state is invariant. Hydrodynamic systems with the same symmetries that bifurcate to two different competing periodic modes have also been found numerically and experimentally in periodically driven cavity flow (Marques, Lopez & Blackburn, 2004; Vogel, Hirsa & Lopez, 2003) and in the wake of a circular cylinder (Barkley & Henderson, 1996; Williamson, 1996). In those problems, the bifurcating states were named modes A and B, and we shall adopt this nomenclature as well in the present problem, rather than using the terms reversing and non-reversing. Here, we not only characterize the spatio-temporal properties of the bifurcated flows, but also investigate mode competition in a neighborhood of the codimension-two point where they bifurcate simultaneously using both nonlinear simulations and laboratory experiments.

5.1 Symmetries

We consider the TaylorCouette system with stationary outer cylinder and inner cylinder rotating at angular velocity which is modulated harmonically in time about a zero mean

$$Re_a \sin(\omega t), \tag{5.1}$$

where Re_a and ω are the non-dimensional amplitude and frequency of the modulations, respectively. Figure 5.1 is a schematic of the system. The geometry of the annulus is defined by the radius ratio $\eta = r_i/r_o$, which we fix at $\eta = 0.5$ in the computations to match that of the experimental apparatus. For the Floquet analysis, the cylinders are assumed to be infinite, whereas the nonlinear computations are performed in a long periodic annulus with axial period $\Lambda = 41.89$ times the annular gap. This corresponds to a

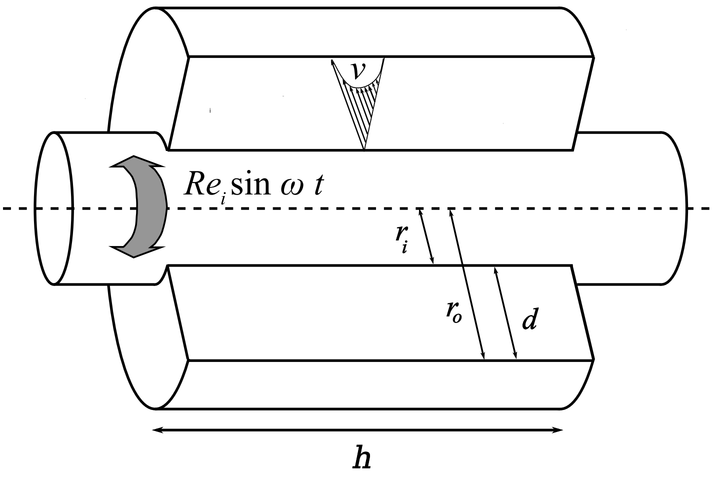

Figure 5.1: Schematic of modulated Taylor–Couette flow.

fundamental wavenumber $k_0 = 0.15$ in (2.17) as in the Eckhaus instability computations of §2.3. In the physical apparatus, whose details can be found in Belisle (2007), the aspect ratio of the annulus is $\Gamma = h/d = 115$.

The boundary conditions are

$$\mathbf{v}(r_i, \theta, z, t) = (0, Re_i(t), 0), \quad \mathbf{v}(r_o, \theta, z, t) = \mathbf{0}, \tag{5.2}$$

where $Re_i(t) = Re_a \sin(\omega t)$ is the instantaneous Reynolds number. The resulting modulated Couette flow (mC) is purely azimuthal and synchronous with the imposed harmonic oscillations

$$\mathbf{v}_{mC} = \Big(0, Re_a\, \Im(f(r)\, \mathrm{e}^{\mathrm{i}\omega t}), 0\Big), \tag{5.3}$$

where $f(r)$ is the solution of a second order ODE; f can be expressed in terms of modified Bessel functions, but here it has been computed using collocation at Gauss–Lobatto points, as in the previous chapter. The linear stability of mC (5.3) has been determined by Floquet analysis following Lopez & Marques (2002).

The governing equations and boundary conditions are invariant to K_z reflection $z \to -z$ and to translations T_a along the z-axis. In the azimuthal direction they are invariant to arbitrary rotations R_α. Together, these symmetries generate the group of spatial symmetries of the classical Taylor–Couette system $\mathcal{G}_0 = SO(2) \times O(2)$. Their actions on the velocity field are given in (2.5)–(2.7). The basic state (4.5) is invariant under $\mathcal{G}_0$. Moreover, when modulations about a zero mean are considered, there is an additional spatio-temporal symmetry S, which consists of a time evolution of a half modulation period followed by the reflection K_θ on the meridional plane $\theta = 0$ (acting as $\theta \to -\theta$), whose action on the velocity is:

$$S(\mathbf{v})(r,\theta,z,t) = K_\theta(\mathbf{v})(r,\theta,z,t+T/2) = (v_r,-v_\theta,v_z)(r,-\theta,z,t+T/2), \qquad (5.4)$$

where $T = 2\pi/\omega$. If S were purely spatial, i.e. the reflection K_θ, then S and R_α would generate the orthogonal group, $O(2) = SO(2) \rtimes Z_2$, where the elements of Z_2 would be K_θ and the identity. Since S is a space-time symmetry, S and R_α generate a space-time symmetry group isomorphic to $O(2)$, which we term $O(2)^{ST} = SO(2) \rtimes Z_2^{ST}$, where now the elements of Z_2 are S and the identity. Therefore, the complete symmetry group of the system modulated about a zero mean is $\mathcal{G} = O(2)^{ST} \times O(2)$ and the basic state (4.5) is invariant under $\mathcal{G}$. When the dynamics preserve the axisymmetry, as is the case over large regions in parameter space, the rotations R_α do not play any dynamic role (they act trivially on the solutions of the governing equations), and in the axisymmetric subspace the symmetry group of the problem reduces to $\mathcal{G} = Z_2^{ST} \times O(2)$.

Generally, the stability of T-periodic flows is determined by Floquet analysis considering their Poincaré map

$$x_0 \longmapsto \mathcal{P}(x_0) = \phi(t_0+T;x_0,t_0), \qquad (5.5)$$

where $\phi(t_0+t;x_0,t_0)$ is the solution of the governing equations at time t with initial conditions (x_0,t_0) in a neighborhood of the periodic orbit. However, for systems with Z_2 spatio-temporal symmetry, the Poincaré map is the square of the half-period-flip map

$$x_0 \longmapsto \mathcal{H}(x_0) = K_\theta\phi(t_0+T/2;x_0,t_0). \qquad (5.6)$$

In these cases, the eigenvalues of $\mathcal{P}$ are $\mu_\mathcal{P} = \mu_\mathcal{H}^2$, where $\mu_\mathcal{H}$ is the corresponding eigenvalue of $\mathcal{H}$. The action of S has important implications on the dynamics of the bifurcated solutions which cannot be detected by studying the stability of $\mathcal{P}$ alone. Marques *et al.* (2004) derived normal forms for codimension-one and two bifurcations in systems with $\mathcal{G} = Z_2^{ST} \times O(2)$, for both $\mathcal{H}$ and $\mathcal{P}$.

5.2 Types A (reversing) and B (non-reversing) modulated Taylor vortex flows

5.2.1 Floquet analysis of the modulated Couette flow

Codimension-one bifurcations are generically obtained when a single parameter is varied. For modulated Couette flow (mC), the possible codimension-one bifurcations correspond to Floquet multipliers of the Poincaré map $\mu_\mathcal{P} = 1$ or the complex conjugate

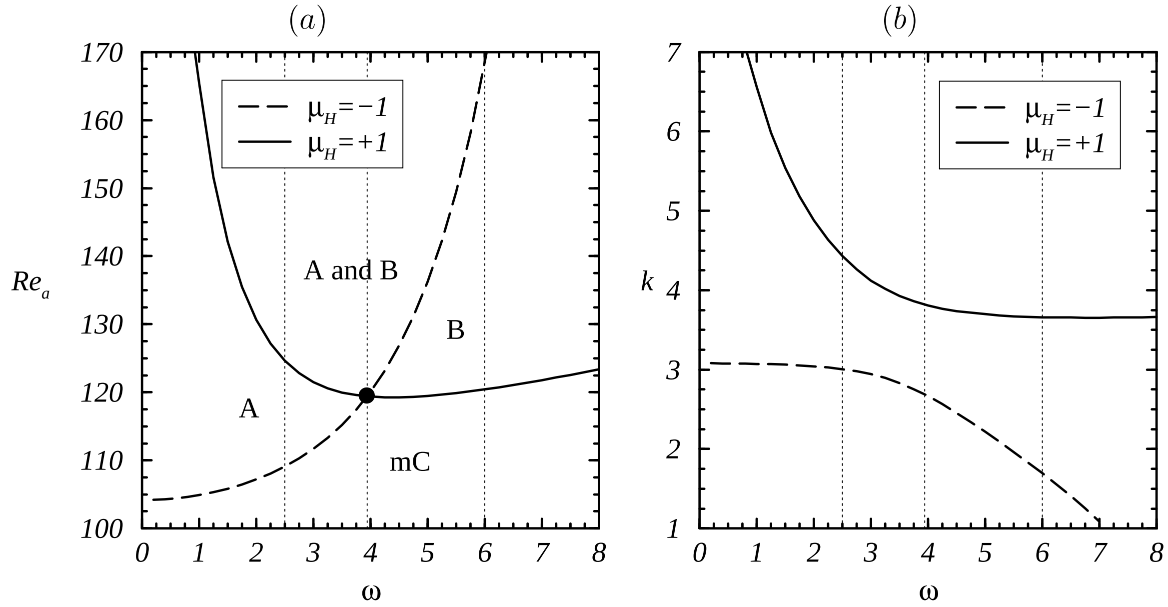

Figure 5.2: (a) Regime diagram obtained via Floquet analysis of the modulated Couette flow (5.3) using the half-period-flip map $\mathcal{H}$. The circle denotes the bicritical point $(\omega, Re_{a,c}) = (3.936, 119.4)$. ($b$) Corresponding axial wavenumber $k_c(\omega)$ at criticality. The vertical dotted lines are the frequencies ω at which the marginal stability curves are shown in figure 5.3.

pair $\mu_{\mathcal{P}} = \exp(\pm i\theta)$. The case of $\mu_{\mathcal{P}} = -1$ is the period-doubling bifurcation which is inhibited by the space-time Z_2 symmetry S (Swift & Wiesenfeld, 1984). Furthermore, the synchronous case $\mu_{\mathcal{P}} = 1$ actually comes in two flavors, one which breaks the symmetry S and another which preserves it. These two cases are readily distinguished by using the half-period-flip map $\mathcal{H}$ for the Floquet analysis, where $\mu_{\mathcal{P}} = \mu_{\mathcal{H}}^2$ and $\mu_{\mathcal{H}} = +1$ is the S-preserving synchronous bifurcation and $\mu_{\mathcal{H}} = -1$ is the S-breaking synchronous bifurcation. The quasi-periodic case $\mu_{\mathcal{P}} = \exp(\pm i\theta)$, while also being generic, has not been observed for modulated Taylor–Couette flow in the parameter regimes studied so far. However, when the outer cylinder is modulated, Lopez & Marques (2002) found some parameter regimes where the quasi-periodic case leads to modulated spiral flows.

Figure 5.2 shows the results of the Floquet analysis of the basic state mC, using the half-period-flip map $\mathcal{H}$. The bifurcation curves $Re_a = Re_{a,c}(\omega)$ are shown in part (a) of the figure. The solid curve is a pitchfork-of-revolution bifurcation corresponding to $\mu_{\mathcal{H}} = +1$, where mode B bifurcates from mC, and the dashed curve is also a pitchfork-of-revolution bifurcation corresponding to $\mu_{\mathcal{H}} = -1$, where mode A bifurcates. These bifurcations break the continuous translational symmetry T_a, which is replaced by a discrete translational symmetry $T_{2\pi/k_c}$, where $k_c(\omega)$ is the critical wavenumber at the

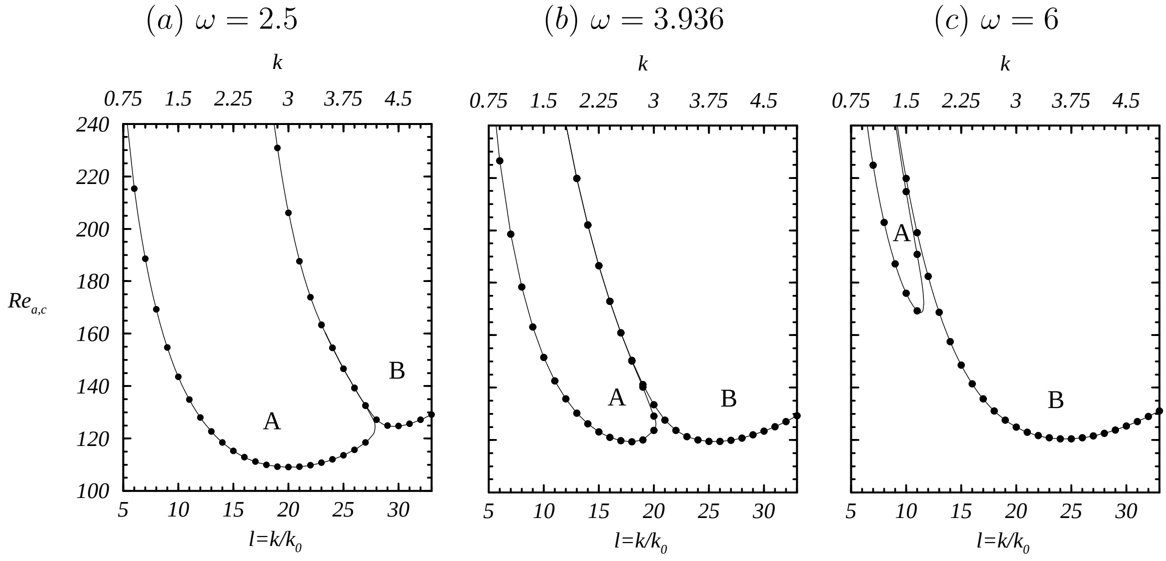

Figure 5.3: Neutral stability curves as computed with Floquet analysis for (a) $\omega = 2.5$, (b) $\omega = 3.936$ and (c) $\omega = 6$. The circles correspond to the discrete set of wavenumbers k considered in the nonlinear computations such that $k \in [0.75, 4.95]$.

bifurcation (see figure 5.2b). The two modes remain T-periodic but mode A breaks the S-symmetry and mode B preserves it.

The four regions in figure 5.2(a) are labeled with the states that exist in them (note that mC exists everywhere but is only stable in the region where it is labeled). Below both the A and B curves only the basic state mC exists and is stable. In the region above both the A and B curves, modes A and B coexist. At low modulation frequencies, mode A is the primary bifurcation (i.e. for a given ω, A bifurcates from mC first as Re_a is increased), and at large frequencies, mode B is primary. The point $(\omega, Re_a) = (3.936, 119.4)$ is a codimension-two point where the two bifurcations occur simultaneously. Figure 5.3 shows neutral stability curves for modulation frequencies $\omega = 2.5$, 3.936 and 6. At $\omega = 2.5$, the bifurcation to A is primary, occurring for a wide range of wavenumbers. At $\omega = 3.936$, both neutral stability curves have minima at $Re_{a,c} = 119.4$, giving rise to the codimension-two bifurcation point. At $\omega = 6$ the bifurcation to A is confined to a small range of wavenumbers and the bifurcation to B is primary. These linear stability results have the same features as the nonlinear computations of Youd *et al.* (2003) for $\eta = 0.75$. Note that the neutral stability curves for A and B do not cross, so that at given (ω, Re_a) the wavenumber of the flow suffices to determine which state is realized in the nonlinear computations and experiments. However, comparing figures 5.3(a) and 5.3(c), it is clear that by changing either Re_a or ω it is possible to obtain A and B with the same wavenumber.

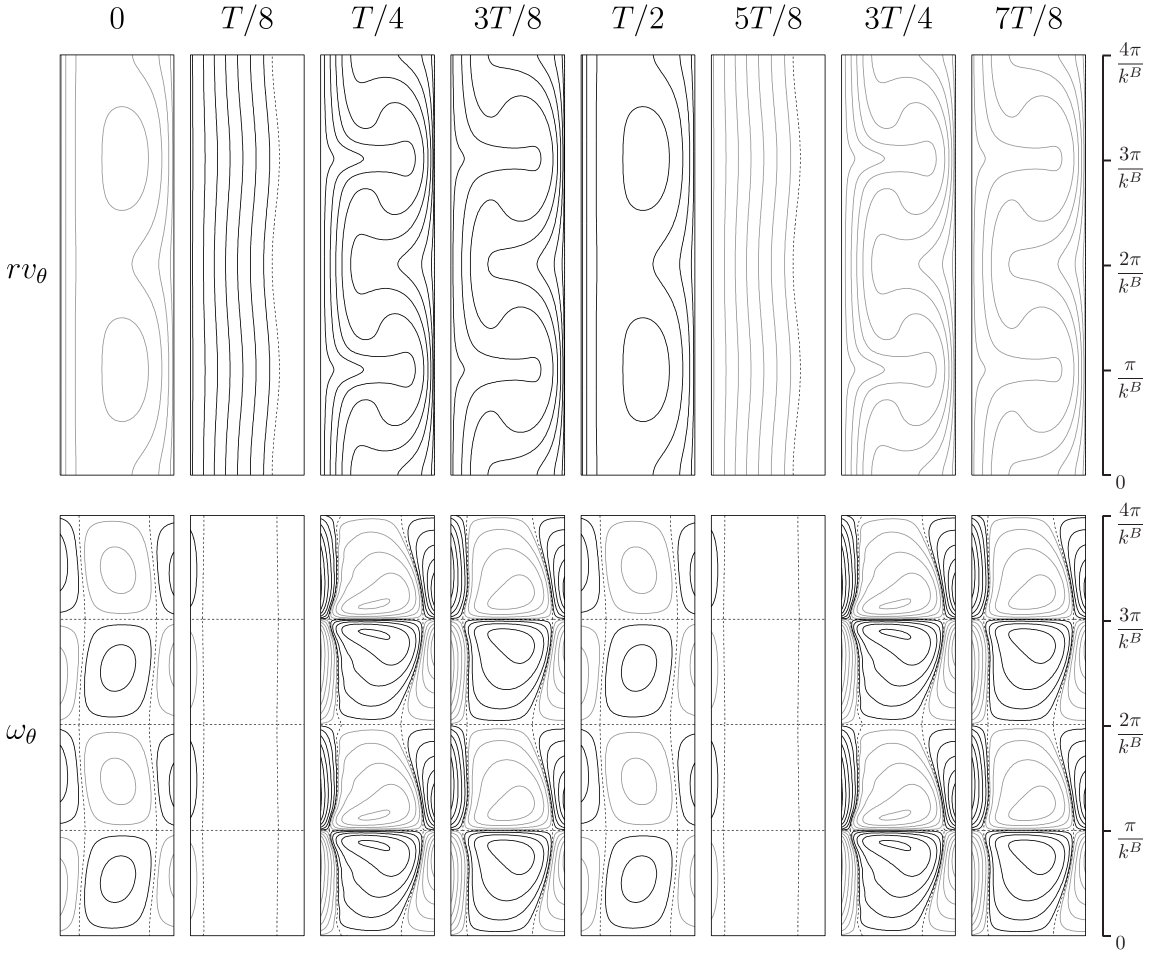

Figure 5.4: Type B (non-reversing) Taylor vortex flow at $\omega = 6.1$ and $Re_a = 240$ with wavenumber $k^B = 3.4$. Quadratically spaced contours of angular momentum (top row) and azimuthal vorticity (bottom row) are shown in a meridional cross-section over a period $T = 2\pi/\omega$. Black (gray) contours correspond to positive (negative) values, showing $r \in [1, 2]$ and $z \in [0, 4\pi/k^B]$. The snapshots have been taken after transients have vanished. In particular, a time shift of several periods $t \to t - NT$ has been applied.

5.2.2 Numerical characterization of the flows

The Taylor–Couette system with modulations about a zero mean is characterized by two distinct phases, depending on the instantaneous value of $Re_i(t) = Re_a \sin \omega t$. When $Re_i(t) < Re_{i,c}$ (the critical Reynolds number of steady Couette flow), the motion of the cylinder is subcritical and therefore all the perturbations decay. For $Re_i(t) > Re_{i,c}$ perturbations are amplified and vortices (Taylor cells) develop. Figure 5.4 shows contours of angular momentum rv_θ (top row) and azimuthal vorticity ω_θ (bottom row) over a modulation period for state B at $\omega = 6.1$ and $Re_a = 240$ with wavenumber $k^B = 3.4$. At $t = 0$, which corresponds to $Re_i(t) = 0$, weak pairs of Taylor cells remain from the previous

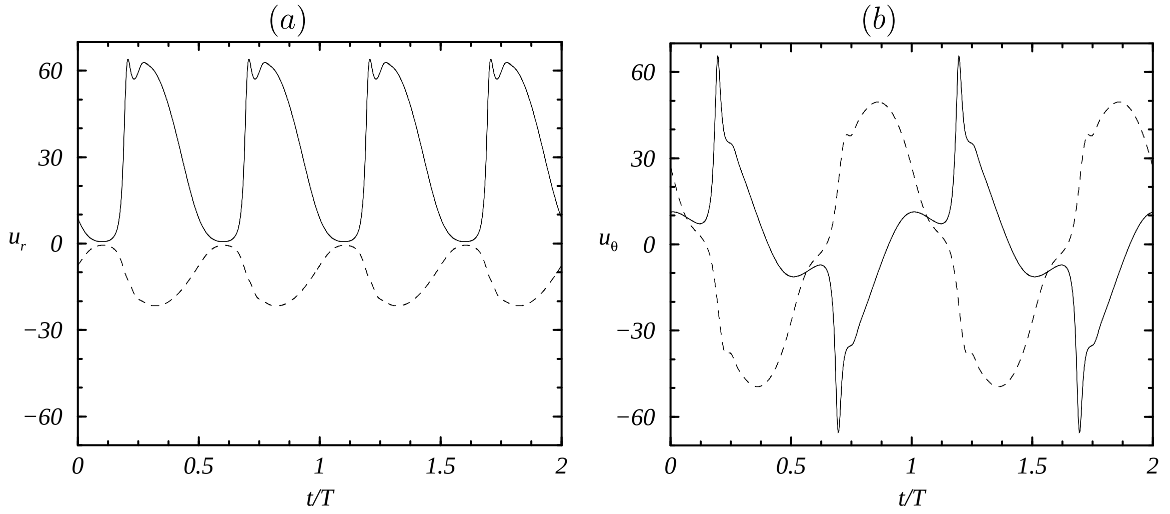

Figure 5.5: Evolutions over two periods of (*a*) the radial velocity and (*b*) the azimuthal velocity components of the perturbation field (2.18) recorded at $(r, \theta, z) = ((r_i + r_o)/2, 0, \pi/k^B)$ (solid lines) and $(r, \theta, z) = ((r_i + r_o)/2, 0, 0)$ (dashed lines) for state B in figure 5.4. Note that the time axes have been normalized by the period T.

modulation cycle. At $t = T/8$ the distribution of angular momentum is almost uniform as the Taylor cells from the previous cycle have almost completely decayed, but they soon re-develop and reach maximum amplitude at about $t = T/4$ with a strong outflow jet of angular momentum erupting from the inner cylinder boundary layer at $z = \pi/k^B$, and a weaker inflow jet from the outer cylinder boundary layer at $z = 0$. Subsequently, the cells decay until the rotation of the inner cylinder becomes supercritical in the opposite direction and the Taylor cells reappear at the same axial locations at $t = 3T/4$. This indicates that a time evolution of $T/2$ leaves the azimuthal vorticity invariant, with the axial locations of the inflow and outflow jets remaining unchanged. The time evolution of a half-period corresponds to a change of sign in the angular momentum, as it does for the basic state. It is therefore evident that the bifurcation to B preserves the spatio-temporal symmetry S. This can also be seen in figure 5.5, showing the time series of the radial and azimuthal perturbation velocities, u_r and u_θ, at $(r, \theta, z) = (1.5, 0, \pi/k^B)$ (solid lines) and $(r, \theta, z) = (1.5, 0, 0)$ (dashed lines). The radial velocity time series are $T/2$-periodic, so that there is no reversal in the sense of circulation in the Taylor cells. However, the azimuthal velocity is T-periodic, with symmetrically opposed maxima and minima at t and $t + T/2$, i.e. $u_\theta(r, \theta, z, t) = -u_\theta(r, \theta, z, t + T/2)$, and S is preserved.

The time evolution of state A over a modulation period is illustrated in figure 5.6, showing contours of angular momentum and azimuthal vorticity. The behavior is similar to that of B, although in this case it is clear that a time evolution of $T/2$ does not leave

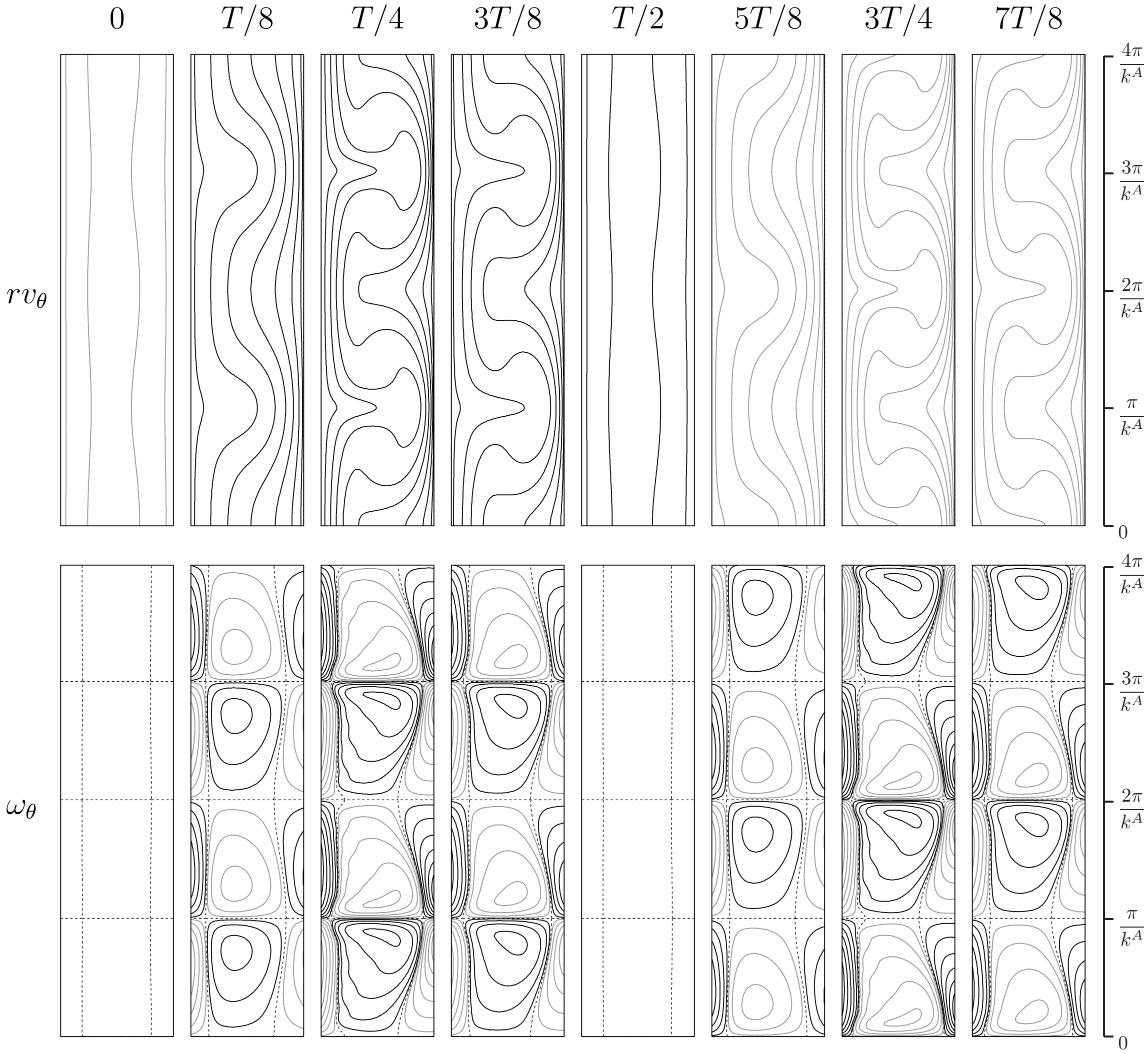

Figure 5.6: Type A (reversing) Taylor vortex flow at $\omega = 1$ and $Re_a = 240$ with wavenumber $k^A = 3.0$. Quadratically spaced contours of angular momentum (top row) and azimuthal vorticity (bottom row) are shown in a meridional cross-section over a period T. Black (gray) contours correspond to positive (negative) values, showing $r \in [1, 2]$ and $z \in [0, 4\pi/k^A]$.

the azimuthal vorticity invariant; the locations of the inflow and outflow jets are shifted by half and axial wavelength π/k^A each half-period (compare snapshots at $t = T/4$ and $t = 3T/4$, for example). Note that this does not correspond to a reflection but to an axial shift of the pattern

$$T_{\pi/k^A}\mathbf{v}(r, \theta, z, t) = \mathbf{v}(r, \theta, z + \pi/k^A, t). \tag{5.7}$$

The change in sign of angular momentum together with this half wavelength axial shift indicates that the spatio-temporal symmetry S has been broken. Nevertheless, A is invariant under a new Z_2 spatio-temporal symmetry S', consisting of S composed with

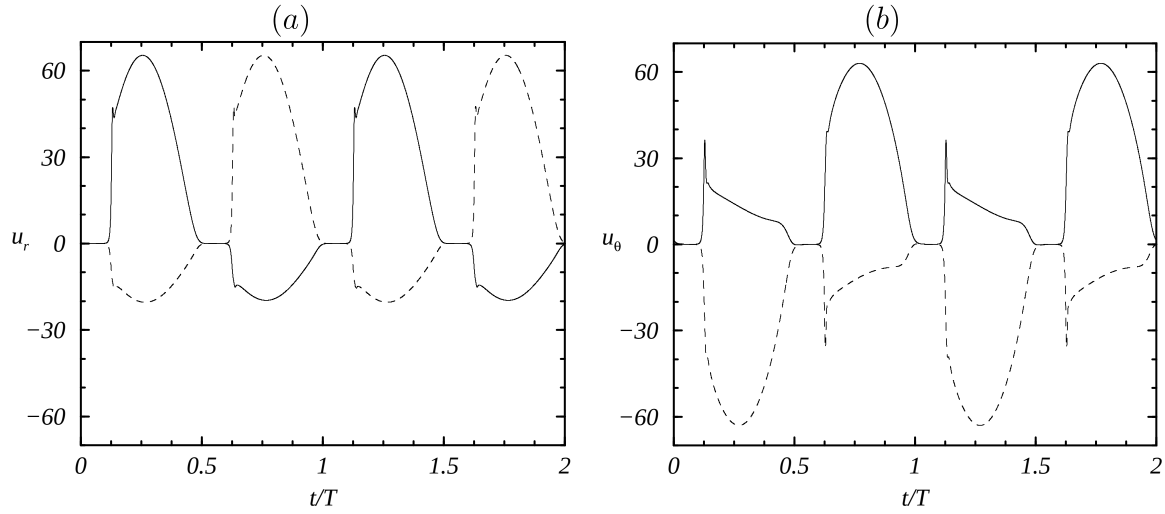

Figure 5.7: Evolutions over two periods of (a) the radial velocity and (b) the azimuthal velocity components of the perturbation field (2.18) recorded at $(r, \theta, z) = ((r_i + r_o)/2, 0, \pi/k^A)$ (solid lines) and $(r, \theta, z) = ((r_i + r_o)/2, 0, 0)$ (dashed lines) for state A in figure 5.6.

the axial translation T_{π/k^A}. Its action on the velocity field is:

$$S'(\mathbf{v})(r, \theta, z, t) = (v_r, -v_\theta, v_z)(r, -\theta, z + \pi/k^A, t + T/2). \tag{5.8}$$

The replacement of S by S' in the bifurcation to A is manifest in the time-series of the radial and azimuthal perturbation components shown in figure 5.7. A time evolution of half a period changes the sign of the radial velocity, illustrating the exchange between outflow and inflow boundaries as a result of the axial shift. If this time evolution is composed with T_{π/k^A}, which corresponds to swapping from solid to dashed line or vice-versa, then the radial velocity is unchanged. The azimuthal component is only invariant after further applying the reflection K_θ. These symmetry considerations fully agree with the results from equivariant normal form theory presented in Appendix D.

5.2.3 Experimental characterization of the flows

The critical $Re_{a,c}$ from the Floquet analysis corresponds to the Re_a at which the net growth of the most dangerous perturbation over a period is zero. For $Re_a \gtrsim Re_{a,c}$, the fraction of the period during which the motion of the cylinder is subcritical ($Re_i(t) = Re_a \sin \omega t < Re_{i,c}$) is large, and the vortices decay to energy levels which are limited by the level of background noise (Hall, 1983; Barenghi & Jones, 1989). For larger Re_a, the signal-to-noise ratio is increased, and so the experimental results of Mr. Michael

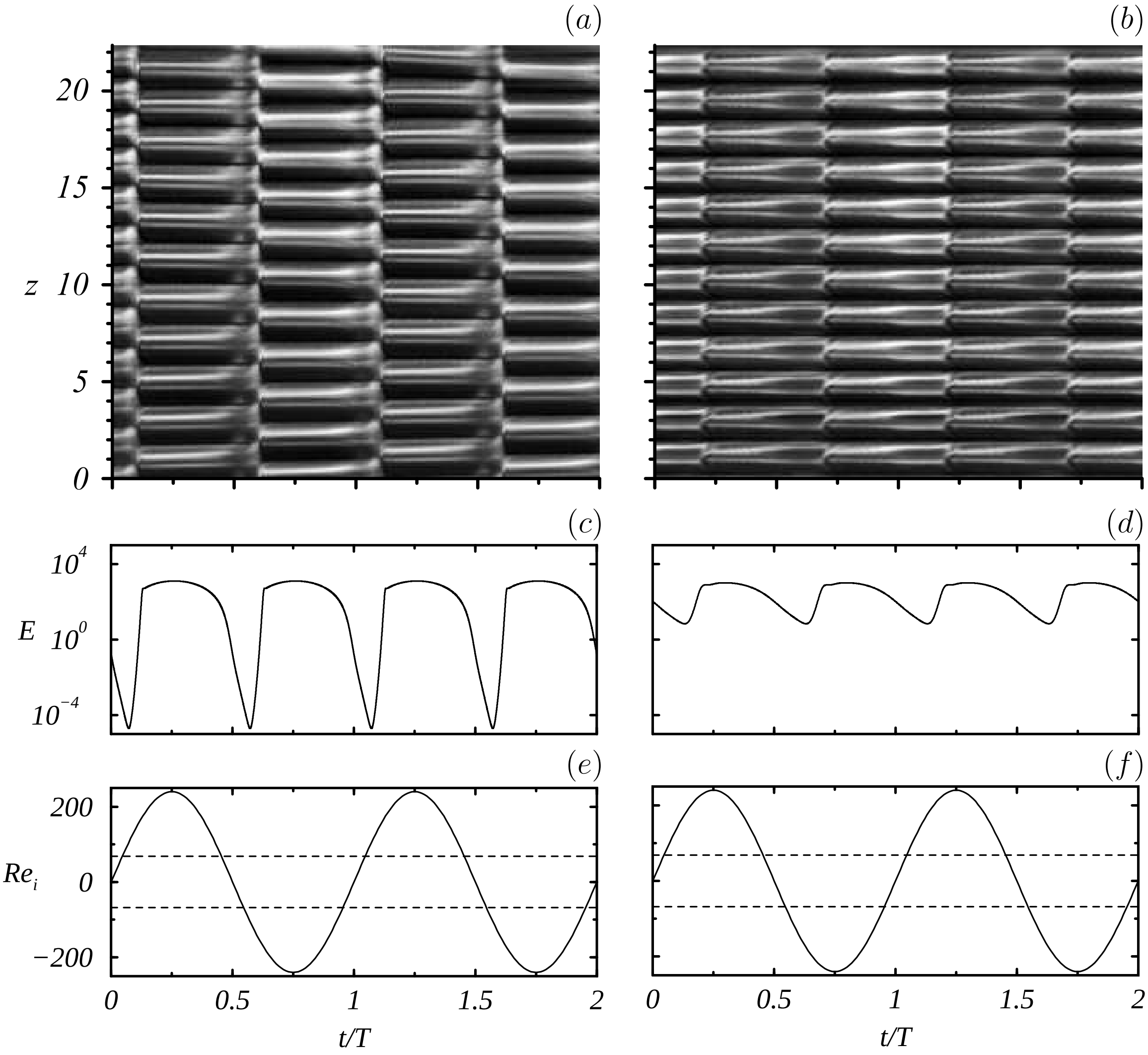

Figure 5.8: Experimental space-time diagrams of the time evolution at $Re_a = 240$ of (*a*) state A at $\omega = 1$ with $k^A = 3.0$ and (*b*) state B at $\omega = 6.1$ with $k^B = 3.4$; the corresponding computed kinetic energies of the perturbation field $\mathbf{u}$ are shown in (*c*) and (*d*), and the corresponding instantaneous Reynolds numbers $Re_i(t) = Re_a \sin \omega t$ (solid curve) are given in (*e*) and (*f*) which also include $Re_{i,c} = \pm 68.19$ (dashed lines).

Belisle reported in this chapter have been performed at $Re_a = 240$, well beyond onset at $Re_{a,c} \approx 110$. At $Re_a = 240$, the motion of the cylinder is subcritical only 18.3% of the period, giving an acceptable signal-to-noise ratio which results in clean synchronous secondary flows. The experimental characterizations at $Re_a = 240$ of A at $\omega = 1.0$ and B at $\omega = 6.1$ are shown as space-time diagrams in figures 5.8(*a*) and 5.8(*b*). A and B can be clearly distinguished by the behavior of the jets separating the Taylor cells. In figure 5.8(*a*) the jets of A shift half a wavelength every half period, and in figure 5.8(*b*) the jets of B do not shift. The corresponding wavenumbers for these particular experimental runs are $k^A = 3.0$ and $k^B = 3.4$, consistent with the nonlinear computations.

Youd *et al.* (2003) noted that the most striking feature of A is the exponential growth and decay that the vortices experience every half-period. This behavior is manifest in the computed kinetic energy time series of A at $Re_a = 240$ and $\omega = 1$ shown in figure 5.8(c). At this low frequency, the response is quasi-steady to the continuous but slow change in $Re_i(t)$. At $t = 0$, corresponding to $Re_i(t) = 0$, the vortices are decaying exponentially and reach a minimum of kinetic energy shortly after the motion of the cylinder becomes supercritical ($Re_i(t) = Re_{i,c}$). The instantaneous $Re_i(t)$ is shown in figure 5.8(e) (and in figure 5.8(f) for the $\omega = 6.1$ case) as a solid line together with $\pm Re_{i,c}$ (dashed lines) so as to clearly identify the phases of the cycle during which the cylinder motion is super- and sub-critical. The decay of the vortices can also be seen in the experimental space-time diagram of figure 5.8(a), where the vortices are observed to fade away (the intensity tends to an axially uniform shade of grey). Subsequently, the vortices grow exponentially until the flow saturates nonlinearly at $t/T = 0.133$ and algebraic growth follows. The algebraic growth continues to $t/T = 0.25$, when the maximum amplitude of the modulations $Re_i(t) = 240$ is achieved, and it is followed by algebraic decay as the cylinder slows down. In the experiments, this long phase of algebraic behavior is distinguished by a greater contrast in the reflected light across the vortices. When the rotation of the cylinder again becomes subcritical, the vortices decay exponentially. Due to the spatio-temporal symmetry S', this sequence is repeated every half period, i.e. the kinetic energy time series is $T/2$ periodic.

The behavior of B at a higher frequency $\omega = 6.1$ is qualitatively different. In this case, the flow does not have time to adjust quasi-steadily to the rapidly changing $Re_i(t)$. This results in a delay of the response as can be seen in the kinetic energy time series of figure 5.8(d), and also in the space-time diagram of figure 5.8(b). In particular, the flow saturates nonlinearly at $t/T = 0.215$, in comparison to A at $\omega = 1$ which saturates at $t/T = 0.133$. Although the flow is subcritical the same fraction of the period in the two cases, since the period is six times shorter in viscous time units for B at $\omega = 6.1$, and the growth rates for A and B in viscous time units are comparable ($\mathrm{e}^{-22.9t}$ and $\mathrm{e}^{-23.4t}$, respectively), the exponential decay of A at $\omega = 1$ during this fraction leads to vortices with minimum energy of about six orders of magnitude smaller than for B at $\omega = 6.1$.

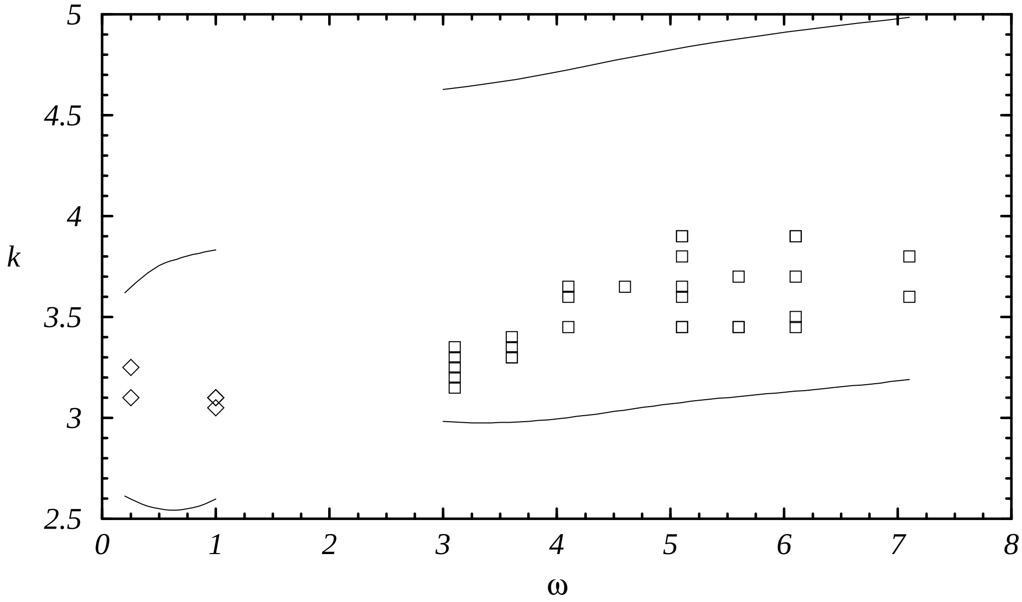

Figure 5.9: Experimentally observed axial wavenumbers k of A ($\diamond$) and B ($\square$) in several experimental runs at $Re_a = 240$. The solid lines correspond to the Eckhaus curves from the nonlinear computations.

5.2.4 Wavenumber selection of the flows

The neutral stability curves shown in figure 5.3 indicate that at $Re_a = 240$ solutions with a wide range of axial wavenumbers k can be selected. The stability of these flows is limited by the Eckhaus bifurcation curves. In the experiments, the axial wavenumber that is selected depends on perturbations and initial conditions that are not completely controllable and cannot be fully characterized. Repeated experimental runs at the same point in parameter space (Re_a, ω) lead to states with different k well within the Eckhaus-stable band. Similar multiplicity of states in classical Taylor–Couette flow is well-known (Coles, 1965). Figure 5.9 shows the axial wavenumbers of A (diamonds) and B (squares) observed in several experimental runs at $Re_a = 240$ and various ω. (Results in the interval $1 < \omega < 3$ are presented in §5.3 as they correspond to the competition region.) After transients have decayed, the Taylor cells are of uniform wavelength and no defects are observed. All the observed k are inside the Eckhaus bands as determined by nonlinear computations. These are shown in solid lines in figure 5.9.

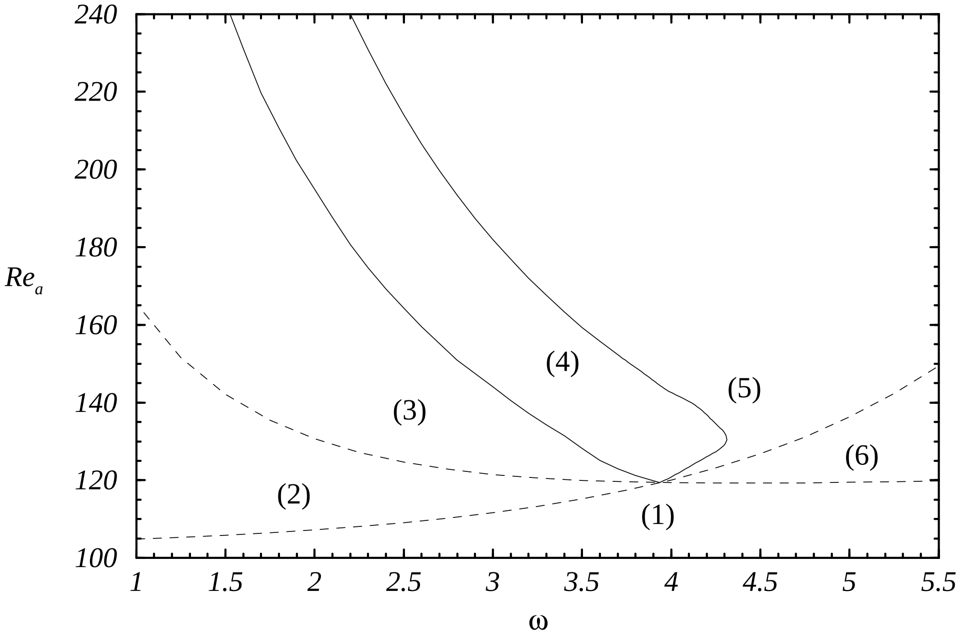

Figure 5.10: Bifurcation diagram of the competition between types A (reversing) and B (non-reversing) Taylor vortex flows. Bracketed numbers correspond to regions in parameter space with qualitatively different dynamics. A schematic of their phase portraits are shown in figure 5.11.

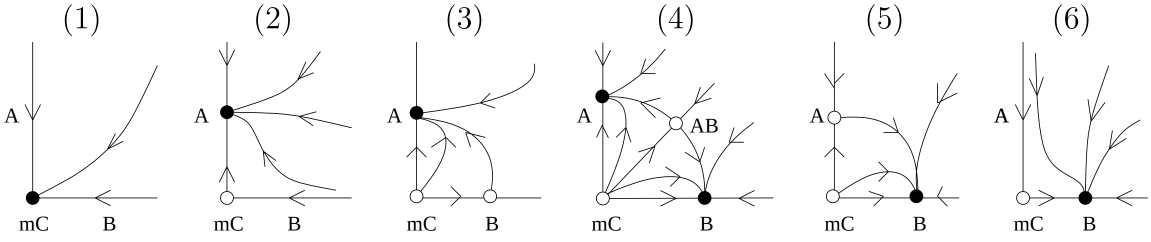

Figure 5.11: Schematic of the phase portraits of the mode competition dynamics in the six regions delimited by the bifurcation curves in figure 5.10. Open (closed) circles are unstable (stable) fixed points of the Poincaré map $\mathcal{P}$.

5.3 Mode competition: bifurcation scenario

We have numerically investigated the competition between A and B in a wide region of parameter space around the codimension-two point where they bifurcate simultaneously, $(\omega, Re_{a,c}) = (3.936, 119.4)$. The critical axial wavenumbers for A and B from Floquet analysis are $k_c^A = 2.71$ and $k_c^B = 3.82$. Let's assume for now that only one A and one B, with fixed incommensurate k_c^A and k_c^B, exist in the neighborhood of this codimension-two point. This classical simplification allows one to interpret the bifurcation scenario in terms of standard equivariant bifurcation theory while preserving the essentials of the competition dynamics. The effects of the presence of two families of flows A and B, given by the Eckhaus bands, shall be addressed in the next paragraph. Figure 5.10 shows the bifurcation diagram of the competition between A and B in a wide region of parameter space. For Re_a and ω in region 1 the basic state mC is the only flow that exists and it is stable. Crossing into region 2, mC becomes unstable and A emerges as a stable state via a synchronous symmetry-breaking bifurcation. Upon crossing into region 3, B emerges from another synchronous bifurcation from mC, but it is unstable and only stabilizes in region 4 where an unstable mixed-mode AB is born. In region 4, A and B coexist and are both stable. Depending on initial conditions, either of them may be obtained. The situation is analogous when starting from region 1 and crossing into regions 6 and 5 to reach region 4. As all the bifurcations are supercritical, these paths in parameter space can be reversed and the same results hold. The detailed analysis of this bifurcation is presented in Appendix D in terms of equivariant normal form theory. Figure 5.11 shows a schematic of the phase portraits in the six regions of parameter space indicating the stability of the flows, summarizing the results in Appendix D.

Note that at any point in parameter space with $Re_a > Re_{a,c}$ there exist not a single A or a single B, but two families of these flows. Therefore, on performing nonlinear computations to determine the bifurcation curves in figure 5.10, it is necessary to consider A and B with different axial wavenumbers (all of them multiples of the small fundamental $k_0 = 0.15$). Their stability is determined as explained in § 2.3. Let's say we start a simulation with $\omega = 3.2$ and $Re_a = 140$ and obtain B_{50} with wavenumber $k^B = 3.75$, corresponding to 50 Taylor cells ($l = 25$). Upon decreasing the Reynolds number to $Re_a = 138$, we cross from region 4 to region 3, B_{50} becomes unstable and the system evolves to A_{38} (with $k^A = 2.85$). However, at this Re_a and ω, B_{52} (with $k^B = 3.9$) is still stable and is only destabilized when Re_a is further reduced to 137. Likewise, for each pair $(A_{2l}, B_{2l'})$ there exists a set of bifurcation curves. Region 4 in figure 5.10 is defined as all points in parameter space where at least a stable A and a stable B coexist simultaneously. The boundaries of region 4 consist of segments from the bifurcation curves at which various A and B lose stability. Note that in region 4, there exists not a single unstable mixed mode AB, but a family of such modes.

A typical example of the nonlinear dynamics of the transition from A to B when crossing from region 4 to region 5 is shown in the space-time diagram of figure 5.12. In the plot, we have arbitrarily set $t = 0$, however by this time the flow had evolved for many periods until a stable A_{36} was obtained at $Re_a = 140$ and $\omega = 4$ (region 4). Then, at $t = 0$ a small perturbation (with energy several orders of magnitude lower than

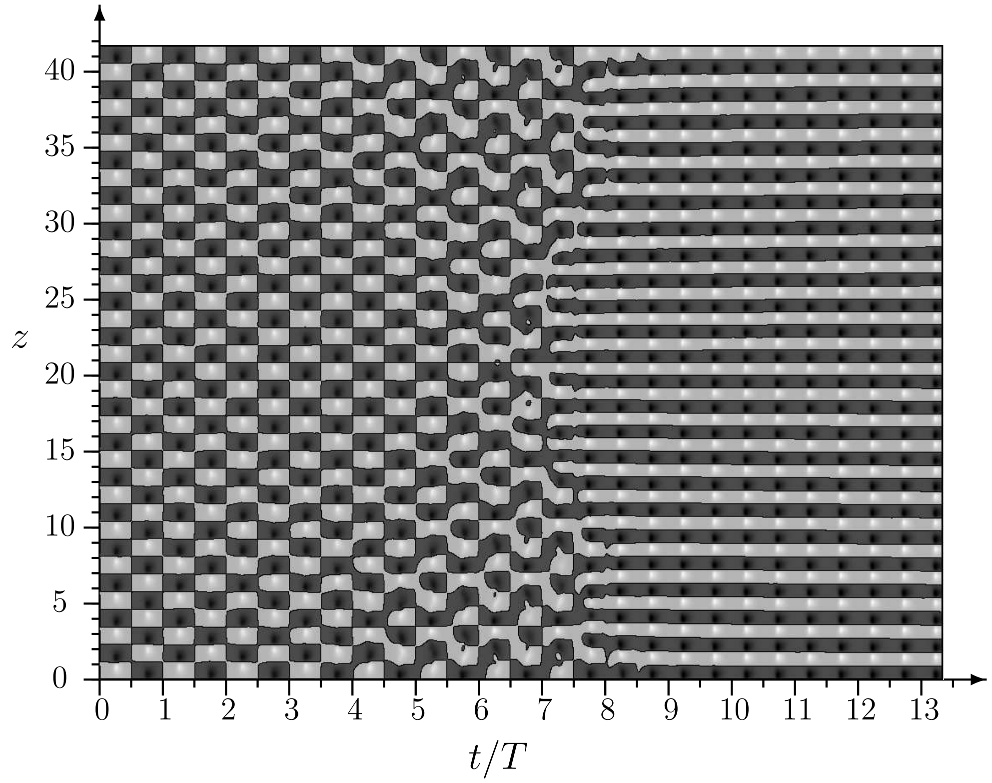

Figure 5.12: Space-time diagram showing an azimuthal vorticity color-map at $(r,\theta) = (r_o, 0)$ over time and the whole computational domain in the axial direction $z \in [0, \Lambda]$. Black (gray) corresponds to positive (negative) values. The initial condition is A_{36} at $\omega = 4$ and $Re_a = 140$. At $t = 0$ the frequency is increased to $\omega = 4.2$ and the system starts evolving to B_{48}.

that of the flow) was introduced and the frequency was raised to $\omega = 4.2$, thus entering region 5 where A is unstable. After a transient (of about 10 periods) during which A and B compete, the flow settles to B_{48}. Before the transition, the half-wavelength axial shifts of A_{36} every half-period are evident. Following the transition to B_{48}, the flow no longer shifts axially and has a larger wavenumber. Figure 5.13 shows the transition from B to A when crossing from region 4 to region 3. The initial state is B_{50} at $Re_a = 140$ and $\omega = 3.2$, and upon decreasing the frequency to $\omega = 3.0$, the flow evolves to A_{38}.

5.3.1 Experimental dynamics of the competition at $Re_a = 240$

We have conducted experiments at $Re_a = 240$ to verify the bifurcation scenario and identify the regions in parameter space predicted by the nonlinear computations. In the low frequency regime, $\omega \leq 1$, corresponding to region 3 in figure 5.10, the only observed flow is A. For frequencies $\omega \geq 3$, corresponding to region 5, only B is observed. These

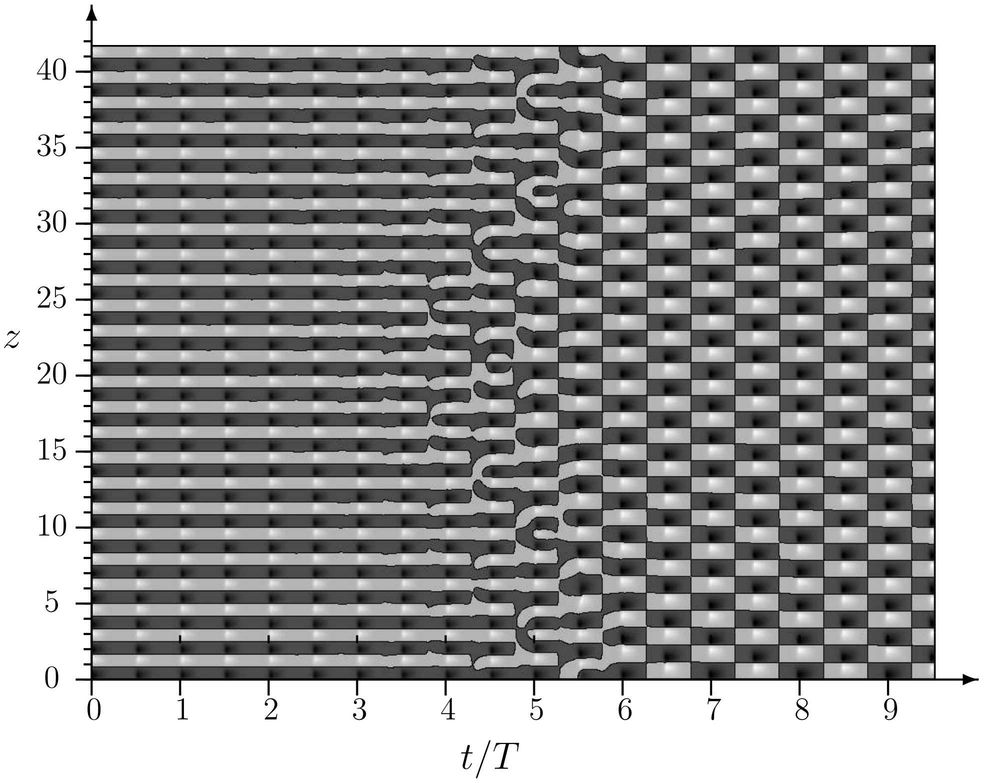

Figure 5.13: Same as Figure 5.12. The initial condition is B_{50} at $\omega = 3.2$ and $Re_a = 140$. At $t = 0$ the frequency is decreased to $\omega = 3.0$ and the system evolves to A_{38}.

flows are characterized by a well-defined time-independent axial wavenumber k. The observed values of k are given in figure 5.9.

The experimental procedure to detect the boundaries of the coexistence region 4 is as follows. The apparatus is operated at $\omega \geq 6$ in region 5 and far from region 4 as determined by the nonlinear computations, which at $Re_a = 240$ spans from $\omega \in (1.53, 2.20)$. After transients have decayed, a spatially regular B is obtained. Then, the frequency is decreased to say $\omega = 5$. There is a rapid initial adjustment via vortex mergers or splits (defects in the pattern which appear at random axial locations) on a time scale of about $2\pi/\omega$ (on the order of d^2/ν for the range of frequencies investigated). This is followed by a slower adjustment of the wavelength on the viscous time scale associated with the distance between endwalls ($\Gamma d^2/\nu$). The frequency is subsequently reduced further and different B are obtained at various ω. Following each of these changes in ω, we observe the same type of rapid adjustment via defects followed by the gradual relaxation. However, close to region 4 (at about $\omega \sim 3$) the defects do not vanish after a period but are persistent in time. Figure 5.14 shows a typical space-time diagram of an experimental run in this parameter regime, with $Re_a = 240$ and $\omega = 2$. The flow does

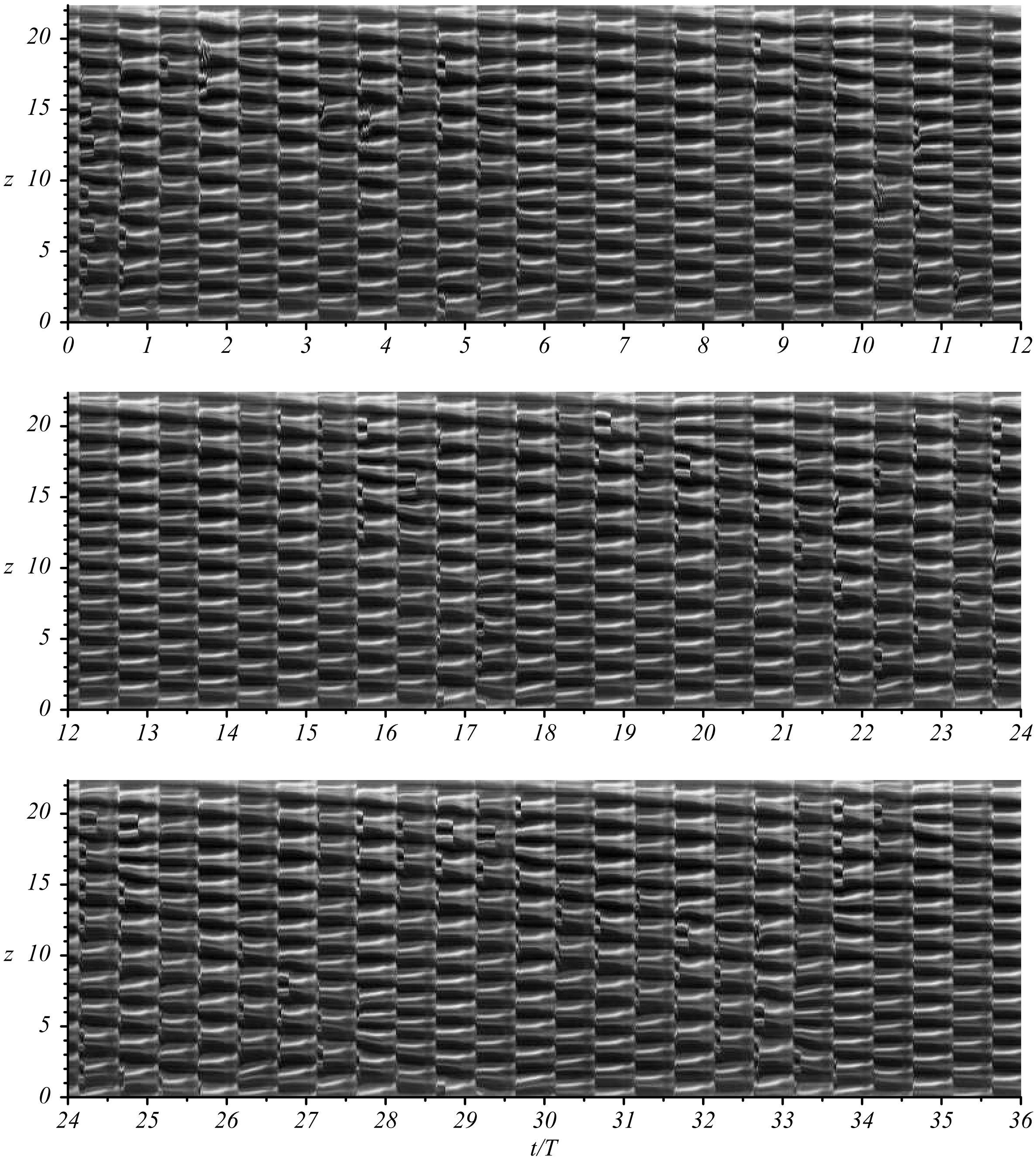

Figure 5.14: Space-time diagram showing the time evolution of a noise-sustained flow in region 4 at $\omega = 2.0$ and $Re_a = 240$ over 36 periods, corresponding to 113 viscous time units. At $t/T = 0$, the frequency was changed from a stable flow at $\omega = 1.0$.

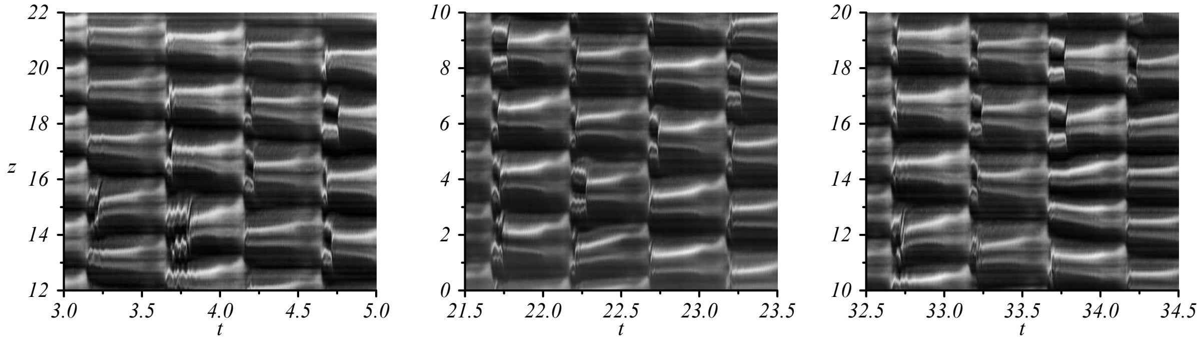

Figure 5.15: Close-ups of the images in figure 5.14 showing typical defects.

not settle on a particular axial wavenumber and there are abrupt appearances of defects over the whole experimental run (which lasted 36 periods, corresponding to about 120 viscous times). The defects are evident when the flow saturates nonlinearly, and when $Re_i(t)$ peaks at about $|Re_i(t)| = 240$ the cells are more spatially uniform. The defects appear at random axial locations each half-period and the dominant axial wavenumber is apparently randomly selected in time with values $k \in [2.9, 4.0]$, showing no clear trend (a few close-ups of the images in figure 5.14 are presented in figure 5.15 showing typical defects). The flow cannot be regarded as either A or B; the jets separating the vortices shift by irregular amounts in space and time. This type of behavior is observed following decreases in ω, until we reach $\omega = 1$. Following a decrease to $\omega = 1$, the defects quickly disappear within about one period, and the Taylor cells adjust slowly to a uniform axial wavenumber k. At this ω, the jets shift by half a wavelength every half-period, corresponding to A. This whole scenario is reversed with increasing ω, i.e. we did not detect any hysteresis with varying ω.

5.4 Discussion and conclusions

Nonlinear dynamics of the time modulated Taylor–Couette system has been investigated experimentally and numerically by solving the unsteady three-dimensional Navier–Stokes equations. The aspect ratio of the experimental apparatus is $\Gamma = 115$, whereas in the nonlinear computations a long periodic annulus of wavelength $\Lambda = 41.89$ has been considered. The study has been focused on temporal modulations about a zero mean. In this case, the basic state is characterized by the presence of a Z_2 spatio-temporal symmetry, S, in addition to the spatial symmetries of the classical Taylor–Couette system.

The onset of instability has been determined by Floquet analysis of the basic state, which shows that two distinct Taylor vortex flows A (reversing) and B (non-reversing) are born at synchronous symmetry-breaking bifurcations of the modulated Couette flow. This result resolves the discrepancies between previous Floquet analyses for finite gaps (Carmi & Tustaniwskyj, 1981; Barenghi & Jones, 1989) and narrow gap (Riley & Laurence, 1976). Moreover, experimental evidence of the existence of A and B has been provided for the first time. The dynamical behavior of A and B and the observed axial wavenumbers are in good agreement with the predicted values from Floquet analysis and nonlinear computations. The stability of the basic state has been investigated using the half-period-flip map $\mathcal{H}$ instead of the Poincaré map $\mathcal{P} = \mathcal{H}^2$. This approach sheds light on the nature of the symmetry-breaking bifurcations to A and B, while also having the practical advantage of halving the computational time. The bifurcation to B preserves the spatio-temporal symmetry S, whereas the bifurcation to A breaks it and a new spatio-temporal symmetry S' emerges, consisting of S composed with an axial shift of half a wavelength. Flows with precisely the same symmetries as A and B arise in other systems, such as the periodically driven cavity flow (Marques *et al.*, 2004) and cylinder wake flows (Barkley & Henderson, 1996), via analogous bifurcations in the transition from two-dimensional to three-dimensional flow (Blackburn *et al.*, 2005). However, in modulated Couette flow, the transition is from one-dimensional to two-dimensional flow, highlighting that the symmetry group of the system, and in particular of the flow from which the bifurcations occur, determines the spatio-temporal characteristics of the bifurcated flows regardless of the specifics of the problem. Therefore, a careful consideration of the symmetries of the system provides not only the key to understand the nature of the two bifurcated flows, but furnishes the setting to compare systems with inherently different physical instability mechanisms.

In previous studies, direct numerical simulation had been focused on investigating the codimension-one bifurcations leading to the two states with distinct spatio-temporal symmetries. The flow in the wake of a cylinder is governed by a single parameter, the Reynolds number Re, so that a study of the mode competition between A and B is impractical (two parameter variations are required to explore the competition dynamics organized by the codimension-two point where both modes bifurcate simultaneously). State A bifurcates first at lower Reynolds number, so a pure state B is never observed in the cylinder wake experiments and can only be obtained in the computations by prescribing the wavenumber. The transition is found to be gradual from A to B in experiments (Williamson, 1996) and to some extent in nonlinear computations (Henderson, 1997). Barkley, Tuckerman & Golubitsky (2000) proposed a system of two coupled amplitude equations based on the assumption of the existence of a codimension-two point where A and B bifurcate simultaneously; the experimentally observed transition was described as a one-dimensional path (parameterized with Re) in a two-parameter model. In modulated Taylor–Couette flow, the study of the competition between the analogous states A and B is more straight-forward as the two parameters, Re_a and ω, can be varied. Youd *et al.* (2003) obtained A and B with nonlinear computations for the first time. In a subsequent study, Youd *et al.* (2005) also investigated the secondary transition to three-dimensional flows and showed that non-reversing spiral flows occur. However, their approach, in which they computed for a single mode with a prescribed wavelength, was unable to study mode competition and pattern selection. At about the same time, Youd & Barenghi (2005) also considered the problem in a finite annulus with stationary rigid endwalls and relatively short aspect ratios, and found that both states A and B continue to exist. Although mode competition could have been studied along the line presented here, they did not perform such an analysis and only considered two modulation frequencies, $\omega = 3$ and $\omega = 7$. The effects of rigid endwalls and finite aspect ratios on the competition between states A and B remains an open question.

In this chapter we have numerically and experimentally investigated the competition between A and B in the two-dimensional parameter space (ω, Re_a). In the nonlinear computations, A and B coexist and the two are stable in a narrow region of parameter space where a mixed-mode AB also exists but is unstable. In fact, in this region there are families of A and B and mixed-modes. In the experiments neither A nor B has been observed in the coexistence region. Instead, we have found that noise sustains flows with irregular time-dependent axial wavenumber. Outside this region, for lower frequency only A is observed, and for higher frequency only B is observed, in good agreement with the numerical simulations and the Floquet stability analysis. It is thus of interest to determine the nature of the flows observed in the coexistence region, and in particular to determine if it is noise sustaining a mixed mode generated by a combination of A and B with a wide range of axial wavenumbers.

CHAPTER 6
OVERVIEW AND DISCUSSION

In the quest for understanding the general question of transition to spatio-temporal complexity and turbulence in natural flows, there has been a need to seek more fundamental flows from which the important physics can be extracted. Researchers in the past century considered idealized problems with simple geometries which have led to the rigorous development of hydrodynamic instability theory. Since the pioneering work of Taylor (1923), the Taylor–Couette flow has been used as canonical flow for centrifugal instability and transition to turbulence following a progression of flow instabilities. In this thesis, we have investigated several variations of the classical Taylor–Couette system leading to very rich dynamical behavior. The work has been motivated by experimental observations of complex flows whose origin was unclear. Our approach has combined Direct Numerical Simulations of the three-dimensional Navier–Stokes equations with equivariant bifurcation and normal form theories to uncover the key factors behind the experimentally observed behavior. The results have been compared to related flows with different physical instability mechanisms, highlighting that the symmetry group of the basic flow from which the bifurcations occur determines the characteristics of the secondary flows regardless of the specifics of the problem.

After introducing the Taylor–Couette system and numerical methodology in chapters 1 and 2, we have investigated the effect of an axial pressure gradient in the co-rotating Taylor–Couette system in chapter 3. The bifurcation scenario leading to coexistence of spiral waves of opposite angle, similar to those experimentally observed by Nagib (1972), has been elucidated. Our numerical computations show that these states consist of the superposition of spiral waves propagating in opposite axial direction. This had been conjectured by Meseguer & Marques (2005*a*) from linear instability results. However, care must be taken when using periodic boundary conditions to simulate Poiseuille type flows. In the experiments, perturbations at the inlet of the apparatus are carried away and swallowed at the outlet. Therefore, the observation of secondary motion in the convectively unstable regime depends on the length of the apparatus and amplitude of the perturbations at the inlet (Babcock *et al.*, 1994). In the Navier–Stokes equations with periodic boundary conditions, perturbations re-enter the system and no distinction is possible between the convectively and absolutely unstable regimes. Therefore, the numerical simulation of open flows has been and continues to be a major challenge, as the boundary conditions are not well defined. Although the numerical results in chapter 3 are most likely in the convective regime, and may be in fact never obtained in a laboratory experiment, the generic bifurcation mechanism leading to interpenetrating spirals presented here remains valid. In addition, the flows have been obtained using periodic boundary conditions, so it seems clear that the related flows observed by Nagib in different parameter regimes are due to linear instabilities and not to extraneous experimental inlet/outlet effects not captured by our model.

In chapter 4, the nonlinear dynamics of the Taylor–Couette flow with axial oscillations of the inner cylinder has been investigated. In contrast to the spiral Poiseuille flow, the oscillating Taylor–Couette flow is an enclosed system, which we have approximated imposing a zero net axial mass flow at any instant in time. The motivation to study these type of flows stemmed from the experimental observation of Weisberg *et al.* (1997) that harmonic axial oscillations led to a parametric suppression of the onset of instability. They noted that in certain ranges of forcing frequency and amplitude they observed erratic behavior being excited directly from the basic state. Marques & Lopez (1997, 2000) showed that this complex behavior was tied to parametric excitation of non-axisymmetric modes via a Neimark-Sacker bifurcation. The dynamics of these non-axisymmetric spiral modes was the subject of recent experiments by Sinha *et al.* (2006), who investigated the presence of resonances between forcing and Neimark–Sacker frequencies. Our work on this problem has shed light on the nature of the erratic behavior observed in the experiments by Weisberg *et al.* (1997) and Sinha *et al.* (2006). We have found that once instability has set in, a rapid sequence of symmetry-breaking bifurcations results in complex spatio-temporal dynamics even for very low post-critical values of the rotation of the inner cylinder. In particular, we have shown that these bifurcations, which cannot be experimentally detected due to the precision required, are responsible for some of the experimentally observed frequencies which were attributed to background noise. The breaking of all the spatial and temporal symmetries leading to defective spiral flow, termed as M4 in chapter 4, results in chaotic behavior at a Reynolds number for which time-periodic and spatially regular Wavy vortex flow is observed in the unforced case. Wavenumber competition in both azimuthal and axial directions leads to broad spatial and temporal spectra. This type of flows were experimentally observed in Taylor–Couette flow with stationary outer cylinder and rotating inner cylinder by Brandstäter & Swinney (1987), following the transition from Modulated wavy vortex flow. Noteworthy, in the axially forced case our computations and experiments by Sinha *et al.* (2006) show that these regimes can be realized at Reynolds numbers one order of magnitude below those of the classical Taylor–Couette experiment. Therefore this type of *weak turbulence*, as termed by Brandstäter & Swinney (1987), is not intrinsic to the momentum of the system.

In chapter 5, we have explored the effect of oscillating the rotation of the inner cylinder about a zero-mean, following previous computational works (Riley & Laurence, 1976; Youd *et al.*, 2003). The resulting time-modulated circular Couette flow possesses a Z_2 spatio-temporal symmetry which gives rise to two distinct modulated Taylor vortex flows. These flows are initiated at synchronous bifurcations, have the same spatial symmetries, but are characterized by different Z_2 spatio-temporal symmetries and axial wavenumber. Flows with precisely the same symmetries arise in periodically driven cavity flow (Marques *et al.*, 2004) and cylinder wake flows (Barkley & Henderson, 1996) in the transition from two-dimensional to three-dimensional flow. Mode competition between these two states, termed as A and B, has been investigated in the neighborhood where they bifurcate simultaneously. The experiments and computations show that for low frequencies only A is observed, whereas for high frequencies only B is observed. In the nonlinear computations, A and B coexist and the two are stable in the mid-frequency regime. However, in the physical experiment, neither state has been observed in the coexistence region. Instead, noise-sustained flows with irregular time-dependent axial wavenumber have been observed. This finding poses a fundamental question of interest in mode competition and pattern formation. In particular it is noteworthy that the wavenumber selection fails only in the mid-frequency coexistence region. For lower frequencies, where noise effects are expected to be more pronounced due to the long time that perturbations have to grow and decay, regular spatially and temporally periodic flows were in fact observed.

Overall, the research presented in the thesis has resolved several issues that arose in previous experimental and numerical works in Taylor–Couette flows. In turn, the new results have given rise to interesting questions in flow transition and pattern formation. It would be interesting to determine the bifurcation scenario that leads to chaotic flow from the quasi-periodic interpenetrating spirals observed in spiral Poiseuille flow. This may be similar to the broadening of the spatial and temporal spectra following Modulated wavy vortex flow and also observed in chapter 4. In the axially oscillating Taylor–Couette flow, only flows that break the Z_2 spatio-temporal symmetry of the basic state have been observed (these correspond to modulated traveling waves M1). It is expected that the modulated standing waves predicted in Appendix C exist in other parameter regimes and follow a different route to chaotic flow. In modulated Taylor vortex flow, both states breaking (A) and preserving (B) the azimuthal spatio-temporal Z_2 symmetry have been observed. However, state A features a new type of spatio-temporal Z_2 symmetry, whereas the modulated traveling waves M1 of chapter 4 do not.

Finally, the effects of finite aspect ratios on the competition between states A and B of chapter 5 will be investigated. This study should be complemented with experiments with rigid end-walls to determine if the noise-sustained flows observed in the current experimental apparatus persist. Efforts are now focused on the implementation and testing of an efficient spectral Navier–Stokes solver for realistic and flexible boundary conditions, including rigid end-walls. Nonetheless, computations with periodic boundary conditions will still be of interest in order to compare results and thus assess the role of end-wall effects on the dynamics of the flows.

APPENDIX A
SOLENOIDAL SPECTRAL BASES

The divergence-free condition for a perturbation field $\mathbf{u}$ of the form (2.8) is $D_+u_r + \mathrm{i}nu_\theta/r + iku_z = 0$, where $D = \partial/\partial_r$ and $D_+ = D + 1/r$. In the axisymmetric subspace of V, the basis is given by

$$\mathbf{u}^{(1)}_{knm}(r) = \begin{pmatrix} 0 \\ h_m \\ 0 \end{pmatrix}, \qquad \mathbf{u}^{(2)}_{knm}(r) = \begin{pmatrix} -\mathrm{i}krg_m \\ 0 \\ D(rg_m) + g_m \end{pmatrix}, \tag{A.1}$$

except that the third component of $\mathbf{u}^{(2)}_m$ is replaced by h_m when $k = 0$. The functions h_m and g_m are expanded with Chebyshev polynomials $T_m(x)$

$$h_m(r) = (1 - x^2)\mathrm{T}_m(x), \qquad g_m(r) = (1 - x^2)^2\mathrm{T}_m(x), \tag{A.2}$$

where

$$x(r) = 2r - \frac{1+\eta}{1-\eta}, \tag{A.3}$$

maps the radial domain $r \in [r_i, r_o]$ to the interval $x \in [-1, 1]$. For the the non-axisymmetric case the basis is

$$\mathbf{u}^{(1)}_{knm}(r) = \begin{pmatrix} -\mathrm{i}ng_m \\ D(rg_m) \\ 0 \end{pmatrix}, \qquad \mathbf{u}^{(2)}_{knm}(r) = \begin{pmatrix} 0 \\ -\mathrm{i}krh_m \\ \mathrm{i}nh_m \end{pmatrix}, \tag{A.4}$$

except that the third component of $\mathbf{u}^{(2)}_m$ is replaced by h_m when $k = 0$.

For the projection space, the basis corresponding to axisymmetric fields is

$$\tilde{\mathbf{u}}^{(1)}_{knm}(r) = \mathrm{w}(x) \begin{pmatrix} 0 \\ rh_m \\ 0 \end{pmatrix}, \quad \tilde{\mathbf{u}}^{(2)}_{knm}(r) = \frac{\mathrm{w}(x)}{r^2} \begin{pmatrix} \mathrm{i}kg_m \\ 0 \\ D_+g_m + \frac{2}{r}(1 - x^2 + rx)h_m \end{pmatrix}, \tag{A.5}$$

$\mathrm{w}(x) = 1/\sqrt{1 - x^2}$ is the weight function within the interval $(-1, 1)$, and the third component of $\tilde{\mathbf{u}}^{(2)}_m$ is replaced by rh_m if $k = 0$. The projection basis for the non-axisymmetric case is

$$\tilde{\mathbf{u}}^{(1)}_{knm}(r) = \mathrm{w}(x) \begin{pmatrix} \mathrm{i}nrg_m \\ rD_+(rg_m) + 2xr^2h_m \\ 0 \end{pmatrix}, \qquad \tilde{\mathbf{u}}^{(2)}_{knm}(r) = \mathrm{w}(x) \begin{pmatrix} 0 \\ \mathrm{i}kr^2h_m \\ -\mathrm{i}nrh_m \end{pmatrix}. \tag{A.6}$$

APPENDIX B

DOUBLE HOPF BIFURCATION WITH $SO(2) \times SO(2)$ SYMMETRY

The technique of Iooss & Adelmeyer (1998), which provides a clear and simple method to obtain normal forms, incorporating symmetry considerations, is now used for the double Hopf bifurcation with the $\mathcal{G} = SO(2) \times SO(2)$ symmetry group. In the codimension-1 Hopf bifurcation, the presence of $SO(2) \times SO(2)$ symmetry does not alter the generic normal form, and the same is true for the double Hopf bifurcation without resonance. However it is important to specify what the resonance conditions are, because as we shall see, $SO(2) \times SO(2)$ inhibits resonance. Resonance is only possible if both the temporal frequencies (imaginary parts of the eigenvalues *at the bifurcation point*, ω_1^0 and ω_2^0) and the spatial frequencies (azimuthal wave numbers, n_1 and n_2, and axial wave numbers, k_1 and k_2, at the bifurcation point) satisfy the resonance condition $\omega_2^0/\omega_1^0 = n_2/n_1 = k_2/k_1 = p/q$, where p and q are positive irreducible integers. We will follow closely the analysis of the double Hopf bifurcation with $SO(2)$ and with $SO(2) \times Z_2$ symmetries provided in former related works (Marques *et al.*, 2002; Lopez & Marques, 2004).

B.1 Derivation of the normal form

The normal form theorem says that the dynamical system in a neighborhood of the fixed point (steady, axisymmetric basic state) in the center manifold can be cast in the form

$$\dot{z}_i = \mathrm{i}\omega_i^0 z_i + S_i(z_1, z_2, \overline{z}_1, \overline{z}_2, \mu), \tag{B.1}$$

plus complex conjugate, for $i = 1, 2$. z_i are the amplitudes of the eigenvectors that bifurcate simultaneously, and μ are parameters. The functions S_i are second order in z for $\mu = 0$ and satisfy

$$S(\mathrm{e}^{tL_o^*} z) = \mathrm{e}^{tL_o^*} S(z), \tag{B.2}$$

$$S(R_\alpha z) = R_\alpha S(z), \tag{B.3}$$

$$S(T_a z) = T_a S(z), \tag{B.4}$$

where L_o is the linear part of the dynamical system at criticality and L_o^* is the corresponding adjoint operator. We have used vector notation $z = (z_1, z_2, \overline{z}_1, \overline{z}_2)$ and $S = (S_1, S_2, \overline{S}_1, \overline{S}_2)$ in order to keep the expressions compact. In this notation the matrices $\mathrm{e}^{tL_o^*}$, R_α and T_a are diagonal:

$$\mathrm{e}^{tL_o^*} = \mathrm{diag}(\mathrm{e}^{-\mathrm{i}\omega_1^0 t}, \mathrm{e}^{-\mathrm{i}\omega_2^0 t}, \mathrm{e}^{\mathrm{i}\omega_1^0 t}, \mathrm{e}^{\mathrm{i}\omega_2^0 t}), \tag{B.5}$$

$$R_\alpha = \mathrm{diag}(\mathrm{e}^{in_1\alpha}, \mathrm{e}^{in_2\alpha}, \mathrm{e}^{-in_1\alpha}, \mathrm{e}^{-in_2\alpha}), \tag{B.6}$$

$$T_a = \mathrm{diag}(\mathrm{e}^{\mathrm{i}k_1 a}, \mathrm{e}^{\mathrm{i}k_2 a}, \mathrm{e}^{-\mathrm{i}k_1 a}, \mathrm{e}^{-\mathrm{i}k_2 a}), \tag{B.7}$$

Equation (B.2) gives the simplest form of S attainable using the structure of the linear part L_o, and equations (B.3) and (B.4) give the additional constraints on S imposed by the symmetry group $SO(2) \times SO(2)$.

Let $z_1^{j_1} z_2^{j_2} \overline{z}_1^{l_1} \overline{z}_2^{l_2}$ be an admissible monomial in S_1; it must satisfy equations (B.2), (B.3) and (B.4), i.e.,

$$(j_1 - l_1 - 1)\omega_1^0 + (j_2 - l_2)\omega_2^0 = 0, \tag{B.8}$$

$$(j_1 - l_1 - 1)n_1 + (j_2 - l_2)n_2 = 0, \tag{B.9}$$

$$(j_1 - l_1 - 1)k_1 + (j_2 - l_2)k_2 = 0. \tag{B.10}$$

This system always admits the trivial solution $j_1 - l_1 - 1 = j_2 - l_2 = 0$. If there are no other solutions, we are in the the non-resonant case; the normal form is not modified by the presence of the symmetry group $SO(2) \times SO(2)$. The non-resonant normal form is

$$S_1 = z_1 Q_1, \quad S_2 = z_2 Q_2, \tag{B.11}$$

where $Q_i(|z_1|^2, |z_2|^2)$, which coincides with the generic case analyzed in Kuznetsov (2004).

In order that equations (B.8-B.10) have non-zero solutions, the resonant case, the condition

$$\frac{\omega_2^0}{\omega_1^0} = \frac{n_2}{n_1} = \frac{k_2}{k_1} \tag{B.12}$$

must be satisfied. The extra solutions are of the form

$$j_1 - l_1 - 1 = jp, \quad j_2 - l_2 = -jq, \quad j \in \mathbb{Z}, \tag{B.13}$$

where p/q is the irreducible form of the fraction n_2/n_1. Additional monomials

$$z_1(z_1^p \overline{z}_2^q)^j |z_1|^{2l_1} |z_2|^{2l_2}, \quad j \in \mathbb{Z},$$

appear in the normal form. As k_1 and k_2 are positive, p and q are also positive, and we obtain

$$S_1 = z_1 Q_{11} + \overline{z}_1^{p-1} z_2^q Q_{12}, \tag{B.14}$$

$$S_2 = z_2 Q_{21} + z_1^p \overline{z}_2^{q-1} Q_{22}, \tag{B.15}$$

where $Q_{ii}(|z_1|^2, |z_2|^2, z_1^p \overline{z}_2^q)$ and $Q_{ij}(|z_1|^2, |z_2|^2, \overline{z}_1^p z_2^q)$, $i \neq j$. This is in accordance with Theorem 4.2 in Golubitsky *et al.* (1988).

Resonance in the presence of $SO(2) \times SO(2)$ symmetry group is only possible if the resonance condition (B.12) is satisfied. The spatial (both azimuthal and axial) and temporal modes must satisfy the *same* resonance condition. Notice that this condition can *never* be satisfied if the two rotating waves do not precess in the same direction, or do not propagate in the same axial direction. When these simultaneous resonance conditions are satisfied, the normal form is given by (B.14–B.15).

Substituting (B.11) into (B.1), we obtain the normal form in the non-resonant case:

$$\dot{z}_i = z_i \big[\mathrm{i}\omega_i^0 + Q_i(|z_1|^2, |z_2|^2) \big]. \tag{B.16}$$

In terms of the moduli and phases of z_i, $z_i = r_i \mathrm{e}^{\mathrm{i}\phi_i}$, we have

$$\dot{r}_i = r_i Q_i^R(r_1^2, r_2^2), \tag{B.17}$$

$$\dot{\phi}_i = \omega_i^0 + Q_i^I(r_1^2, r_2^2), \tag{B.18}$$

where Q_i^R and Q_i^I are the real and imaginary parts of Q_i respectively. Up to fourth order in r_1 and r_2, and assuming that the coefficients of second order in Q_i^R are nonzero, the normal form can be written as (Kuznetsov, 2004):

$$\begin{aligned}
\dot{r}_1 &= r_1(\mu_1 + p_{11}r_1^2 + p_{12}r_2^2 + q_1 r_2^4), \\
\dot{r}_2 &= r_2(\mu_2 + p_{21}r_1^2 + p_{22}r_2^2 + q_2 r_1^4), \\
\dot{\phi}_1 &= \omega_1^0 + \psi_1(r_1, r_2, \mu_1, \mu_2), \\
\dot{\phi}_2 &= \omega_2^0 + \psi_2(r_1, r_2, \mu_1, \mu_2),
\end{aligned} \tag{B.19}$$

where we have introduced explicitly the normalized bifurcation parameters μ_1 and μ_2. The dynamics of the moduli r_1 and r_2 decouple from the phase dynamics, and we end up with an effective two-dimensional normal form for r_1 and r_2.

This effective normal form has four fixed points, that after introducing the phase dependence, become one fixed point, two periodic solutions, and a quasi-periodic solution. The stability and regions of existence of these solutions depend on the values of p_{ij} and q_i. There are eleven different scenarios, classified in two categories: *simple* ($p_{11}p_{22} > 0$) and *difficult* ($p_{11}p_{22} < 0$). For a specific problem, in order to determine the corresponding scenario, there are two options. One option is to compute the normal form coefficients p_{ij} and q_i using the eigenvectors at the bifurcation point, which is very complicated in the present case. The other option is to numerically compute a regime diagram in parameter space, delineating the regions of existence of the solutions, and determine their stability in a neighborhood of the double Hopf bifurcation point, and use this information to determine the corresponding scenario; this is the approach we have employed in Chapter 3. Figure 3.5 is the regime diagram we have obtained, by computing several solutions for different parameter values close to the double Hopf bifurcation point, and computing the Hopf curves using linear stability analysis. There is only one double Hopf scenario compatible with our results, and it is the type IV of the simple case (Kuznetsov, 2004).

B.2 Transition scenario

For the simple cases ($p_{11}p_{22} > 0$), the fourth order terms in (B.19) can be neglected. Introducing new variables, $\xi_1 = -p_{11}r_1^2$ and $\xi_2 = -p_{22}r_2^2$, we obtain

$$\begin{aligned} \dot{\xi}_1 &= 2\xi_1(\mu_1 - \xi_1 - \theta\xi_2), \\ \dot{\xi}_2 &= 2\xi_2(\mu_2 - \delta\xi_1 - \xi_2), \end{aligned} \tag{B.20}$$

where $\theta = p_{12}/p_{22}$ and $\delta = p_{21}/p_{11}$. For the double Hopf bifurcation investigated in §3.2, $\theta < 0$, $\delta < 0$, and $\theta\delta < 1$. The expressions for the normalized parameters $\mu_{1,2}$ as a function of the physical parameters Re_o and Re_i read

$$\mu_1 = Re_i - (1.949Re_o + 22.05), \tag{B.21}$$

$$\mu_2 = Re_i - (1.952Re_o + 21.75), \tag{B.22}$$

where $H_i = \{\mu_i = 0\}$, for $i = 1, 2$. This normal form admits up to four fixed points:

$$P_0 = (0,0), \quad P_1 = (\mu_1, 0), \quad P_2 = (0, \mu_2), \tag{B.23}$$

$$P_3 = \Big(\frac{\mu_1 - \theta\mu_2}{1-\theta\delta}, \frac{\mu_2 - \delta\mu_1}{1-\theta\delta}\Big). \tag{B.24}$$

Figure B.1 shows the parametric portrait in a neighborhood of a type IV double Hopf bifurcation point. Parameter space is divided into six regions, delimited by bifurcation curves. The number of solutions and their stability is different in each region. P_0 exists for all values of μ_1 and μ_2, and is stable for $\mu_1, \mu_2 < 0$. This corresponds to our basic state SPF. P_1 exists for $\mu_1 > 0$ and is stable for $\mu_2 < \delta\mu_1$ (below the N_1 curve in figure B.1, region 6); P_2 exists for $\mu_2 > 0$ and is stable for $\mu_2 < \theta^{-1}\mu_1$ (below the N_2 curve in figure B.1, region 2). By including the phase information, P_1 and P_2 are limit cycles, corresponding to Right and Left spiral waves, respectively. P_3 exists and is stable between N_1 and N_2 (regions 3, 4 and 5 in figure B.1). As both moduli are nonzero for P_3, by including the phase information, it is recognized as a quasi-periodic solution on

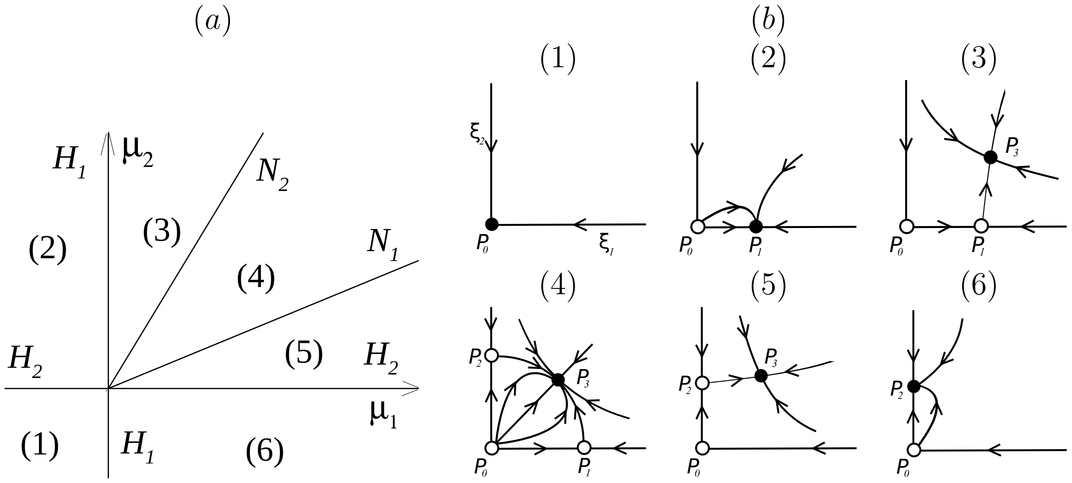

Figure B.1: *a*) Parametric portrait for a simple type IV double Hopf bifurcation. The curves H_1 and H_2 (coinciding with the axes $\mu_1 = 0$ and $\mu_2 = 0$, respectively), are the two Hopf bifurcation curves at which the limit cycles, P_1 and P_2, bifurcate supercritically from the basic state P_0. The curves N_1 and N_2 are Neimark-Sacker bifurcation curves at which the quasi-periodic mixed mode P_3 bifurcates. Phase portraits in each of the six regions indicated are shown in (*b*).

a two-torus, and in our case it corresponds to interpenetrating spirals. For P_1, P_2 and P_3, r_1 and r_2 are constant, and so they have constant angular frequencies:

$$\begin{aligned}\omega_1 = \dot{\phi}_1 = \omega_1^0 + \psi_1(r_1, r_2, \mu_1, \mu_2),\\ \omega_2 = \dot{\phi}_2 = \omega_2^0 + \psi_2(r_1, r_2, \mu_1, \mu_2).\end{aligned} \tag{B.25}$$

B.3 Symmetries of the solutions

In the non-resonant case, we have seen that the normal form is unaltered by the symmetry group $\mathcal{G}$. Nevertheless, the symmetries act on the bifurcating solutions in a well-determined fashion. From (B.6) and (B.7), we see that the action of $\mathcal{G}$ leaves the moduli (r_1, r_2) invariant, and $\mathcal{G}$ acts only on the phases (ϕ_1, ϕ_2). The action of $\mathcal{G}$ on the phases is:

$$R_\alpha \begin{pmatrix}\phi_1\\ \phi_2\end{pmatrix} = \begin{pmatrix}\phi_1 + n_1\alpha\\ \phi_2 + n_2\alpha\end{pmatrix}, \tag{B.26}$$

$$T_a \begin{pmatrix}\phi_1\\ \phi_2\end{pmatrix} = \begin{pmatrix}\phi_1 + k_1 a\\ \phi_2 + k_2 a\end{pmatrix}. \tag{B.27}$$

The basic state P_0 is a steady solution, $r_1 = r_2 = 0$, there are no phases, and hence it is $\mathcal{G}$-invariant. The solution P_1 has $r_2 = 0$ and so we only need to consider ϕ_1; as k_1 and

n_1 are different from zero, both symmetries are broken. The actions of R_α and T_a are equivalent to appropriate time translations τ_α and τ_a:

$$R_\alpha : \ \omega_1 \tau_\alpha = n_1 \alpha \ \rightarrow \ \tau_\alpha = n_1 \alpha / \omega_1, \tag{B.28}$$

$$T_a : \ \omega_1 \tau_a = k_1 a \ \rightarrow \ \tau_a = k_1 a / \omega_1. \tag{B.29}$$

R_α and T_a become spatio-temporal symmetries; time evolution is equivalent to a rotation around the axis and also to a translation along the axis. The limit cycle can be viewed simultaneously as a rotating wave (with precession frequency $\omega_p = -\omega_1/n_1$) and also as a traveling wave in the axial direction (with axial speed $c = -\omega_1/k_1$). In fact, P_1 retains a helical symmetry: $H_\alpha = R_\alpha T_{-n_1\alpha/k_1}$ leaves P_1 invariant; these helical symmetries generate a $SO(2)_H$ symmetry group, which is a subgroup of $\mathcal{G}$. The periodic solution P_1 is point-wise $SO(2)_H$-invariant, and *as a set* it is $\mathcal{G}$-invariant. For this reason we call this solution a spiral wave.

The solution P_2 has $r_1 = 0$ and so we only need to consider ϕ_2; exactly the same considerations as for P_1 show that P_2 is a rotating wave/traveling wave with helical symmetry $SO(2)$, i.e., a spiral wave; but the helical symmetries that keep P_2 invariant are different from the ones that leave P_1 invariant. P_2 is invariant to $H'_\alpha = R_\alpha T_{-n_2\alpha/k_2}$. The helical symmetries for P_1 and P_2 are the same only when there is *spatial resonance*: $n_2/n_1 = k_2/k_1$.

The time evolution of a P_3 solution is given by

$$\Phi_t \begin{pmatrix} \phi_1 \\ \phi_2 \end{pmatrix} = \begin{pmatrix} \phi_1 + \omega_1 t \\ \phi_2 + \omega_2 t \end{pmatrix}, \tag{B.30}$$

where Φ_t is the time evolution operator acting on the phases ϕ_1 and ϕ_2. If ω_2/ω_1 is rational P_3 is a periodic solution; it is the *temporal resonance* case. If not, it is a quasi-periodic solution. From P_3, the action of $\mathcal{G}$ generates a two torus (in the non-resonant case, where B.12 is not satisfied). The two-torus as a set is $\mathcal{G}$-invariant, but the individual P_3 solutions do not retain any point-wise spatial symmetry (except in the case of spatial resonance). Although P_3 is quasi-periodic, in an appropriate rotating (or traveling axially) frame of reference, it becomes a periodic solution; using (B.26), in an arbitrary reference frame rotating with angular velocity ω_r, the time evolution of P_3 is given by:

$$R_{-\omega_r t} \Phi_t \begin{pmatrix} \phi_1 \\ \phi_2 \end{pmatrix} = \begin{pmatrix} \phi_1 + (\omega_1 - n_1 \omega_r) t \\ \phi_2 + (\omega_2 - n_2 \omega_r) t \end{pmatrix}. \tag{B.31}$$

When ω_r is such that $(\omega_1 - n_1\omega_r)/(\omega_2 - n_2\omega_r)$ is rational, P_3 is *periodic* in the rotating reference frame. The two simplest choices are $\omega_r = \omega_i/n_i$, for $i = 1$ and 2. These choices are precisely the precession frequencies of the pure modes P_1 and P_2.

APPENDIX C

NEIMARK-SACKER BIFURCATION WITH $SO(2) \times O(2)^{ST}$ SYMMETRY

The analysis of the dynamics in a neighborhood of a periodic orbit in a continuous system is greatly simplified by the introduction of the Poincaré map. Generically, the Poincaré map is defined locally, in a neighborhood of the periodic orbit considered. However, in periodically forced systems like the present problem, there exists a global Poincaré map P, consisting of strobing the flow once every forcing period T_f. The base state, which is synchronous with the forcing, is a T_f-periodic orbit γ that becomes a fixed point of the discrete dynamical system P. The dynamics in a neighborhood of γ are completely determined once the normal form of the Poincaré map is known. The normal form is a low-dimensional low-order polynomial dynamical system, which is easy to obtain once the critical eigenvectors of γ and their symmetries are known. The critical eigenvectors span a low-dimensional linear subspace tangent to the center manifold. The amplitudes of these eigenvectors are the natural coordinates of the center manifold. In our problem, the base state γ depends only on (r, t) and the critical eigenvectors can be Fourier expanded in (θ, z). They are of the form $\mathbf{u}_1(r,t)\mathrm{e}^{\mathrm{i}(kz+n\theta)}$, $\mathbf{u}_2(r,t)\mathrm{e}^{\mathrm{i}(kz-n\theta)}$, with $n = 1$, and their complex conjugates. The first is a left-handed spiral and the second is a right-handed spiral (both are rotating waves in θ and traveling waves in z). Figure 4.6 shows the geometrical shapes of these spirals. The center manifold is four dimensional, and we use as coordinates the complex amplitudes $(A, B, \bar{A}, \bar{B})$ of the eigenvectors. The four eigenvectors bifurcate simultaneously because the space-time symmetry transforms A into B.

C.1 Spatial symmetries: generic dynamics

Let $x \to P(x) = L_P x + N_P(x)$ be the discrete dynamical system considered (the Poincaré map), restricted to the center manifold, with a fixed point that we assume to be the origin (after a convenient translation if necessary). The map is written as the sum of a linear part, L_P, and a nonlinear part, N_P. The eigenvalues of L_P are the critical eigenvalues, of modulus one. The symmetries of the original problem act on the amplitudes as a linear representation of the symmetry group of the problem, that commute with L_P. However, this applies only to purely spatial symmetries; space-time symmetries require a different treatment.

The normal form of the map, when the symmetries are purely spatial and do not involve time, satisfy the equations (Iooss & Adelmeyer, 1998)

$$N_P(L_P^\dagger x) = L_P^\dagger N_P(x), \qquad N_P(Gx) = GN_P(x),\ \forall G \in \mathcal{G}_0, \tag{C.1}$$

where $L_P^\dagger$ is the adjoint (conjugated and transposed) of L_P. The symmetry group of the spatial symmetries of the system under consideration is $\mathcal{G}_0 = SO(2) \times SO(2)$ and it is generated by rotations R_α about and translations T_a along the common axis of the cylinders. The actions of R_α and T_a on the amplitudes $x = (A, B, \bar{A}, \bar{B})$ are

$$R_\alpha = \operatorname{diag}(\mathrm{e}^{in\alpha}, \mathrm{e}^{-in\alpha}, \mathrm{e}^{-in\alpha}, \mathrm{e}^{in\alpha}), \quad T_a = \operatorname{diag}(\mathrm{e}^{ika}, \mathrm{e}^{ika}, \mathrm{e}^{-ika}, \mathrm{e}^{-ika}). \tag{C.2}$$

As L_P commutes with R_α and T_a, it must be diagonal. Let $\mathrm{e}^{\mathrm{i}\beta_1}$ be the eigenvalue corresponding to A. As the space-time symmetry S transforms A into B, both have the same eigenvalue. Therefore, L_P must be of the form

$$L_P = \operatorname{diag}(\mathrm{e}^{\mathrm{i}\beta_1}, \mathrm{e}^{\mathrm{i}\beta_1}, \mathrm{e}^{-\mathrm{i}\beta_1}, \mathrm{e}^{-\mathrm{i}\beta_1}), \tag{C.3}$$

where β_1 is related to the spiral frequency ω_s as $\beta_1 = \omega_s T_f = 2\pi\,\omega_s/\omega_f$. The normal form for the Poincaré map is

$$P : \begin{cases} A \to \mathrm{e}^{\mathrm{i}\beta_1} A + N_1(A, B, \bar{A}, \bar{B}), \\ B \to \mathrm{e}^{\mathrm{i}\beta_1} B + N_2(A, B, \bar{A}, \bar{B}), \end{cases} \tag{C.4}$$

plus complex conjugates. Let $A^p B^q \bar{A}^r \bar{B}^j$ be a monomial in N_1. The first equation in (C.1) is a particular case of the second, because L_P coincides with an axial translation $a = \beta_1/k$ ($L_P = T_{\beta_1/k}$). The second equation in (C.1) results in

$$\left.\begin{aligned} \mathrm{e}^{in\alpha(p-q-r+j)} &= \mathrm{e}^{in\alpha} \\ \mathrm{e}^{ika(p+q-r-j)} &= \mathrm{e}^{ika} \end{aligned}\right\} \;\Rightarrow\; \left.\begin{aligned} p-q-r+j &= 1 \\ p+q-r-j &= 1 \end{aligned}\right\} \;\Rightarrow\; p = r+1,\ q = j, \tag{C.5}$$

so $N_1(A, B, \bar{A}, \bar{B}) = AQ_1(|A|^2, |B|^2)$, and analogously for N_2. Equation (C.4) reduces to

$$P : \begin{cases} A \to \mathrm{e}^{\mathrm{i}\beta_1} A\big(1 + Q_1(|A|^2, |B|^2)\big), \\ B \to \mathrm{e}^{\mathrm{i}\beta_1} B\big(1 + Q_2(|A|^2, |B|^2)\big), \end{cases} \tag{C.6}$$

where a factor $\mathrm{e}^{-\mathrm{i}\beta_1}$ has been included in Q_i for convenience. Some important consequences of this normal form are worth noting. First of all, there are no resonant terms, therefore the normal form is the same regardless of whether $\beta_1/2\pi$ is rational or irrational. In particular, there is no distinction between strong resonances ($\beta_1/2\pi = \ell/m$, with $m = 1$, 2, 3 or 4), weak resonances ($m > 4$), or no resonances at all ($\beta_1/2\pi \notin \mathbb{Q}$). This is a consequence of the rotational and translational symmetry of the system, i.e.

the spatial symmetry group $\mathcal{G}_0 = SO(2) \times SO(2)$. Another important consequence is the absence of frequency-locking phenomena. Generically, frequency-locking takes place when resonant terms (different from $A|A|^2$ and $A|B|^2$ in N_1, and analogously in N_2) couple the modulus and phase dynamics of A and B. By introducing $A = r_1 \mathrm{e}^{\mathrm{i}\phi_1}$ and $B = r_2 \mathrm{e}^{\mathrm{i}\phi_2}$, the normal form (C.6) can be written as

$$P: \begin{cases} r_1 \to r_1\big(1 + Q_{1,1}(r_1^2, r_2^2)\big) \\ r_2 \to r_2\big(1 + Q_{2,2}(r_1^2, r_2^2)\big) \end{cases} \qquad \begin{cases} \phi_1 \to \phi_1 + \beta_1 + Q_{1,2}(r_1^2, r_2^2) \\ \phi_2 \to \phi_2 + \beta_1 + Q_{2,1}(r_1^2, r_2^2) \end{cases} \tag{C.7}$$

and the modulus dynamics (r_1 and r_2) decouples from the phase dynamics (ϕ_1 and ϕ_2). The decoupling is the cause of the suppression of the frequency-locking phenomena.

This frequency-locking suppression is very similar to the result of Rand (1982, Theorem 3 and Remark) that Hopf bifurcations from rotating waves do not manifest frequency-locking, due to the rotational symmetry. In our case, the base state is not a rotating wave, but it is independent of the azimuthal and axial coordinates, i.e. it is a $SO(2) \times SO(2)$ symmetric periodic orbit. The breaking of these symmetries results in modulated spiral waves that do not manifest frequency-locking. There has been a great deal of work concerning bifurcations from periodic orbits generalizing Rand's original work (Krupa, 1990; Lamb *et al.*, 2003), from which our result, complementary to Rand's, can be obtained. We have kept the result in the appendix for completeness.

C.2 Space-time symmetry S

Now consider the implications of the space-time symmetry S. The square of S is the identity on the base state of the system, but acting on an arbitrary solution results in the global Poincaré map P: the two axial reflections K_z cancel each other, and the total advance in time is the period of the forcing T_f. The fact that the Poincaré map is a square, $P = S^2$, has important implications on the dynamics (see for example Swift & Wiesenfeld, 1984, when the critical eigenvalues are simple). A powerful and simple way to take into account the space-time symmetry is to analyze the normal form of S and recover the Poincaré map normal form by squaring it. This has been done, for example, in Marques, Lopez & Blackburn (2004) for a system with spatial symmetry $O(2)$ and spatio-temporal symmetry Z_2. The analysis in that case was facilitated by the fact that the spatio-temporal symmetry commuted with the spatial symmetries, and the conditions to be satisfied by the normal form of S were the same as in (C.1), just replacing L_P by L_S. But in the present problem, S does not commute with the axial translations T_a (in fact $ST_a = T_{-a}S$), so we need to establish what are the conditions to be satisfied by the normal form of S. The condition $N(Gx) = GN(x)$ must be changed to a more general condition that includes the case of non-commutativity of the spatial symmetries with S, and in particular with their linear part L_S. The discrete dynamical system S is a map $S : x \to F(x)$, but now F is not $\mathcal{G}_0$-equivariant (i.e. $F(Gx) \neq GF(x)$, $\forall G \in \mathcal{G}_0$). This is because there exist elements of $\mathcal{G}_0$ that do not commute with S (e.g. the axial translations T_a). Inspired by, and following the work of Lamb & Melbourne (1999) (and references therein), we say that F satisfies a *twisted equivariance condition* of the form

$$F(Gx) = \psi(G)F(x), \quad \forall G \in \mathcal{G}_0, \tag{C.8}$$

where ψ is an automorphism of $\mathcal{G}_0$. This automorphism is fixed by the same twisted equivariance condition on the linear part of S, $L_S(Gx) = \psi(G)L_S(x)$, i.e. $\psi(G) = L_S G L_S^{-1}$. Summarizing, if the normal form of S is $x \to S(x) = L_S x + N(x)$, the conditions on N are of the form

$$N(L_S^\dagger x) = L_S^\dagger N(x), \; N(Gx) = \psi(G)N(x), \; \forall G \in \mathcal{G}_0, \text{ where } \psi(G) = L_S G L_S^{-1}. \tag{C.9}$$

Notice that when L_S commutes with $\mathcal{G}$ (as in Marques *et al.*, 2004), the inner automorphism becomes the identity, and we recover the ordinary equivariant condition (C.1). What is the action of L_S on the center manifold? The center manifolds and eigenvectors of P and their square-root S are the same, and the eigenvalues of P are the eigenvalues of S squared. However, there is some freedom in the form of L_S, because the eigenvalues are of multiplicity two (e.g. the two-dimensional eigenspace associated to the eigenvalue $\mathrm{e}^{\mathrm{i}\beta_1}$ has A and B as coordinates). This freedom is fixed since L_S must transform A into B, because the axial reflection K_z transforms the left-handed spiral A into the right-handed spiral B (modulus the time translation $T/2$). The action of L_S on the complex amplitudes $(A, B, \bar{A}, \bar{B})$ is

$$L_S = \begin{pmatrix} 0 & \mathrm{e}^{\mathrm{i}\beta_1/2} & 0 & 0 \\ \mathrm{e}^{\mathrm{i}\beta_1/2} & 0 & 0 & 0 \\ 0 & 0 & 0 & \mathrm{e}^{-\mathrm{i}\beta_1/2} \\ 0 & 0 & \mathrm{e}^{-\mathrm{i}\beta_1/2} & 0 \end{pmatrix} \tag{C.10}$$

and the actions of R_α and T_a are unchanged, given by (C.2). The automorphism ψ can be explicitly computed: $\psi(R_\alpha) = R_\alpha$, $\psi(T_a) = T_{-a}$, reflecting the fact that S commutes with R_α, but $ST_a = T_{-a}S$. ψ is an involution, $\psi^2 = Id$, reflecting the fact that $S^2 = P$. Having explicitly obtained the actions of L_S, ψ and $\mathcal{G}_0$, we can work out the conditions

(C.9). The normal form for the space-time map S is of the form

$$S : \begin{cases} A \to \mathrm{e}^{\mathrm{i}\beta_1/2} B + N_3(A, B, \bar{A}, \bar{B}), \\ B \to \mathrm{e}^{\mathrm{i}\beta_1/2} A + N_4(A, B, \bar{A}, \bar{B}). \end{cases} \tag{C.11}$$

Let $A^p B^q \bar{A}^r \bar{B}^j$ be a monomial in N_3. Following the same lines as in the purely spatial symmetries case, we obtain

$$S : \begin{cases} A \to \mathrm{e}^{\mathrm{i}\beta_1/2} B\big(1 + Q(|B|^2, |A|^2)\big), \\ B \to \mathrm{e}^{\mathrm{i}\beta_1/2} A\big(1 + Q(|A|^2, |B|^2)\big). \end{cases} \tag{C.12}$$

Instead of two arbitrary functions Q_3 and Q_4, there is only one, Q, because L_S transforms A into B. By squaring the map, the normal form of the Poincaré map P (C.6) is obtained, but thanks to the use of the space-time symmetry S, we obtain

$$Q_1(|A|^2, |B|^2) = Q_2(|B|^2, |A|^2) = \tilde{Q}(|A|^2, |B|^2), \tag{C.13}$$

where $\tilde{Q}$ is a complex-coefficient polynomial; this is the constraint imposed by the space-time symmetry S on the normal form of the Poincaré map. The relationship between Q and $\tilde{Q}$ is easy to obtain, but convoluted[1]. In terms of the moduli and phases of A and B, the normal form of the Poincaré map (C.7) reduces to

$$P : \begin{cases} r_1 \to r_1\big(1 + Q_m(r_1^2, r_2^2)\big) \\ r_2 \to r_2\big(1 + Q_m(r_2^2, r_1^2)\big) \end{cases} \qquad \begin{cases} \phi_1 \to \phi_1 + \beta_1 + Q_p(r_1^2, r_2^2) \\ \phi_2 \to \phi_2 + \beta_1 + Q_p(r_2^2, r_1^2) \end{cases} \tag{C.14}$$

where the polynomials Q_m and Q_p have real coefficients: $1 + \tilde{Q} = (1 + Q_m)\exp(\mathrm{i}Q_p)$. The moduli dynamics decouples from the phase dynamics, and we end up with a two-dimensional reduced normal form, the first two equations in (C.14). As the polynomial Q_m is the same in r_1 and r_2, the fixed points of the reduced normal form are of the form (r, r), including $(0, 0)$ which is the base state, or they come in symmetric pairs (r, r') and (r', r). In the complete problem, the fixed points of the form $(0, r)$, $(r, 0)$ and (r, r), $r \neq 0$, are quasiperiodic solutions with two frequencies, and the fixed points of the form (r, r'), $r \neq r' \neq 0$, correspond to three-frequency solutions.

C.3 Bifurcation scenarios

In order to explore the dynamics in a neighborhood of the bifurcation, the normal form for S (C.12) is truncated up to fourth-order terms, and written in terms of the moduli

---

[1] The precise expression is $\tilde{Q}(x, y) = \{1 + Q(x, y)\}\{1 + Q(x|1 + Q(x, y)|^2, y|1 + Q(y, x)|^2)\} - 1$

and phases of A and B:

$$S: \begin{cases} r_1 \to r_2(1+\mu - ar_2^2 - br_1^2) \\ r_2 \to r_1(1+\mu - ar_1^2 - br_2^2) \end{cases} \qquad \begin{cases} \phi_1 \to \phi_2 + \beta_1/2 + \nu + cr_2^2 + dr_1^2 \\ \phi_2 \to \phi_1 + \beta_1/2 + \nu + cr_1^2 + dr_2^2 \end{cases} \tag{C.15}$$

It is worth noting that the symmetry group of this normal form is $Z_2 \times Z_2$. One of the symmetries corresponds to the exchange between r_1 and r_2 ($r_1 \leftrightarrow r_2$), and comes from the space-time symmetry S. The other Z_2 symmetry ($r \leftrightarrow -r$) comes from the use of polar coordinates. The bifurcation is of codimension two (two independent parameters μ and ν), but the reduced system is of codimension one since the parameter ν only affects the phase dynamics. The only fixed points of the reduced planar system (r_1, r_2) in a neighborhood of the origin are of the form (r, r), and there are two of them:

$$p_0 = (0,0), \quad p_3 = \left(\sqrt{\frac{\mu}{a+b}}, \sqrt{\frac{\mu}{a+b}}\right). \tag{C.16}$$

The corresponding eigenvalues (in the reduced system for S) are

$$p_0: \quad \lambda_1 = 1+\mu, \qquad \lambda_2 = -1-\mu, \tag{C.17}$$

$$p_3: \quad \lambda_1 = 1-2\mu, \quad \lambda_2 = -1 + 2\,\frac{a-b}{a+b}\,\mu. \tag{C.18}$$

The eigenvalues of the corresponding reduced system for P are the same squared. The base state is p_0, it exists for any μ value, it is stable for $\mu < 0$ and unstable for $\mu > 0$. p_3 exists only for $\mu/(a+b) > 0$, and is stable for $a - b > 0$ and $\mu > 0$. Both p_0 and p_3 are invariant under the space-time symmetry S. The bifurcation is supercritical for $a + b > 0$ and subcritical for $a + b < 0$. The bifurcated state p_3 is a linear combination with the same weight ($|A| = |B|$) of the left-handed and right-handed spirals, which travel in opposite axial directions. p_3 therefore corresponds to a modulated standing wave, MSW.

We can also look for periodic orbits of S, of period two, and these are fixed points of the Poincaré map P. As $P = S^2$, from (C.15) we obtain

$$P: \begin{cases} r_1 \to r_1(1+2\mu - 2ar_1^2 - 2br_2^2) \\ r_2 \to r_2(1+2\mu - 2ar_2^2 - 2br_1^2) \end{cases} \qquad \begin{cases} \phi_1 \to \phi_1 + \beta_1 + 2\nu + 2cr_1^2 + 2dr_2^2 \\ \phi_2 \to \phi_2 + \beta_1 + 2\nu + 2cr_2^2 + 2dr_1^2. \end{cases} \tag{C.19}$$

The fixed points of the reduced planar system, of the form (r, r) are the same p_0 and p_3 already obtained. But there is a pair of new fixed points of P:

$$p_1 = (\sqrt{\mu/a}, 0), \quad p_2 = (0, \sqrt{\mu/a}), \tag{C.20}$$

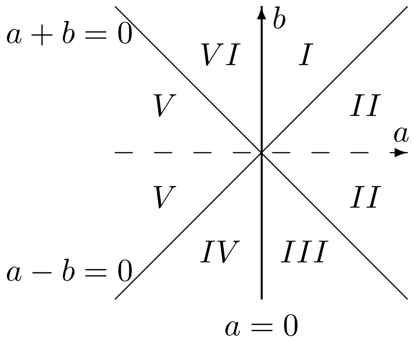

Figure C.1: Regions in parameter space where different dynamics exist. The corresponding phase portraits are shown in figure C.2.

that exist for $\mu/a > 0$. The fixed points p_1 and p_2 correspond to periodic orbits of period two of the space-time symmetry S that transforms one into the other: $Sp_1 = p_2$, $Sp_2 = p_1$, as can be checked directly in (C.15). p_1 is a left-handed spiral, a traveling wave in the axial direction. p_2 is a right-handed spiral, traversing in the opposite axial direction. Both are modulated traveling wave solutions, MTW, that break the space-time symmetry. They have the same eigenvalues (in the reduced system for P), which are

$$p_1,\ p_2: \quad \lambda_1 = 1 - 4\mu, \quad \lambda_2 = 1 + 2\frac{a-b}{a}\mu, \tag{C.21}$$

and they are stable if $\mu > 0$ and $a < b$.

When $a = 0$ or $a + b = 0$ or $a - b = 0$, there are degeneracies between the fixed points p_i and/or their eigenvalues, so we will assume $a \neq 0$ and $a + b \neq 0$ and $a - b \neq 0$. The bifurcation has six different scenarios, corresponding to the six regions in parameter space delimited by the curves $a = 0$, $a + b = 0$ and $a - b = 0$, as illustrated in figure C.1. The phase portraits for the six scenarios are schematically drawn in figure C.2. The scenarios and phase portraits in figures C.1 and C.2 occur in a number of contexts involving symmetry breaking Hopf bifurcations (see Crawford & Knobloch, 1991, and references there in). As the bifurcation is of codimension one and takes place for $\mu = 0$, we have plotted the phase portraits for the reduced system (r_1, r_2) before and after the bifurcation.

In the first (I) and second (II) scenarios, the two modulated traveling waves and the modulated standing wave bifurcate simultaneously and supercritically from the base state, that becomes unstable. In the first scenario the MTW are stable and the MSW is unstable. In the second scenario it is the opposite. In the (IV) and (V) scenarios, the two modulated traveling waves and the modulated standing wave bifurcate simultaneously

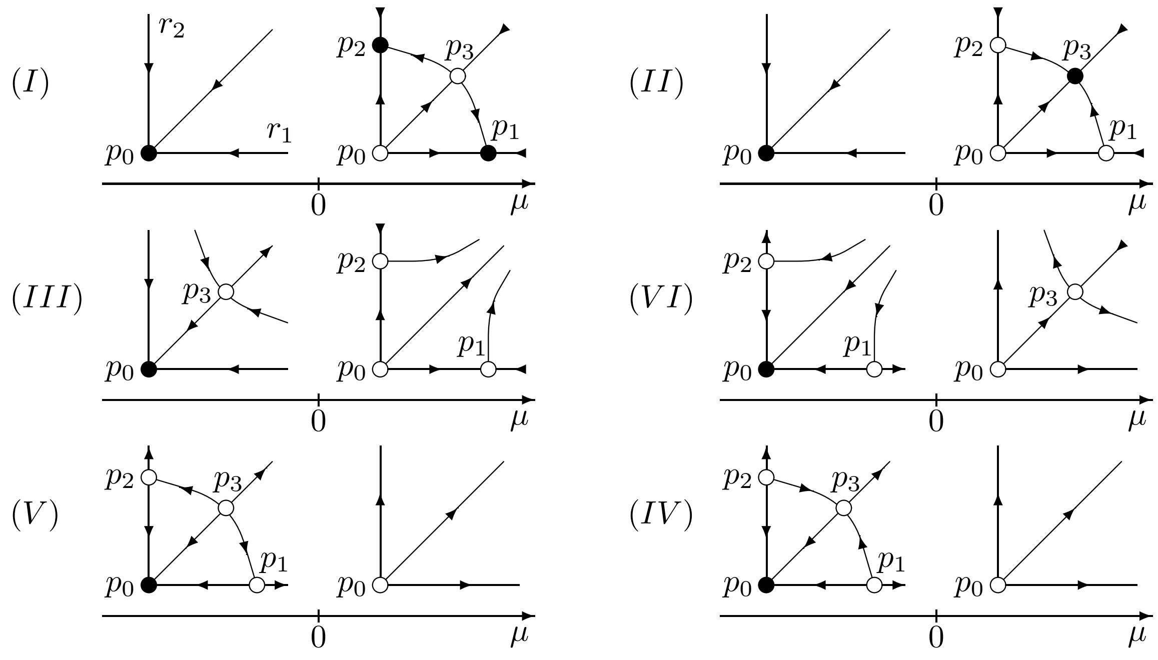

Figure C.2: Phase portraits corresponding to the six bifurcation scenarios in figure C.1. Phase portraits for the reduced system (r_1, r_2) have been plotted before $(\mu < 0)$ and after $(\mu > 0)$ the bifurcation.

and subcritically from the base state, that becomes unstable. The traveling and standing waves are always unstable, so after the bifurcation $(\mu > 0)$ there are no stable solutions close to the origin, and the system evolves far away from the base state. The only difference between both scenarios is in the number of unstable directions of the standing wave, one and two in scenarios (IV) and (V) respectively. In the (III) scenario, the base state becomes unstable by colliding with the unstable MSW, and after the bifurcation the two MTW emerge but are unstable, and the system evolves far away from the base state, as there are no stable states close to the origin. Finally, in the (VI) scenario, the base state becomes unstable by colliding with the two unstable MTW, and after the bifurcation the MSW emerge but are unstable, and the system evolves far away from the base state as before. In the system under consideration, and for the parameter values analyzed, the second scenario (II) takes place.

C.4 Neimark-Sacker bifurcation with $SO(2)$ symmetry

The M1 spiral waves perturbation velocity field depends on (θ, z) only in the combination $\omega_s t + kz + n\theta$. After the bifurcation, an additional dependence on $\omega_w t + n_w\theta$

appears, therefore the critical eigenvector is of the form $\mathbf{f}(r, t, \omega_s t + kz + n\theta)\mathrm{e}^{\mathrm{i}(\omega_w t + n_w\theta)}$. In fact we do not have a pair of complex-conjugate eigenvectors, but rather an infinite family. This is because the action of R_α does not leave a M1 spiral wave invariant (the bifurcation to M1 has broken the rotational symmetry), but changes its phase in the azimuthal direction. The Poincaré map (strobing with the forcing period T_f) has a pair of complex-conjugate eigenvectors of modulus one at the bifurcation point, given by $\mathrm{e}^{\pm\mathrm{i}\beta_2}$ with $\beta_2 = \omega_w T_f = 2\pi\,\omega_w/\omega_f$. It also has a center direction corresponding to the continuous symmetry broken at the bifurcation to M1, so the center manifold is three-dimensional. Nevertheless, as M1 is a relative periodic orbit, the dynamics in this third direction decouples from the dynamics corresponding to the pair of complex-conjugate eigenvectors (see Wulff *et al.*, 2001), so the bifurcation can be analyzed as being effectively two-dimensional, spanned by the mentioned eigenvector and its complex conjugate, and can be parameterized by a complex amplitude A. The normal form $x \to P(x) = L_P x + N_P(x)$, with $x = (A, \bar{A})$ must satisfy (C.1), where the symmetry group is now $\mathcal{G}_0 = SO(2)$, generated by the helical motion $H_\alpha = R_\alpha T_{-n\alpha/k}$, and no spatio-temporal symmetries exist. The action of L_P and H_α on $(A, \bar{A})$ is easy to obtain from the (θ, z) dependence of the eigenvectors, and is

$$L_P = \mathrm{diag}(\mathrm{e}^{\mathrm{i}\beta_2}, \mathrm{e}^{-\mathrm{i}\beta_2}), \quad H_\alpha = \mathrm{diag}(\mathrm{e}^{\mathrm{i}n_w\alpha}, \mathrm{e}^{-\mathrm{i}n_w\alpha}). \tag{C.22}$$

$L_P = H_{\beta_2/n_w}$, showing that the bifurcated solution is a modulated spiral wave: advancing a forcing period is equivalent to a helical motion. The conditions (C.1) on the normal form result in $N_P(A, \bar{A}) = A\tilde{Q}(|A|^2)$ and the normal form is

$$P : A \to \mathrm{e}^{\mathrm{i}\beta_2} A\big(1 + Q(|A|^2)\big), \tag{C.23}$$

where a factor $\mathrm{e}^{-\mathrm{i}\beta_2}$ has been included in Q for convenience. This is the normal form of a non-resonant Neimark-Sacker bifurcation (Kuznetsov, 2004), the absence of resonant terms being due to the presence of the helical symmetry group $SO(2)$, irrespective of $\beta_2/2\pi = \omega_w/\omega_f$ being rational or irrational. The bifurcated solution retains a discrete helical symmetry: from (C.22), $H_{2\pi/n_w}$ is the identity on the bifurcated solutions, and their symmetry group is discrete, $\mathbb{Z}_{ln_w}$, generated by the helical motion $H_{2\pi/n_w}$. Notice that in this bifurcation the axial periodicity is not altered: $H_{2\pi/n_w}^{n_w} = T_\lambda$, an axial translation of the wavelength of the spiral wave.

APPENDIX D
DOUBLE PITCHFORK-OF-REVOLUTION WITH $Z_2^{ST} \times O(2)$ SYMMETRY

In chapter 5, we found that the dynamics of the Taylor–Couette system with modulations about a zero-mean is organized about a codimension-two point where the periodic base state bifurcates simultaneously to modes A and B. In the axisymmetric subspcace, the symmetry goup of the basic state is $\mathcal{G} = Z_2^{ST} \times O(2)$. Marques *et al.* (2004) obtained the possible bifurcations and corresponding normal forms in $\mathcal{G}$-symmetric systems. Moreover, they analyzed in detail the codimension-one bifurcations and illustrated them with examples in periodically driven cavity flow. Since mode A breaks the space-time symmetry S, and mode B preserves it, the normal form for the half-period-flip map $\mathcal{H}$, up to third order, is (Marques *et al.*, 2004)

$$\mathcal{H}: \begin{cases} A \mapsto A(-1+\mu+a|A|^2+b|B|^2) \\ B \mapsto B(+1+\nu+c|A|^2+d|B|^2), \end{cases} \tag{D.1}$$

where A and B are the complex amplitudes corresponding to the bifurcating modes A and B respectively. Since all the coefficients (μ, ν, a, b, c, d) are real, the dynamics of the phases of A and B are trivial; writing A and B in terms of their moduli and phases, $A = r_1 \mathrm{e}^{\mathrm{i}\phi_1}$ and $B = r_2 \mathrm{e}^{\mathrm{i}\phi_2}$, we obtain

$$\mathcal{H}: \begin{cases} r_1 \mapsto r_1(-1+\mu+ar_1^2+br_2^2) \\ r_2 \mapsto r_2(+1+\nu+cr_1^2+dr_2^2), \end{cases} \qquad \begin{cases} \phi_1 \mapsto \phi_1 \\ \phi_2 \mapsto \phi_2 \end{cases}, \tag{D.2}$$

and the phases ϕ_1 and ϕ_2 remain constant. Assuming that a and d are not zero (they are negative in our problem), re-scaling r_1 and r_2 gives

$$\mathcal{H}: \begin{cases} r_1 \mapsto r_1(-1+\mu-r_1^2-\zeta r_2^2) \\ r_2 \mapsto r_2(+1+\nu-\delta r_1^2-r_2^2), \end{cases} \tag{D.3}$$

with two unfolding parameters μ and ν, and two constants ζ and δ whose exact values depend on the problem considered. In the neighborhood of the codimension-two point the two bifurcation parameters μ and ν are linearly related to Re_a and ω by

$$\begin{aligned} \mu &= Re_a - 10.56\,\omega - 77.86, \\ \nu &= Re_a + 0.8992\,\omega - 122.96, \end{aligned} \tag{D.4}$$

and the two constants are $\zeta = 1.9670$ and $\delta = 1.9022$. These values have been obtained from the numerical data in figure 5.10. The action of $\mathcal{G}_s = O(2) \times Z_2$ leaves the amplitudes r_1 and r_2 invariant, but acts non-trivially on the phases (Marques *et al.*, 2004):

$$\begin{aligned} T_a(\phi_1, \phi_2) &= (\phi_1 + k_1 a, \phi_2 + k_2 a), \\ K_z(\phi_1, \phi_2) &= (-\phi_1, -\phi_2), \\ H(\phi_1, \phi_2) &= (\phi_1 + \pi, \phi_2), \end{aligned} \tag{D.5}$$

where k_1 and k_2 are the critical axial wavenumbers of modes A and B respectively. These actions are easy to obtain by considering that the bifurcating eigenvectors are of the form $A\mathrm{e}^{\mathrm{i}kz}\mathbf{v}(r, t)$ because the base state mC is independent of (θ, z). We assume that k_1/k_2 is irrational (non-resonant case), i.e. the critical wavenumbers of the two modes are not in a rational ratio, as is the case in our problem.

In order to describe the dynamics associated to the normal form (D.3), it is very convenient to obtain the fixed points of the Poincaré map $\mathcal{P} = \mathcal{H}^2$. Up to third order,

$$\mathcal{P} : \begin{cases} r_1 \mapsto r_1(1 + 2\mu - 2r_1^2 - 2\zeta r_2^2) \\ r_2 \mapsto r_2(1 + 2\nu - 2\delta r_1^2 - 2r_2^2). \end{cases} \tag{D.6}$$

The Poincaré map may have up to four different fixed points, depending on the values of ζ and δ, and on the region in parameter space (μ, ν) considered. The fixed points in phase space (r_1, r_2) are:

$$\mathrm{mC} = (0, 0), \quad \mathrm{A} = (\sqrt{\mu}, 0), \quad \mathrm{B} = (0, \sqrt{\nu}\,), \quad \mathrm{AB} = \left(\sqrt{\frac{\zeta\nu - \mu}{\zeta\delta - 1}}, \sqrt{\frac{\delta\mu - \nu}{\zeta\delta - 1}} \right), \tag{D.7}$$

and they have been labeled according to the solutions of the present problem.

The modulus dynamics (D.6) are identical to the modulus dynamics of the double-Hopf bifurcation (dH) of equation (B.19) in Appendix B. Therefore, the results Kuznetsov (2004) apply to the present case. In particular, the bifurcation scenario of figure 5.10 is the analogous of type I of the “simple” case of dH, for which $\zeta > 0$, $\delta > 0$ and $\theta\delta > 1$ (Kuznetsov, 2004). However, the interpretation of the dynamics associated to the fixed points (D.7) changes. The Hopf bifurcations in dB become pitchforks-of-revolution bifurcations (since the phases remain constant). A and B are limit cycles in dH, and here they are fixed points; and AB, a quasiperiodic solution in dH, is also a fixed point here. As the phase dynamics here refers to translations in z while in the dH it is associated with time, A and B are periodic solutions in z, while AB is quasiperiodic in space. Finally, in dH one is dealing with an ODE system, so the curves in the phase portraits are orbits in (r_1, r_2) phase space; here we are dealing with maps ($\mathcal{P}$ and $\mathcal{H}$) and so the curves in the phase portraits are invariant manifolds, containing an infinite number of discrete orbits.

BIBLIOGRAPHY

Ali, M. E. & Weidman, P. D. 1993 On the linear stability of cellular spiral Couette flow. *Phys. Fluids A* **5**, 1188–1200.

Andereck, C. D., Liu, S. S. & Swinney, H. L. 1986 Flow regimes in a circular Couette system with independently rotating cylinders. *J. Fluid Mech.* **164**, 155–183.

Arnold, V. I., Afrajmovich, V. S., Il'yashenko, Y. S. & Shil'nikov, L. P. 1999 *Bifurcation Theory and Catastrophe Theory*. Springer.

Avila, M., Belisle, M. J., Lopez, J. M., Marques, F. & Saric, W. S. 2008 Mode competition in modulated Taylor–Couette flow. *J. Fluid Mech.* **601**, 381–406.

Avila, M., Marques, F., Lopez, J. M. & Meseguer, A. 2007 Stability control and catastrophic transition in a forced Taylor-Couette system. *J. Fluid Mech.* **590**, 471–496.

Avila, M., Meseguer, A. & Marques, F. 2006 Double Hopf bifurcation in corotating spiral Poiseuille flow. *Phys. Fluids* **18**, 064101.

Babcock, K. L., Ahlers, G. & Cannell, D. S. 1994 Noise amplification in open Taylor-Couette flow. *Phys. Rev. E* **50** (5), 3670–3691.

Barenghi, C. F. & Jones, C. A. 1989 Modulated Taylor-Couette flow. *J. Fluid Mech.* **208**, 127–160.

Barkley, D. & Henderson, R. D. 1996 Three–dimensional Floquet stability analysis of the wake of a circular cylinder. *J. Fluid Mech.* **322**, 215–241.

Barkley, D., Tuckerman, L. S. & Golubitsky, M. 2000 Bifurcation theory for three-dimensional flow in the wake of a circular cylinder. *Phys. Rev. E* **61**, 5247–5252.

Belisle, M. J. 2007 Experiments on mode competition in temporally-modulated Taylor–Couette flow. Master's thesis, Arizona State University, Tempe, Arizona.

Benjamin, T. B. 1978 Bifurcation phenomena in steady flows of a viscous fluid. i. theory, ii. experiments. *Proc. Roy. Soc. Lond. A* **359**, 1–26,27–43.

Benjamin, T. B. & Mullin, T. 1981 Anomalous modes in the Taylor experiment. *Proc. Roy. Soc. Lond. A* **377**, 221–249.

Blackburn, H. M., Marques, F. & Lopez, J. M. 2005 Symmetry breaking of two-dimensional time-periodic wakes. *J. Fluid Mech.* **522**, 395–411.

Brandstäter, A. & Swinney, H. L. 1987 Strange attractors in weakly turbulent Couette-Taylor flow. *Phys. Rev. A* **35**, 2207–2220.

Canuto, C., Hussaini, M. Y., Quarteroni, A. & Zang, T. A. 2006 *Spectral Methods*, *Scientific Computation*, vol. 1. Berlin: Springer–Verlag.

Carmi, S. & Tustaniwskyj, J. I. 1981 Stability of modulated finite-gap cylindrical Couette flow: linear theory. *J. Fluid Mech.* **108**, 19–42.

Chossat, P. & Iooss, G. 1994 *The Couette-Taylor problem*, *Applied Mathematical Sciences*, vol. 102. Springer–Verlag.

Chossat, P. & Lauterbach, R. 2000 *Methods in Equivariant Bifurcations and Dynamical Systems*. World Scientific.

Chung, K. C. & Astill, K. N. 1977 Hydrodynamic instability of viscous flow between rotating coaxial cylinders with fully developed axial flow. *J. Fluid Mech.* **81**, 641–655.

Cliffe, K. A. 1983 Numerical calculations of two-cell and single-cell Taylor flows. *J. Fluid Mech.* **135**, 219–233.

Cole, J. A. 1976 Taylor-vortex instability and annulus-length effects. *J. Fluid Mech.* **75**, 1–15.

Coles, D. 1965 Transition in circular Couette flow. *J. Fluid Mech.* **21**, 385–425.

Cotrell, D. L. & Pearlstein, A. J. 2004 The connection between centrifugal instability and tollmien schlichting-like instability for spiral poiseuille flow. *J. Fluid Mech.* **509**, 331–351.

Crawford, J. D. & Knobloch, E. 1991 Symmetry and symmetry-breaking bifurcations in fluid dynamics. *Ann. Rev. Fluid Mech.* **23**, 341–387.

Dominguez-Lerma, M. A., Cannell, D. S. & Ahlers, G. 1986 Eckhaus boundary and wave-number selection in rotating Couette-Taylor flow. *Phys. Rev. A* **34**, 4956–4970.

Donnelly, R. J. 1964 Experiments on the stability of viscous flow between rotating cylinders. III enhancement of stability by modulation. *Proc. Roy. Soc. Lond. A* **281**, 130–139.

Edwards, W. S., Tagg, R. P., Dornblaser, B. C. & Swinney, H. L. 1991 Periodic traveling waves with nonperiodic pressure. *Eur. J. Mech. B/Fluids* **10**, 205–210.

Fenstermacher, P. R., Swinney, H. L. & Gollub, J. P. 1979 Dynamical instabilities and the transition to chaotic Taylor vortex flow. *J. Fluid Mech.* **94**, 103–128.

Golubitsky, M., Stewart, I. & Schaeffer, D. G. 1988 *Singularities and Groups in Bifurcation Theory. Volume II*, *Applied Mathematical Sciences*, vol. 69. New York: Springer–Verlag.

Hall, P. 1975 The stability of unsteady cylinder flows. *J. Fluid Mech.* **67**, 29–63.

Hall, P. 1983 On the nonlinear stability of slowly varying time-dependent viscous flows. *J. Fluid Mech.* **126**, 357–368.

Hasoon, M. A. & Martin, B. W. 1977 The stability of viscous axial flow in an annulus with a rotating inner cylinder. *Proc. Roy. Soc. Lond. A* **352**, 351–380.

Henderson, R. D. 1997 Nonlinear dynamics and pattern formation in turbulent wake transition. *J. Fluid Mech.* **352**, 65–112.

Hoffmann, C., Lücke, M. & Pinter, A. 2004 Spiral vortices and taylor vortices in the annulus between rotating cylinders and the effect of an axial flow. *Phys. Rev. E* **69(5)**, 056309(1–14).

Hu, H. C. & Kelly, R. E. 1995 Effect of a time-periodic axial shear flow upon the onset of Taylor vortices. *Phys. Rev. E* **51**, 3242–3251.

Huerre, P. & Monkewitz, P. A. 1990 Local and global instabilities in spatially developing flows. *Ann. Rev. Fluid Mech.* **22**, 473–537.

Hwang, J. & Yang, K. 2005 Numerical study of TaylorCouette flow with an axial flow. *Computers & Fluids* **33**, 97–118.

Iooss, G. & Adelmeyer, M. 1998 *Topics in Bifurcation Theory and Applications*, 2nd edn., *Advanced Series in Nonlinear Dynamics*, vol. 3. Singapore: World Scientific.

Jones, C. A. 1985 Numerical methods for the transition to wavy taylor vortices. *J. Comput. Phys.* **61**, 321–344.

Joseph, D. D. 1976 *Stability of Fluid Motions I and II*. *Springer Tracts in Natural Philosophy* 27-28. Berlin: Springer-Verlag.

King, G. P., Li, Y., Lee, W., Swinney, H. L. & Marcus, P. S. 1984 Wave speeds in wavy taylor-vortex flow. *J. Fluid Mech.* **141**, 365–390.

Krueger, E. R., Gross, A. & Di Prima, R. C. 1966 On the relative importance of Taylor-vortex and non-axisymmetric modes in flow between rotating cylinders. *J. Fluid Mech.* **24**, 521–538.

Krupa, M. 1990 Bifurcations of relative equilibria. *SIAM J. Math. Anal.* **21** (6), 1453–1486.

Kuznetsov, Y. A. 2004 *Elements of Applied Bifurcation Theory, Third Edition*, 3rd edn. *Applied Mathematical Sciences* 112. New-York: Springer–Verlag.

Lamb, J. S. W. & Melbourne, I. 1999 Bifurcation from discrete rotating waves. *Arch. Ration. Mech. An.* **149**, 229–270.

Lamb, J. S. W., Melbourne, I. & Wulff, C. 2003 Bifurcation from periodic solutions with spatiotemporal symmetry, including resonances and mode interactions. *J. Differential Equations* **191**, 377–407.

Langenberg, M., Heise, M., Pfister, G. & Abshagen, J. 2004 Convective and absolute instabilities in counter-rotating spiral poiseuille flow. *Theoret. Comput. Fluid Dynamics* **18**, 97–103.

Langford, W. F., Tagg, R., Kostelich, E. J., Swinney, H. L. & Golubitsky, M. 1988 Primary instabilities and bicriticality in flow between counter-rotating cylinders. *Phys. Fluids* **31**, 776–785.

Lopez, J. M. & Marques, F. 2002 Modulated taylor-couette flow: Onset of spiral modes. *Theoret. Comput. Fluid Dynamics* **16**, 59–69.

Lopez, J. M. & Marques, F. 2004 Mode competition between rotating waves in a swirling flow with reflection symmetry. *J. Fluid Mech.* **507**, 265–288.

Ludwieg, H. 1964 Experimentelle Nachprüfung des Stabilitätstheorien für reibungsfreie Strömungen mit schraubenlinienförmigen Stromlinien. *Z. Flugwiss* **12**, 304–309.

Lueptow, R. M., Docter, A. & Min, K. 1992 Stability of axial flow in an annulus with a rotating inner cylinder. *Phys. Fluids A* **4**, 2446–2455.

Marques, F. & Lopez, J. M. 1997 Taylor-Couette flow with axial oscillations of the inner cylinder: Floquet analysis of the basic flow. *J. Fluid Mech.* **348**, 153–175.

Marques, F. & Lopez, J. M. 2000 Spatial and temporal resonances in a periodically forced hydrodynamic system. *Phys. D* **136** (3-4), 340–352.

Marques, F. & Lopez, J. M. 2006 Onset of three-dimensional unsteady states in small-aspect-ratio Taylor-Couette flow. *J. Fluid Mech.* **561**, 255–277.

Marques, F., Lopez, J. M. & Blackburn, H. M. 2004 Bifurcations in systems with Z_2 spatio-temporal and $O(2)$ spatial symmetry. *Phys. D* **189**, 247–276.

Marques, F., Lopez, J. M. & Shen, J. 2002 Mode interactions in an enclosed swirling flow: A double Hopf bifurcation between azimuthal wavenumbers 0 and 2. *J. Fluid Mech.* **455**, 263–281.

Meseguer, A., Avila, M., Mellibovsky, F. & Marques, F. 2007 Solenoidal spectral formulations for the computation of secondary flows in cylindrical and annular geometries. *Eur. Phys. J. Spec. Top.* **146**, 249–259.

Meseguer, A. & Marques, F. 2000 On the competition between centrifugal and shear instability in spiral Couette flow. *J. Fluid Mech.* **402**, 33–56.

Meseguer, A. & Marques, F. 2002 On the competition between centrifugal and shear instability in spiral Poiseuille flow. *J. Fluid Mech.* **455**, 129–148.

Meseguer, A. & Marques, F. 2005*a* Bicritical instabilities in pressure driven helicoidal flows. *J. Phys. Conf. Ser.* **14**, 228–235.

Meseguer, A. & Marques, F. 2005*b* On the stability of medium gap co-rotating spiral poiseuille flow. *Phys. Fluids* **17**, 094104.

Meseguer, A. & Mellibovsky, F. 2007 On a solenoidal Fourier-Chebyshev spectral method for stability analysis of the Hagen-Poiseuille flow. *Appl. Num. Math.* **57** (8), 920–938.

Moser, R. D., Moin, P. & Leonard, A. 1983 A spectral numerical method for the Navier-Stokes equations with applications to Taylor-Couette flow. *J. Comput. Phys.* **52**, 524–544.

Mullin, T., Toya, Y. & Tavener, S. J. 2002 Symmetry-breaking and multiplicity of states in small aspect ratio Taylor-Couette flow. *Phys. Fluids* **14** (8), 2778–2787.

Nagib, H. M. 1972 On instabilities and secondary motions in swirling flows through annuli. *Tech. Rep.*. Illinois Intitute of Technology.

Pfister, G., Buzug, T. h. & Enge, N. 1992 Characterization of experimental time series from Taylor-Couette flow. *Physica D* **58**, 441–454.

Pfister, G., Schmidt, H., Cliffe, K. A. & Mullin, T. 1988 Bifurcation phenomena in Taylor-Couette flow in a very short annulus. *J. Fluid Mech.* **191**, 1–18.

Pinter, A., Lücke, M. & Hoffmann, C. 2003 Spiral and taylor vortex fronts and pulses in axial through flow. *Phys. Rev. E* **67(2)**, 026318(1–15).

Rand, D. 1982 Dynamics and symmetry. Predictions for modulated waves in rotating fluids. *Arch. Ration. Mech. An.* **79**, 1–37.

Rayleigh, L. 1916 On the dynamics of rotating fluids. *Proc. Roy. Soc. Lond. A* **93**, 148–154.

Riecke, H. & Paap, H. G. 1986 Stability and wave-vector restriction of axisymmetric Taylor vortex flow. *Phys. Rev. A* **33**, 547–553.

Riley, P. J. & Laurence, R. L. 1976 Linear stability of modulated circular Couette flow. *J. Fluid Mech.* **75**, 625–646.

Sinha, M., Kevrekidis, I. G. & Smits, A. J. 2006 Experimental study of a Neimark-Sacker bifurcation in axially forced Taylor-Couette flow. *J. Fluid Mech.* **558**.

Snyder, H. A. 1962 Experiments on the stability of spiral flow at low axial Reynolds numbers. *Proc. Roy. Soc. Lond. A* **265**, 198–214.

Snyder, H. A. 1968 Stability of rotating Couette flow. i. asymmetric waveforms. *Phys. Fluids* **11**, 728–734.

Swift, J. W. & Wiesenfeld, K. 1984 Suppression of period doubling in symmetric systems. *Phys. Rev. Lett.* **52**, 705–708.

Takeuchi, D. I. & Jankowski, D. F. 1981 A numerical and experimental investigation of the stability of spiral Poiseuille flow. *J. Fluid Mech.* **102**, 101–126.

Taylor, G. I. 1923 Stability of a viscous liquid contained between two rotating cylinders. *Phil. Trans. Royal Soc.* **A223**, 289–343.

Trefethen, L. N. 2000 *Spectral Methods in Matlab*, 1st edn. *Software, Environments, and Tools* 10. Philadelphia: SIAM.

Tsameret, A. & Steinberg, V. 1994 Competing states in a Couette-Taylor system with an axial flow. *Phys. Rev. E* **49** (4), 4077–4086.

Tuckerman, L. S. & Barkley, D. 1990 Bifurcation analysis of the Eckhaus instability. *Phys. D* **46**, 57–86.

Vogel, M., Hirsa, A. H. & Lopez, J. M. 2003 Spatio-temporal dynamics of a periodically driven cavity flow. *J. Fluid Mech.* **478**, 197–226.

Weisberg, A. Y., Kevrekidis, I. G. & Smits, A. J. 1997 Delaying transition in Taylor-Couette flow with axial motion of the inner cylinder. *J. Fluid Mech.* **348**, 141–151.

Wereley, S. T. & Lueptow, R. M. 1999 Velocity field for taylor-couette flow with an axial flow. *Phys. Fluids* **11**, 3637–3649.

Williamson, C. H. K. 1996 Vortex dynamics in the cylinder wake. *Ann. Rev. Fluid Mech.* **28**, 477–539.

Wulff, C., Lamb, J. S. W. & Melbourne, I. 2001 Bifurcation from relative periodic solutions **21**, 605–635.

Youd, A. J. & Barenghi, C. F. 2005 Reversing and nonreversing modulated Taylor-Couette flow at finite aspect ratio. *Phys. Rev. E* **72**, 056321.

Youd, A. J., Willis, A. P. & Barenghi, C. F. 2003 Reversing and non-reversing modulated Taylor-Couette flow. *J. Fluid Mech.* **487**, 367–376.

Youd, A. J., Willis, A. P. & Barenghi, C. F. 2005 Non-reversing modulated Taylor-Couette flows. *Fluid Dynam. Res.* **36**, 61–73.